Title

Continuous Sensing of Physiological Biomarkers using Implantable Optical Sensors

Permalink

https://escholarship.org/uc/item/7rk6t5bc

Author

Nguyen, Dat

Publication Date

2021

Peer reviewed|Thesis/dissertation

UNIVERSITY OF CALIFORNIA,
IRVINE

Continuous Sensing of Physiological Biomarkers using Implantable Optical Sensors

DISSERTATION

submitted in partial satisfaction of the requirements for the degree of

DOCTOR OF PHILOSOPHY

in Biomedical Engineering

by

Dat Nguyen

Dissertation Committee:
Professor Elliot Botvinick, Chair
Professor Bernard Choi
Associate Professor Michelle Digman

2021

DEDICATION

To my family,

Your continued support and love motivates me to be the best version of myself.

TABLE OF CONTENTS

LIST OF FIGURES

ACKNOWLEDGEMENTS

CURRICULUM VITAE
DAT NGUYEN

EDUCATION

The University of California, Irvine, Henry Samueli School of Engineering, Irvine, CA   2017 – 2021
Doctor of Philosophy, Major: Biomedical Engineering
University of Southern California, Viterbi School of Engineering, Los Angeles, CA   2015 -2017
Master of Science, Major: Biomedical Engineering
California State University, Long Beach   2010 – 2014
Bachelor of Science, Major: Chemical Engineering, Minor: Chemistry
Engineering in Training: Chemical Engineering (2014)

FELLOWSHIPS

- Cardiovascular Applied Research and Entrepreneurship (CARE) Fellowship – NIH T32 Grant
- NSF: Integrative Graduate Education and Research Traineeship (IGERT) Biophotonics Across Energy, Space, and Time (BEST)

RESEARCH EXPERIENCE

Bio-Engineering of Advanced Mechanical Systems (BEAMS) Lab (Irvine, California)   2017 – 2021
PhD Graduate Student
- Project1 - Photostable and Proteolysis-Resistant Förster Resonance Energy Transfer-Based Calcium Biosensor
- Project2 - In Vivo Photonic Detection of pH and Lactate on an Implantable Flexible Sensor

Medical Research Institute (Pasadena, CA)   2016 – 2017
MRI Cardiac Research Associate
- Project 1 - Cerebrovascular Reactivity as a Biomarker for Alzheimer's Disease and Traumatic Brain Injury

Naval Research Laboratory (Washington D.C.)   2014
Naval Research Intern
- Project 1 - Validating the Hall-Petch Relationship in Nanocrystalline Ceramics

California State University, Long Beach (CSULB) (Long Beach, California)   2013 – 2014
Undergraduate Researcher
- Project 1 - Fabrication and power measurements of dye-sensitized solar cells

PROFESSIONAL EXPERIENCE

Genefluidics (Irwindale, CA)   2016
- Manufacturing Engineer Intern

Irvine Pharmaceutical Services (Irvine, CA)   2015
- West Production Chemist

Lipscomb Chemical Company (Long Beach, CA)   2013 – 2014
- Sample Desk Intern

PROFESSIONAL DEVELOPMENT

- UCI MGMT X410.18 **-** Six Sigma Lean Toolkit   2021
- UCI MGMT X442.6 **-** Medical Device Quality Systems   2020
- Graduate Professional Success (GPS-STEM) Member   2017 – 2021
- Graduate Association of Biomedical Engineering Students (GABES)   2017 – 2020

TEACHING EXPERIENCE

UCI: BME 135 - Photomedicine   2018

- Teaching Assistant

CSULB: Chemistry and Math Tutor 2013 – 2014

- Student Learning Assistant Level 2

PUBLICATIONS

1. Pending. **Dat Nguyen**, Micah M. Lawrence, Haley Berg, Mark Keating, John Weidling, and Elliot L. Botvinick. "In vivo Photonic Detection of pH and Lactate on an Implantable Flexible Sensor"
2. **Dat Nguyen**, Danielle M. Behrens, Sanjana Sen, Avid Najdahmadi, Jessica N. Pham, Gaetano Speciale, Micah M. Lawrence, Sudipta Majumdar, Gregory A. Weiss, and Elliot L. Botvinick. "Photostable and Proteolysis-Resistant Förster Resonance Energy Transfer-Based Calcium Biosensor." Anal. Chem. 2020, 92, 11, 7683–7689
3. J.A. Wollmershauser, B.N. Feigelson, E.P. Gorzkowski, C.T. Ellis, R. Goswami, S.B. Qadri, **Dat Nguyen**, J.G.Tischler, F.J. Kub, R.K. Everett. Reply to comments on "An Extended Hardness Limit in Bulk Nanoceramics", Acta Materialia 69 (2014) 9–16.

SELECTED PRESENTATIONS

International Webinar on Chemistry Spring 2021

- Photostable and Proteolysis-Resistant Förster Resonance Energy Transfer-Based Calcium Biosensor

NRL Summer Poster Presentation Summer 2014

- Validating the Hall-Petch Relationship in Nanocrystalline Ceramics

CSULB Lab Research Symposium Spring 2014

- Harnessing Solar Energy as an Alternative Energy Source to Power Electrical Devices

ABSTRACT OF THE DISSERTATION

Continuous Sensing of Physiological Biomarkers using Implantable Optical Sensors

by

Dat Nguyen

Doctor of Philosophy in Biomedical Engineering

University of California, Irvine 2021

Professor Elliot Botvinick, Chair

Continuous measurements of physiological biomarkers enables patients to assess their biomarkers levels in real – time and can help healthcare professionals determine if treatment is improving patient outcome. To monitor many of these biomarkers, an invasive blood draw is required. Unfortunately, frequent blood draws for frequent blood analyte measurements increases the likelihood of anemia, blood infection, and nerve damage, which in many situations, may worsen the patient's condition. My thesis works alleviates the need to frequently sample blood to continuously monitor physiological biomarkers by developing implantable optical sensors.

In collaboration with Dr. Gregory Weiss in the Department of Chemistry at UCI, I have engineered an implantable Förster Resonance Energy Transfer (FRET)-based calcium (Ca^{2+}) sensor that provides continuous, physiologically relevant Ca^{2+} measurements. The FRET sensor addresses the foreign body response by incorporating a molecular filter and takes advantage of the conformational changes observed when calcium binds to Troponin-C (within FRET complexes) to optically monitor calcium. My findings suggest that FRET-based sensing of target analytes using an implantable optical fiber sensor is effective and, in conjunction with protein engineering, is a new option for continuously monitoring physiologically relevant electrolytes.

For my second project, I spectroscopically monitor pH and lactate on an implantable flexible sensor. Together, pH and lactate values and trends can help healthcare professionals discriminate between metabolic and respiratory dysfunctions, helping to guide patient therapy. For pH sensing, a dual excitation, single band fluorescence detection scheme is employed, while for lactate sensing, an oxygen-sensitive phosphorescent scheme is employed. When implanted in a rabbit, the pH and lactate multi-analyte sensor shows accurate pathophysiological trends with respect to a handheld blood analyzer. The findings highlight the potential for implantable optical sensors to accurately monitor various analytes.

Collectively, these efforts show the feasibility of implantable optical sensors to continuously monitor physiological biomarkers. With libraries of new and selective luminescence dyes and FRET probes engineered each year, there is potential for implantable optical sensors to be a complete alternative to monitor blood analytes.

CHAPTER 1: INTRODUCTION AND BACKGROUND

1.1 Value of Continuous Biosensors

Continuous monitoring of biomarkers, such as calcium (Ca^{2+}), pH, glucose, and sodium (Na^+), is critical when a patient is in a diseased state or in need of critical care. For example, glucose should be continuously monitored during Type 1 Diabetes (T1D). An individual with T1D has improper glucose regulation and therefore must regulate their carbohydrate intake and how they exercise, as well as undergo insulin therapy to keep their glucose levels in a healthy range.[1–3] If improperly regulated, too high and low glucose levels (hyper- and hypoglycemia, respectively) can lead to both micro- and macrovasculature problems as well as death.[1] Since the 1990's, Continuous Glucose Monitors (CGMs) have helped T1D improve their glucose control **(Figure 1.1A)**.[4] Because CGMs can provide glucose measurements every 5 min, individuals with T1D can see whether their glucose levels are approaching hyper and hypoglycemic values and the rate of which their glucose levels are changing **(Figure 1.1B)**.[5] Subsequently, T1D can dose insulin or eat carbohydrates to normalize their glucose levels.[4] CGMs have enabled T1D patients to be in the normal range > 70% of the time.[4,5]
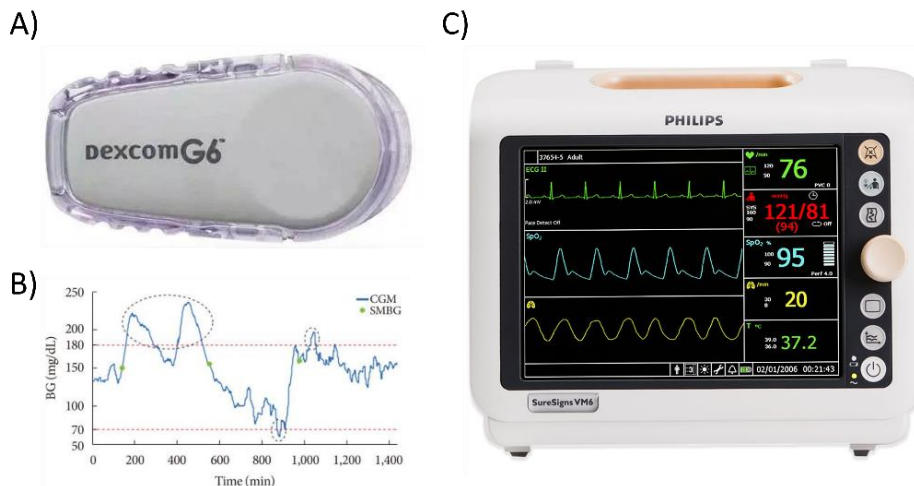
Figure 1.1. Continuous Biosensors. (A) Since the 1990's, Continuous Glucose Monitors (CGMs) have helped individuals with T1D improve their glycemic control.[6] (B) Single measurements of blood glucose (SMBG) may miss glucose levels out of the target range. However, CGMs can alert the user of both high and low glucose values, providing the user opportunities to intervene and administer treatment. (C) Vital monitors measure numerous biomarkers, such as respiratory rate and temperature, that can help healthcare professions identify and stratify metabolic or respiratory disturbances.[7] Graphics adapted from [16,17].

In clinics, vital monitors continuously measure patient heart rate, respiration rate, saturated oxygen (SpO_2), end tidal carbon dioxide CO_2 ($EtCO_2$), blood pressure, and temperature. (**Figure 1.2C**).[8] Together, these biomarkers are essential to monitor during, for example, surgery as high heart rates, high temperatures, and abnormal breathing patterns are signs of organ failure.[9–11] Individually, each biomarker can provide insight on the respiratory and metabolic state of the patient. If a patient's heart rate becomes tachycardic, this can be a sign of heart injury in which case, a ventricular assist device or total artificial heart may be prepared to assist in the workload of the heart.[12] If SpO_2 values are less than 92% (target range 92-96%), this is often a sign of poor oxygenation, usually requiring the patient to undergo mechanical ventilation to increase oxygen intake. Subsequently, $EtCO_2$ details how much CO_2 is being exhaled, a measure of both the metabolic activity of cells and respiratory status of the lungs.[13] If $EtCO_2$ falls below 35 mmHg, interventions associated with tachypnea or metabolic dysfunction should be executed.[14] For critical care situations, invasive pressure monitoring is employed. This method requires a cannula needle (connected to a pressure transducer) to be inserted into an artery. The pulsatile flow extracted from the needle is digitized with a pressure transducer to yield a pressure waveform descriptive of the diastolic and systolic pressure.[15] Low blood pressure can be a sign of heart failure or a low heart rate, both of which require immediate intervention.[12] Collectively, the ability of a vital monitor to continuous monitor key biomarkers can help direct healthcare professionals towards a targeted mode of treatment.

1.2 Blood Sampling and Analysis to Monitor Blood Biomarkers

1.2.1 Blood Sampling

To evaluate additional biomarkers, such as pH, lactate, Na^+, an invasive blood draw is required. These blood draws (either phlebotomies or arterial blood draws) may require anywhere from 1-10 mL of blood.[16,17] For phlebotomies (to monitor blood chemistries), first, a healthcare care professional must identify a vein to collect the blood specimen (**Figure 1.2A**). Typically, the median cubital vein (located at the ante cubital area) is chosen to draw blood as it is generally more visible and contains a greater cross-sectional area than both the cephalic and basilic vein.[18] The patient's arm is then placed on a padding, and a tourniquet is applied approximately 4-5 fingers widths above the collection point.[19] After, the location of the vein is disinfected with an alcohol wipe. For blood extraction, either vacuum extraction systems (with a vacutainer) or piston syringes are used.[19] Vacuum extraction system are more commonly employed because (1) they contain either a plastic/glass tube that protects the healthcare professional from blood spill, (2) the blood draw is under vacuum, and (3) blood can be directly pooled into test tubes.[19] If the vacuum extraction system technique is employed, a needle is inserted into the chosen vein and test tubes (with cap colors indicating which test to run) are cycled through the vacutainer to aliquot blood into each test tube. If a piston syringe is employed, volume for all blood tests is extracted at once and then aliquoted to the labeled test tubes. Once blood sampling is completed, the tourniquet must be removed prior to needle withdrawal and the site of needle insertion is immediately exposed to a cotton swab to prevent bleeding. These samples are then processed with a blood analyzer machine with results available spanning from 30 min to hours.[20] A similar process is completed for arterial blood draws where blood samples are typically withdrawn from

the radial artery near the wrist, without a tourniquet, to quantify, for example, the amount of oxygen and carbon dioxide in the blood (**Figure 1.2B**).[21]
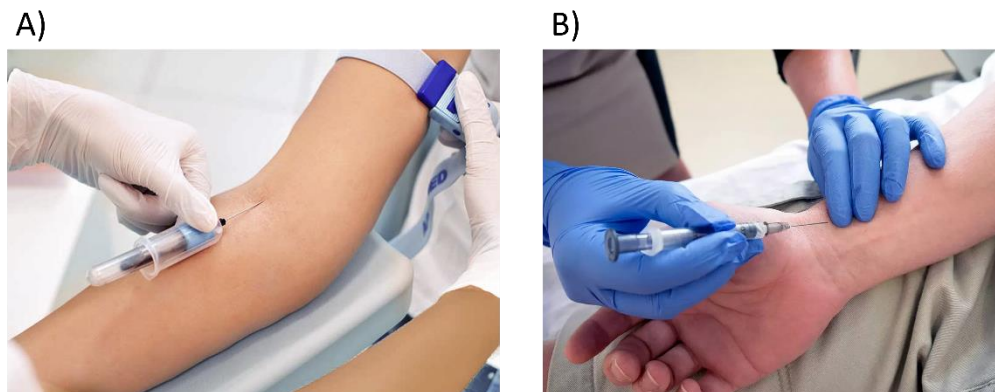
Figure 1.2. Phlebotomy and Arterial Blood Gas Sampling. A) To sample blood chemistries (calcium, glucose, etc.), phlebotomists commonly use the median cubital vein located at the antecubital fossa region to withdraw blood. B) The radial artery is used to extract blood for blood gas sampling. Images adapted from [22,23].

1.2.2 Blood Analyzers

Benchtop and handheld blood analyzers machines are the standard for quantifying blood electrolyte, chemistry, and gas levels.[24] Examples of such machines are the Abbott i-STAT, Piccolo Xpress, and Yellow Spring Instruments (YSI) analyzers. The Abbott i-STAT (**Figure 1.3A**) blood analyzer accompanied with Abbot cartridges (such as CG4+, CG8+, and EG7+, **Figure 1.3B**) permit testing of biomarkers such as lactate, pH, partial pressure of oxygen, ionized Ca^{2+}, and Na^+. This handheld analyzer measures biomarkers through electrochemical modes of operation including: (1) potentiometric, (2) amperometric, and (3) conductometric.[25] Potentiometric sensing measures the different in potential between a working and reference electrode using the Nernst equation.[25] Amperometric sensing applies a potential (operation voltage) to a working electrode and the resulting current produced from an oxidation and reduction reaction (relative to a reference electrode) can be translated to analyte concentration[26]. Conductometric sensing is used for electrolyte sensing where an alternative current is applied

between a working and reference electrode. The resulting voltage difference is proportional to the analyte measured.[25] Similar to the Abbott i-STAT, the Piccolo Xpress chemistry analyzer (**Figure 1.3C**) is accompanied with cartridges to measure a range of blood biomarkers. These cartridges contain low hazard lyophilized chemical beads enclosed in a plastic rotor that react with the analyte of interest.[26] Changes in absorbance behavior at one or multiple wavelengths are quantified to yield analyte concentration.[26,27]The last blood analyzer previously mentioned is the YSI 2300 STAT PLUS Glucose and Lactate Analyzer (**Figure 1.3D**) which employs enzymes glucose and lactate oxidase (GLOX and LOX) to react and monitor with glucose and lactate, respectively. [28] Both oxidases yield hydrogen peroxide as a byproduct. The production of hydrogen peroxide is oxidized with a platinum wire to yield a current proportional to the analyze concentration.
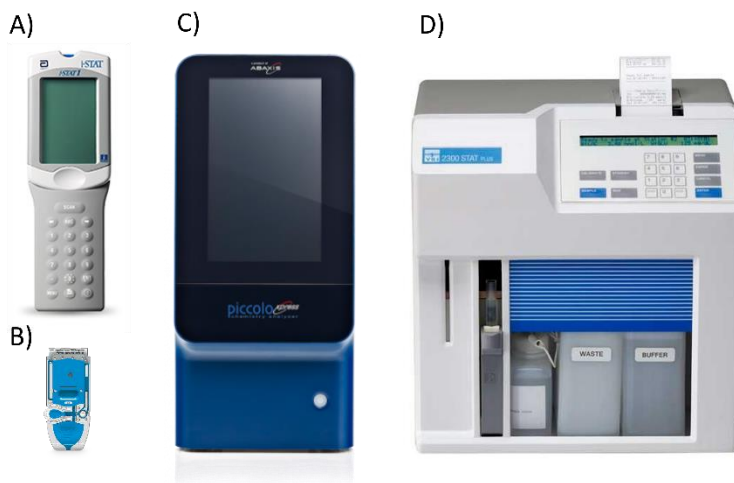
Figure 1.3. Blood Analyzers. Portable (A) Abbott i-STAT accompanied with a CG4+ cartridge (B) can be used to measure blood gasses such as pH and SpO_2. (C) Piccolo Xpress quantifies absorbance changes to measure analytes levels.[26] (D) The YSI 2300 STAT PLUS Glucose and Lactate Analyzer operates electrochemically to monitor glucose and lactate. Images adapted from [29–32].

1.3 Drawbacks with Blood Sampling and Analyzers for Continuous Biomarker Sensing

1.3.1 Issues with Blood Sampling

For those requiring intensive care, frequent measurements of blood biomarkers necessitates continuous blood sampling. However, there are many drawbacks with continuous blood sampling (and their subsequent analysis) that must be considered and addressed prior to repeated sampling. For example, as more blood is withdrawn, the likelihood of both anemia and blood infections increase **(Figure 1.4A,B)**.[33,34] In regards to anemia, in a retrospective study, every 100 mL of phlebotomy was associated with a reduction of 7.0 g/L and 19% in hemoglobin and hematocrit, respectively.[34] In intensive care situations, such as after cardiovascular surgery, the reduction in red blood cells and hematocrit has increased the likelihood of morbidity.[34] In a review of 19,617 radial artery cannulations, temporary occlusion **(Figure 1.4C)** of the artery was observed in 19.70% of those cases.[35] Studies show that arterial occlusions may lead to local ischemia and stroke, with poorer clinical outcome associated with older aged patients.[36] Needle insertion into the subcutaneous space also carries the risk of nerve damage **(Figure 1.4D)**. The most common nerve damage involves the lateral antebrachial cutaneous nerve which can lead to complex regional pain syndrome.[37] The incidence of nerve injury was found to be between 1 in 21,000 and 1 in 26,000.[38] Although chronic ailments associated with venipuncture associated nerve damage are scarce (1 in 1.5 million phlebotomies), 87% of these patients require treatment by a pain management specialist.[38] Furthermore, though incidences of hematomas are rare after arterial blood draws and phlebotomy (<3%), ecchymosis occur more often (15%) with a noticeable diameter <20 mm occurring in 90% of cases.[19,39] Interestingly, hematomas were exhibited at the site of phlebotomy in 12.3% of blood donors, an observed increased likely due to prolonged blood draws at the venipuncture site **(Figure 1.4E)**.[40] A side effect of hematoma is the compression of surrounding nerves that has been noted to occur in 24% of patients.[38]
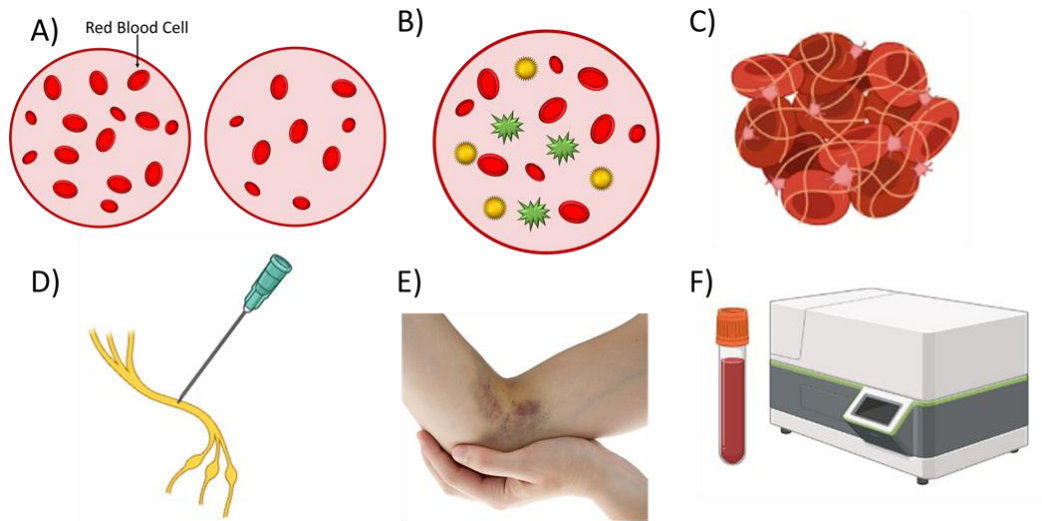
Figure 1.4. Risks of Continued Blood Sampling. Drawbacks of blood sampling strategies include (A) anemia, (B) blood infection, (C) blood clots, (D) nerve damage, (E) hematoma, and (F) poor turnover time. Images created on Biorender.

Additionally, tourniquets, which should only be left on less than 1 min, can result in hemoconcentration. As a result, analytes such as glucose, potassium, and cholesterol can have falsely elevated readings.[41] Lastly, in a large multicenter study, the average completion time of phlebotomy took 6 min only 50% of the time, while in 10% of cases, spanned from 21 mins to an hour.[19] The length of blood extraction may hamper patient confidence and compliance that diminishes the opportunity to provide the patient the best care.

1.3.2 Issues with Blood Analyzers

Blood analyzers also have risks that limit their efficacy during critical care and towards real-time measurements. One of the obvious flaws of blood analyzers are their contribution to poor turnover times (results provided $\geq$ 30 min).[20] A college of American Pathologists (CAP) Q-Probes survey of emergency department turn over time showed low satisfaction to a laboratory's sensitivity to urgent testing (39% satisfaction) and towards meeting the physician need (48%

satisfaction).[42] Treatments during these critical conditions were delayed more than 50% of the time (43% of the time) and patient length of stay increased over half the time (61% of the time, **Figure 1.4F**).[42] Poor turnover time obviates immediate care, wasting precious time to provide a patient the best care. In general, most blood analyzer require a low volume of sample, generally < 100 µL.[43] However, loading samples are not a simple process.[44,45] This is obvious when loading samples into Abbott i-STAT cartridges as there is an arrow indicating to what level to load the blood sample. If too little or too much blood is loaded, the i-STAT outputs an error message requesting another cartridge to be loaded. In this situation, not only has there been time lost to provide the patient critical information, but the cartridge has been wasted. Unfortunately, another blood draw may be necessary because the blood sample may have not been stored correctly. Lastly, if a single key biomarker is to be measured, the blood analyzer will run all tests noted within the sample cartridge sample or as provided within the system. This not only wastes resources but consumes time that would be better spent treating the patient. A clear example of this is exhibited with the YSI 2300 STAT PLUS Glucose and Lactate Analyzer. For an individual experiencing diabetic ketoacidosis, a rapid measurement of glucose can help a clinician determine whether their insulin infusion reduced their patient's glucose levels. However, as the YSI 2300 STAT PLUS Glucose and Lactate Analyzer measures both lactate and glucose, extra time and resources are utilized on measuring lactate, which in this situation, that is not critical towards patient prognosis.

1.4 Luminescent Sensing Alternatives

1.4.1 Fluorescence and Phosphorescence

The Piccolo Xpress blood analyzer and many of the sensing modalities of vital monitors utilize spectroscopy modalities, specifically absorption properties, to monitor analytes. Additional

spectroscopic techniques, namely fluorescence of phosphorescence, have gained traction towards

continuous sensing biomarkers. The mechanisms of fluorescence and phosphorescence are

closely related and are subsequently described (**Figure 1.5**). In general, in the ground state (S_0), a

molecule contains electron pairs that have opposite spin orientations ($\downarrow,\uparrow$).[46] When the molecule

absorbs photons, the molecule is promoted to its excited state (S_1).[46] In the excited state, one of

the electron pairs jumps up one energy level. In fluorescence, the spin orientations are

unchanged. As energy dissipates, photons are emitted in a time span of nanoseconds (ns) to

microseconds (μs) with lower energy, and thus at a longer wavelength (relative to the excitation

wavelength).[46] In phosphorescence, after one of the electron pairs jumps one energy level,

instead of immediately dissipating energy, the electron undergoes a process known as

intersystem crossing.[46] As a result of intersystem crossing, one of the electron pairs spin

orientation is flipped, causing both electron pairs to have identical spin orientations. This state is

called the Triplet State (T_1).[46]. In this state of phosphorescence, even less energy is dissipated (in

comparison to fluorescence), where the wavelengths emitted are even longer and the emission

process is slower, in the millisecond (ms) regime.[46] Interestingly, oxygen naturally is present in

its triplet state.[47] Evidence suggest that this phenomenon allows oxygen to play a crucial role in

phosphorescence quenching where higher concentrations of oxygen lead to shorter

phosphorescence lifetimes and lower concentrations of oxygen lead to higher phosphorescence

lifetimes. [48]
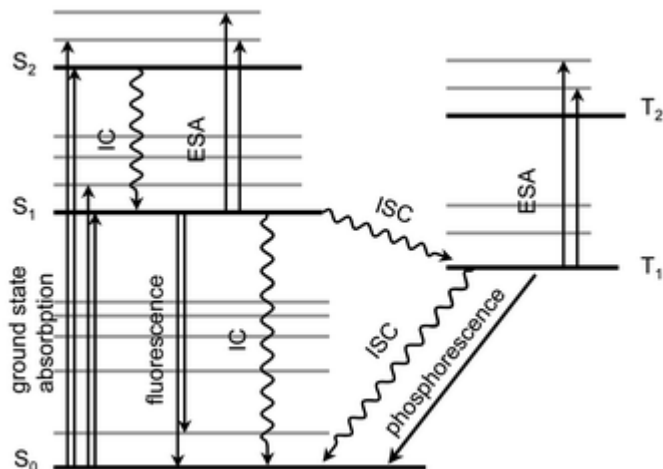
Figure 1.5. Mechanism of Fluorescence and Phosphorescence. Compared to fluorescence, phosphorescent molecules undergo intersystem crossing (ISC) causing an electron orbital to spin. When energy is dissipated from a phosphorescent molecule, the light emitted is at a longer wavelength and the emission occurs slower than fluorescence.[49] Image adapted from [49].

1.4.2 Förster Resonance Energy Transfer (FRET)

An extension of fluorescence known as Förster Resonance Energy Transfer (FRET) has become

a powerful tool in biological research.[50] FRET was first described by Theodore Förster in 1946

and is a collision-free, non-radiative energy transfer by which an excited state donor fluorophore

transfers energy to a ground state acceptor fluorophore.[50,51] The result is an fluorescence

emission signal with properties of both the donor and acceptor fluorophore.[50] There are three

criterion that must be met for FRET to occur (**Figure 1.6**).
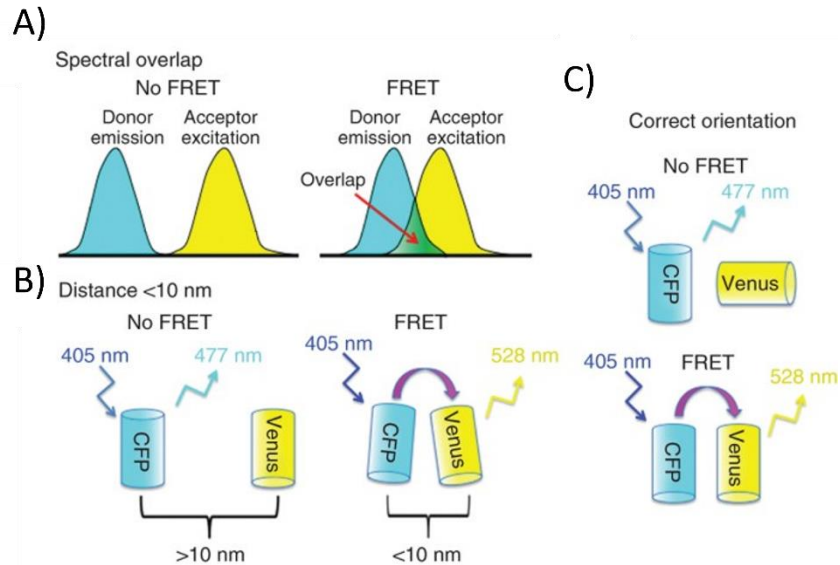
Figure 1.6. Dependencies of FRET. (A) The donor emission signal must overlap the acceptor excitation ratio for the radiationless energy transfer to occur. (B) The donor and acceptor fluorophores must be as least 10 nm of one another for FRET to occur. (C) Collinear dipoles lead to optimal FRET while perpendicularly oriented dipoles lead to an absence of FRET. Image adapted from [52].

The first criteria is that the donor fluorophore's emission spectrum must overlap the acceptor

fluorophore's excitation spectrum (**Figure 1.6A**). This overlapping region is called the spectral

overlap $J(\lambda)$ and is described by the following (**eq 1.1**):

$$J(\lambda) = \int_0^\infty F_D(\lambda)\varepsilon_A(\lambda)\lambda^4 d\lambda \qquad\qquad \textbf{eq 1.1}$$

where λ is the wavelength (in nm), and $\varepsilon_A(\lambda)$ and $F_D(\lambda)$ are the molar absorption coefficient of

the acceptor and the normalized fluorescence emission of the donor at wavelength

λ, respectively.[53] The greater the overlap between the acceptor excitation and donor emission

spectrums, the greater the spectral overlap.

The second criteria is that the donor fluorophore and acceptor fluorophore must be within close proximity (< 10 nm) for the resonance energy transfer to occur **(Figure 1.6B)**.[50] The Foster radius (R_o) is an extension of this criteria and is the length by which 50% FRET efficiency is achieved and is characterized by the following equation (**eq 1.2**):

$$E_{fret} = \frac{R_o^6}{R_o^6 + r^6}$$
                                             eq 1.2

where E_{fret} is the efficiency of FRET (percent of energy transfer from the donor to the acceptor fluorophore), R_o is the Foster radius, and r is actual distance between the donor and acceptor fluorophore.[50,53–55] Tabulated R_o values for various FRET pairs, such as Cyan Fluorescent Protein (CFP) and Yellow Fluorescent Protein (YFP), have been calculated with the following equation (**eq 1.3**):

$$R_o = 9.78 \ x \ 10^3 [k^2 n^{-4} Q_D J(\lambda)]^{1/6} \text{ (in Å)}$$
                                             eq 1.3

Where k^2 is the orientation factor between the acceptor and donor, n is the refractive index of the medium, Q_D is the quantum yield of the donor in the absence of the acceptor, and $J(\lambda)$ is the degree of spectral overlap between the donor emission spectrum and acceptor absorbance spectra.[54,5553] The FRET efficiency drastically diminishes by the sixth power from the distance between the donor and acceptor fluorophores, labelling FRET as a "spectroscopic ruler".

The last criterion is that the fluorophores dipoles must be oriented within a specific orientation for maximal dipole – dipole coupling **(Figure 1.6C)**. This orientation factor (k^2) is described as follows (**eq 1.4**):

$$k^2 = \cos(\theta_R - 3\cos\theta_D \cos\theta_A)^2$$
                                             eq 1.4

Where θ_R is the angle between the donor and acceptor fluorophore dipole and θ_D and θ_A are the angles of the donor and acceptor fluorophores dipoles, respectively.[50,53,55,56] If the dipoles of the FRET pair are oriented in a perpendicular fashion, the FRET efficiency is 0%. However, if the dipoles are in a colinear plane, $k^2 = 4$ and the FRET efficiency is optimal.[71] Advances in FRET probes and fluorescent labelling techniques have diversified the application of FRET into proteomics, signal transduction, and biosensors (genetically encoded Ca^2 indicators (GECI)), and is therefore hypothesized to be a vehicle for additional analyte sensing.[57–62]

1.5 Physiologically Relevant Biomarkers

Detailed below is a list of biomarkers (calcium, pH, and lactate) that are tightly regulated during homeostasis. Unfortunately, during either metabolic or physiological disturbances, the concentrations of these biomarkers may dramatically deviate, thus, necessitating sensors to continuously measure these analytes.

1.5.1 Calcium

Physiologically, total serum Ca^{2+} (2.1 – 2.6 mM) is made up of two subpopulations, those that are bound or unbound to protein (called ionized Ca^{2+}).[63] Ionized Ca^{2+} makes up approximately 50% of the Ca^{2+} load and is the form of Ca^{2+} that regulates nerve activation, cardiac function, the immune response, and bone structure.[64,65] Ionized Ca^{2+} is regulated by parathyroid hormone, vitamin D, and calcitonin.[63] If an individual is exhibiting hypocalcemia (ionized $Ca^{2+} < 1.1$ mM), parathyroid hormone (PTH) is secreted from chief cells located within the parathyroid glands (located in the thyroid).[66–68] PTH activate multinucleated osteoclasts which break down bone tissue, which store up 99% of the Ca^{2+} reserve.[69] Parathyroid hormone also increases Ca^{2+} absorption in the intestines, and reabsorption in the kidneys.[70] Exogenous (from supplement and

food) and endogenous Vitamin D hydroxylated in the liver yields it active form, 1,25-Dihydroxyvitamin D_3, which accommodates parathyroid hormone to further the increase in absorption a of Ca^{2+} in the intestines and kidney (**Figure 1.7A**).[71] These mechanisms increase ionized blood Ca^{2+} levels. Meanwhile, calcitonin, secreted by C-cells located the thyroid glands, counterbalances PTH by inhibiting osteoclast activity and decreasing Ca^{2+} reabsorption.[68,72] As a result, calcitonin prevents instances of hypercalcemia.

In conditions such as breast and lung cancer as well as myeloma, cells secrete parathyroid-hormone- related-peptide which mimics the function of parathyroid hormone.[71,73] This release is highly unregulated; therefore, activated osteoclasts break down copious amounts of bones tissue, dramatically increasing the ionized blood Ca^{2+} levels. Hypercalcemia is observed within 30% of patients exhibiting malignant cancer and has a 30 day morbidity rate of 50%.[92] To rectify hypercalcemia, bisphosphonates supplements are administered, which similar to calcitonin, mitigate the activity of osteoclasts.[73] Unfortunately, high levels of bisphosphonates may lead to severe musculoskeletal pain and esophageal cancer.[75] Meanwhile, hypocalcemia is also a serious issue during blood transfusions during liver transplants.[76] Upon blood transfusion, citrate that is not properly filtered can chelate Ca^{2+}, reducing ionized Ca^{2+} levels.[76] The lack of calcium causes arrhythmias and nerve impairment.[63,66]
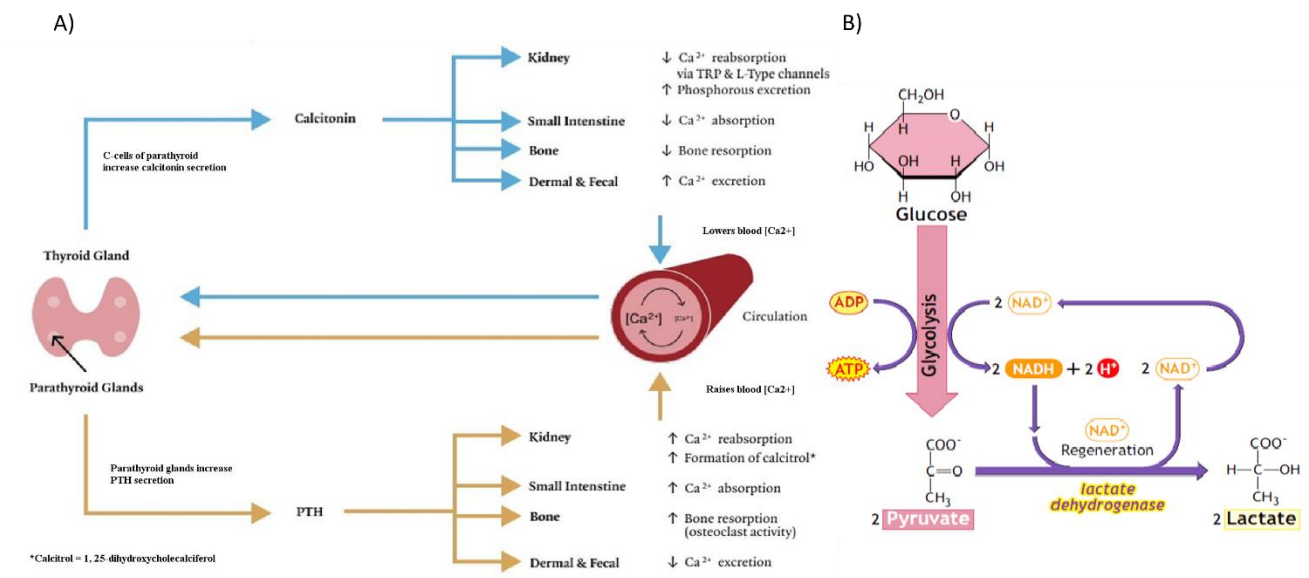
Figure 1.7. Calcium and Lactate Metabolism. A) Hormones Parathyroid hormone (PTH) and 1,25-Dihydroxyvitamin D3 can be upregulated to increase ionized Ca^{2+} levels. B) Anaerobic glycolysis generates lactate and converts NADH to NAD^+. Images adapted from [77,78].

1.5.2 pH and Lactate

Of the many mechanisms that buffer blood pH, the bicarbonate buffering system may be the most important. In the bicarbonate buffering system, carbon dioxide (CO_2), a gaseous acid and byproduct of cellular respiration, reacts with water in the blood stream to yield carbonic acid (H_2CO_3).[79,80] H_2CO_3 (a weak acid) reversibly dissociates into bicarbonate (HCO_3^-) and hydronium ion (H^+). Both bicarbonate and hydronium can neutralize blood pH by binding to excess cations and anions, respectively.[79,80]

The lungs are one of the two primary organs that can modulate blood pH in the blood bicarbonate system.[79] By increasing (hyperventilation) or decreasing (hypoventilation) respiration rate, the lungs can modulate CO_2 metabolism which in turn, can change pH.[79] Hypoventilation builds up CO_2, causing a reduction in blood pH, while hyperventilation exhales

CO_2, increasing blood pH. The lungs address pH imbalances by peripheral and central chemoreceptors activation, receptors located on carotid/aortic bodies and the medullary oblongata, respectively.[79,81] In general, the chemoreceptors sense the acidotic/alkalotic pH levels and send nerve impulses to the external intercoastal muscles and diaphragm, resulting in either an increase or decrease in ventilation.[82]

The kidneys are the second primary organs that can buffer blood pH in the bicarbonate buffering system. The kidneys can buffer pH by modulating HCO_3^- reabsorption or producing new HCO_3^-.[79] Although the kidney's buffering mechanism is slower than the lungs (days), its buffering capability is much stronger, providing greater changes in pH. 80% of bicarbonate reabsorption occurs in the proximal tubule (PT).[79] In the lumen of the PT, H^+ and HCO_3^- react to slowly generate CO_2 and water. CO_2 and water are then able to freely pass into the proximal tubule cell, reacting with carbonic anhydrate to yield H_2CO_3 and subsequently, HCO_3^- and H^+.[79] H^+ gets shuttled to the proximal tube lumen via H^+-ATPase which, cyclically, reacts with HCO_3^- to yield CO_2 and water. The HCO_3^- in the proximal tubule cell is passed into the blood stream via a sodium HCO_3^- cotransport, typically either NBCe1-A, or SLC4A4, for reabsoprtion.[79] To additionally modulate HCO_3^- in the blood, glutamine metabolism can be altered. Glutamine is metabolized by the kidney to create 2 copies of both HCO_3^- and ammonium (NH_4^+).[83] Generally, NH_4^+ is secreted into the urine while HCO_3^- is shuttled to the blood. However, NH_4^+ can be metabolized in the liver to yield urea and $2H^+$. The H^+ may react with HCO_3^- in the blood, negating new HCO_3^- generation.[83]

Lactate (interchangeably defined as lactic acid) is a common biomarker of anaerobic glycolysis and is predominately produced by skeletal muscle and red blood cells.[84,85] In anaerobic glycolysis, lactate is converted from pyruvate via lactate dehydrogenase, (**Figure 1.7B**) with

16

baseline lactate values < 2 mM.[86,87] Lactate values can increase during strenuous exercise, and during instances of mitochondria failure and hypoxemia, can reach up to 15 mM.[88] Typically metabolized by the liver (Cori Cycle) and kidneys, conditions such as sepsis, hypovolemia, and cardiac shock (due to hypoperfusion and trauma) can yield dangerous amounts of lactate, that if left untreated, can be deadly.[89] One reason for this is that lactate is a strong acid, with a pKa of 3.9.[90] The production of lactate can therefore coincide with a reduction blood pH that can detrimentally alter organ, protein, and cell function.[91,92]

1.6 Overview of the Dissertation

To help clinicians continuously monitor biomarkers without the need of frequent blood draws, my thesis work develops continuous implantable optical biosensors. Specifically, sensors are fabricated to continuously monitor calcium, pH, and lactate. Calcium is critical to monitor during hypercalcemia, exhibited with malignant cancers, while simultaneously monitoring pH and lactate can help guide therapy during conditions such as sepsis. Chapter 2 focuses on creating a FRET-based Ca^{2+} sensor that contains a semi-permeable membrane designed to mitigate the foreign body response upon device implantation. A FRET molecule was genetically modified to selectively bind to Ca^{2+}, and here, was further engineered to integrate photostable dyes to alleviate concerns of photobleaching. Chapter 3 describes the fabrication and results of a multi-analyte sensor which uses both fluorescence and phosphorescence luminescent properties to measure pH and lactate, respectively. A filter-coated photodetector is manually assembled to collect pH-sensitive emission signals in the visible region of light. By serially exciting LEDs encapsulated with pH and lactate sensitive chemistries, pH and lactate sensing can be completed on a single sensor, in parallel, without signal crosstalk.

1.7 References

1. Kharroubi AT. Diabetes mellitus: The epidemic of the century. *World J Diabetes*. 2015;6(6):850. doi:10.4239/wjd.v6.i6.850
2. Atkinson MA. The pathogenesis and natural history of type 1 diabetes. *Cold Spring Harb Perspect Biol*. 2012;4(12). doi:10.1101/cshperspect.a007641
3. Mameli C. Explaining the increased mortality in type 1 diabetes. *World J Diabetes*. 2015;6(7):889. doi:10.4239/wjd.v6.i7.889
4. Freckmann G. Basics and use of continuous glucose monitoring (CGM) in diabetes therapy. *J Lab Med*. 2020;44(2):71-79. doi:10.1515/LABMED-2019-0189
5. Cappon G, Vettoretti M, Sparacino G, Facchinetti A. Continuous Glucose Monitoring Sensors for Diabetes Management: A Review of Technologies and Applications. *Diabetes Metab J*. 2019;43(4):383. doi:10.4093/DMJ.2019.0121
6. Cappon G, Vettoretti M, Sparacino G, Facchinetti A. Continuous Glucose Monitoring Sensors for Diabetes Management: A Review of Technologies and Applications. *Diabetes Metab J*. 2019;43(4):383. doi:10.4093/DMJ.2019.0121
7. SureSigns VM6 Vital Signs Patient Monitor w/ECG, SpO2, NBP. Accessed August 16, 2021. https://www.spotmonitor.com/philips-suresigns-vital-signs-monitor-863064-863065-vm6-ecg-spo2-nbp-ibp-temp-recorder.html
8. Brekke IJ, Puntervoll LH, Pedersen PB, Kellett J, Brabrand M. The value of vital sign trends in predicting and monitoring clinical deterioration: A systematic review. *PLoS One*. 2019;14(1). doi:10.1371/JOURNAL.PONE.0210875
9. Vital signs to monitor hospital patients: a systematic review. *JBI Libr Syst Rev*. 2008;6(Supplement):1-11. doi:10.11124/JBISRIR-2008-785
10. Lima A, van Bommel J, Jansen TC, Ince C, Bakker J. Low tissue oxygen saturation at the end of early goal-directed therapy is associated with worse outcome in critically ill patients. *Crit Care 2009 135*. 2009;13(5):1-7. doi:10.1186/CC8011
11. Gilhooley C, Burnhill G, Gardiner D, Vyas H, Davies P. Oxygen saturation and haemodynamic changes prior to circulatory arrest: Implications for transplantation and resuscitation. *J Intensive Care Soc*. 2019;20(1):27. doi:10.1177/1751143718764541
12. Cook JA, Shah KB, Quader MA, et al. The total artificial heart. *J Thorac Dis*. 2015;7(12):2172. doi:10.3978/J.ISSN.2072-1439.2015.10.70
13. Aminiahidashti H, Shafiee S, Kiasari AZ, Sazgar M. Applications of End-Tidal Carbon Dioxide (ETCO2) Monitoring in Emergency Department; a Narrative Review. *Emergency*. 2018;6(1):e5. Accessed August 11, 2021. /pmc/articles/PMC5827051/
14. Kodali BS, Urman RD. Capnography during cardiopulmonary resuscitation: Current evidence and future directions. *J Emerg Trauma Shock*. 2014;7(4):332. doi:10.4103/0974-2700.142778
15. Romagnoli S, Ricci Z, Quattrone D, et al. Accuracy of invasive arterial pressure monitoring in cardiovascular patients: an observational study. *Crit Care*. 2014;18(6). doi:10.1186/S13054-014-0644-4
16. WHO guidelines on drawing blood: best practices in phlebotomy WHO Library Cataloguing-in-Publication Data WHO guidelines on drawing blood: best practices in phlebotomy. Published online 2010.
17. Nigam PK. Correct Blood Sampling for Blood Gas Analysis. *J Clin Diagn Res*. 2016;10(10):BL01. doi:10.7860/JCDR/2016/21383.8712
18. Mukai K, Nakajima Y, Nakano T, et al. Safety of Venipuncture Sites at the Cubital Fossa as Assessed by Ultrasonography. *J Patient Saf*. 2020;16(1):98.

doi:10.1097/PTS.0000000000000441

19. Ialongo C, Bernardini S. Phlebotomy, a bridge between laboratory and patient. *Biochem Medica*. 2016;26(1):17. doi:10.11613/BM.2016.002

20. Hawkins RC. Laboratory Turnaround Time. *Clin Biochem Rev*. 2007;28(4):179. Accessed August 9, 2021. /pmc/articles/PMC2282400/

21. Arterial blood sampling. Published online 2010. Accessed August 11, 2021. https://www.ncbi.nlm.nih.gov/books/NBK138661/

22. Interpreting ABGs - Arterial Blood Gases Explained. Accessed August 23, 2021. https://nurse.org/articles/arterial-blood-gas-test/

23. Open Enrollment for Vocational Training • News - MENDOCINO COUNTY OFFICE OF EDUCATION. Accessed August 23, 2021. https://www.mcoe.us/District/News/4-Open Enrollment for Vocational Training.html

24. Snider CL, Dick EJ, Jr, et al. Evaluation of Four Hematology and a Chemistry Portable Benchtop Analyzers Using Nonhuman Primate Blood. *J Med Primatol*. 2009;38(6):390. doi:10.1111/J.1600-0684.2009.00385.X

25. i-STAT ® 1 System Manual. Accessed August 9, 2021. www.abbott.us/patents

26. Piccolo ® Comprehensive Metabolic Panel For In Vitro Diagnostic Use and For Professional Use Only Customer and Technical Service: 1-800-822-2947.

27. Piccolo Xpress chemistry analyzer Operator's Manual. Published online 2020.

28. OWEN VM. Biosensors: *Ann N Y Acad Sci*. 1987;501(1):233-239. doi:10.1111/J.1749-6632.1987.TB45715.X

29. i-STAT 1 | Abbott Point of Care Testing. Accessed August 23, 2021. https://www.globalpointofcare.abbott/en/product-details/i-stat-system-us.html

30. i-STAT Alinity v CG4+ Cartridge | Zoetis US. Accessed August 23, 2021. https://www.zoetisus.com/products/diagnostics/vetscan/i-stat-cg4+-cartridge.aspx

31. Piccolo Xpress Chemistry Analyzer - Abbott 07P0501 | Vitality. Accessed August 23, 2021. https://www.vitalitymedical.com/piccolo-xpress-chemistry-analyzer.html?network=g&device=c&keyword=&campaign=916499254&adgroup=pla-343104258937&gclid=Cj0KCQjwjo2JBhCRARIsAFG667X_C2lb0PVqLVK0SOWgx5XHo83TQUEbA9phjo0FpKNj4bmgH6fG9N4aAphJEALw_wcB

32. YSI 2300 | gscysi2021. Accessed August 23, 2021. https://www.gscysi.com/ysi-2300d-stat-plus-glucose-an

33. Kim KH, Oh KY. Clinical applications of therapeutic phlebotomy. *J Blood Med*. 2016;7:139. doi:10.2147/JBM.S108479

34. Thavendiranathan P, Bagai A, Ebidia A, Detsky AS, Choudhry NK. Do Blood Tests Cause Anemia in Hospitalized Patients?: The Effect of Diagnostic Phlebotomy on Hemoglobin and Hematocrit Levels. *J Gen Intern Med*. 2005;20(6):520. doi:10.1111/J.1525-1497.2005.0094.X

35. Scheer BV, Perel A, Pfeiffer UJ. Clinical review: Complications and risk factors of peripheral arterial catheters used for haemodynamic monitoring in anaesthesia and intensive care medicine. *Crit Care*. 2002;6(3):199. doi:10.1186/CC1489

36. Ha S-K, Lim D-J, Seok B-G, Kim S-H, Park J-Y, Chung Y-G. Risk of Stroke with Temporary Arterial Occlusion in Patients Undergoing Craniotomy for Cerebral Aneurysm. *J Korean Neurosurg Soc*. 2009;46(1):31. doi:10.3340/JKNS.2009.46.1.31

37. Elahi F, Reddy CG. Venipuncture-induced complex regional pain syndrome: A case report and review of the literature. *Case Rep Med*. 2014;2014. doi:10.1155/2014/613921

38. Oven SD, Johnson JD. Radial Nerve Injury after Venipuncture. *J Hand Microsurg*. 2017;9(1):43. doi:10.1055/S-0037-1599220

39. Arterial blood sampling. Published online 2010. Accessed August 12, 2021. https://www.ncbi.nlm.nih.gov/books/NBK138661/

40. Waheed U, Biochem Mp, Ansari MA, Biochem Ms, Zaheer HA. Phlebotomy as the Backbone of the Laboratory. *Lab Med*. 2013;44(1):e69-e71. doi:10.1309/LMC7WIA8Z7VVBSTO

41. Saleem S, Mani V, Chadwick MA, Creanor S, Ayling RM. A prospective study of causes of haemolysis during venepuncture: tourniquet time should be kept to a minimum: *http://dx.doi.org/101258/acb2009008228*. 2009;46(3):244-246. doi:10.1258/ACB.2009.008228

42. Hawkins RC. Laboratory Turnaround Time. *Clin Biochem Rev*. 2007;28(4):179. Accessed August 11, 2021. /pmc/articles/PMC2282400/

43. Han J, Nichols JH, Rice M, Klonoff DC. The End of the Road for the YSI 2300 Analyzer: Where Do We Go Now? *J Diabetes Sci Technol*. 2020;14(3):595. doi:10.1177/1932296819886603

44. Baird G. Preanalytical considerations in blood gas analysis. *Biochem Medica*. 2013;23(1):19. doi:10.11613/BM.2013.005

45. Dukić L, Kopčinović LM, Dorotić A, Baršić I. Blood gas testing and related measurements: National recommendations on behalf of the Croatian Society of Medical Biochemistry and Laboratory Medicine. *Biochem Medica*. 2016;26(3):318. doi:10.11613/BM.2016.036

46. Froschauer EM, Kolisek M, Dieterich F, Schweigel M, Schweyen RJ. Fluorescence measurements of free [Mg 2+] by use of mag-fura 2 in Salmonella enterica . *FEMS Microbiol Lett*. 2004;237(1):49-55. doi:10.1111/j.1574-6968.2004.tb09677.x

47. Borden WT, Hoffmann R, Stuyver T, Chen B. Dioxygen: What Makes This Triplet Diradical Kinetically Persistent? *J Am Chem Soc*. 2017;139(26):9010-9018. doi:10.1021/JACS.7B04232

48. Charlesworth JM. Optical sensing of oxygen using phosphorescence quenching. *Sensors Actuators B Chem*. 1994;22(1):1-5. doi:10.1016/0925-4005(94)01263-6

49. Zimmermann J, Zeug A, Röder B. A generalization of the Jablonski diagram to account for polarization and anisotropy effects in time-resolved experiments. *Phys Chem Chem Phys*. 2003;5(14):2964-2969. doi:10.1039/B303138A

50. Saini S, Singh H, Bagchi B. *Fluorescence Resonance Energy Transfer (FRET) in Chemistry and Biology: Non-Förster Distance Dependence of the FRET Rate*. Vol 118.; 2006. Accessed January 22, 2020. www.olympusmicro.com/primer/techniques/fluorescence/

51. Bajar BT, Wang ES, Zhang S, Lin MZ, Chu J. A guide to fluorescent protein FRET pairs. *Sensors (Switzerland)*. 2016;16(9). doi:10.3390/s16091488

52. Broussard JA, Rappaz B, Webb DJ, Brown CM. Fluorescence resonance energy transfer microscopy as demonstrated by measuring the activation of the serine/threonine kinase Akt. *Nat Protoc 2013 82*. 2013;8(2):265-281. doi:10.1038/nprot.2012.147

53. Shrestha D, Jenei A, Nagy P, Vereb G, Szöllősi J. Understanding FRET as a research tool for cellular studies. *Int J Mol Sci*. 2015;16(4):6718-6756. doi:10.3390/ijms16046718

54. Müller SM, Galliardt H, Schneider J, Barisas BG, Seidel T, Meckel T. Quantification of Förster resonance energy transfer by monitoring sensitized emission in living plant cells.

Published online 2013. doi:10.3389/fpls.2013.00413

55. Wallace B, Atzberger PJ. Förster resonance energy transfer: Role of diffusion of fluorophore orientation and separation in observed shifts of FRET efficiency. *PLoS One*. 2017;12(5):e0177122. doi:10.1371/journal.pone.0177122

56. Ma L, Yang F, Zheng J. Application of fluorescence resonance energy transfer in protein studies. *J Mol Struct*. 2014;1077:87-100. doi:10.1016/j.molstruc.2013.12.071

57. Betolngar DB, Erard M, Pasquier H, et al. pH sensitivity of FRET reporters based on cyan and yellow fluorescent proteins. *Anal Bioanal Chem*. 2015;407(14):4183-4193. doi:10.1007/s00216-015-8636-z

58. Aoki K, Kiyokawa E, Nakamura T, Matsuda M. Visualization of growth signal transduction cascades in living cells with genetically encoded probes based on Förster resonance energy transfer. *Philos Trans R Soc B Biol Sci*. 2008;363(1500):2143-2151. doi:10.1098/rstb.2008.2267

59. Kelleher MT, Fruhwirth G, Patel G, et al. The potential of optical proteomic technologies to individualize prognosis and guide rational treatment for cancer patients. *Target Oncol*. 2009;4(3):235-252. doi:10.1007/s11523-009-0116-y

60. Brumbaugh J, Schleifenbaum A, Gasch A, Sattler M, Schultz C. A dual parameter FRET probe for measuring PKC and PKA activity in living cells. *J Am Chem Soc*. 2006;128(1):24-25. doi:10.1021/ja0562200

61. Braun DC, Garfield SH, Blumberg PM. Analysis by fluorescence resonance energy transfer of the interaction between ligands and protein kinase Cδ in the intact cell. *J Biol Chem*. 2005;280(9):8164-8171. doi:10.1074/jbc.M413896200

62. Otten J, Tenhaef N, Jansen RP, et al. A FRET-based biosensor for the quantification of glucose in culture supernatants of mL scale microbial cultivations. *Microb Cell Fact*. 2019;18(1):143. doi:10.1186/s12934-019-1193-y

63. Fong J, Khan A. Hypocalcemia: Updates in diagnosis and management for primary care. *Can Fam Physician*. 2012;58(2):158. Accessed August 18, 2021. /pmc/articles/PMC3279267/

64. Beto JA. The Role of Calcium in Human Aging. *Clin Nutr Res*. 2015;4(1):1. doi:10.7762/CNR.2015.4.1.1

65. Calvi LM, Bushinsky DA. When Is It Appropriate to Order an Ionized Calcium? *J Am Soc Nephrol*. 2008;19(7):1257-1260. doi:10.1681/ASN.2007121327

66. Vuralli D. Clinical Approach to Hypocalcemia in Newborn Period and Infancy: Who Should Be Treated? *Int J Pediatr*. 2019;2019:1-7. doi:10.1155/2019/4318075

67. Renaghan AD, Rosner MH. Hypercalcemia: etiology and management. *Nephrol Dial Transplant*. 2018;33(4):549-551. doi:10.1093/ndt/gfy054

68. Felsenfeld AJ, Levine BS. Calcitonin, the forgotten hormone: does it deserve to be forgotten? *Clin Kidney J*. 2015;8(2):180. doi:10.1093/CKJ/SFV011

69. Florencio-Silva R, Sasso GR da S, Sasso-Cerri E, Simões MJ, Cerri PS. Biology of Bone Tissue: Structure, Function, and Factors That Influence Bone Cells. *Biomed Res Int*. 2015;2015. doi:10.1155/2015/421746

70. Fleet JC, Schoch RD. Molecular Mechanisms for Regulation of Intestinal Calcium Absorption by Vitamin D and Other Factors. *Crit Rev Clin Lab Sci*. 2010;47(4):181. doi:10.3109/10408363.2010.536429

71. Veldurthy V, Wei R, Oz L, Dhawan P, Jeon YH, Christakos S. Vitamin D, calcium homeostasis and aging. *Bone Res*. 2016;4:16041. doi:10.1038/BONERES.2016.41

72. Ilahi A, Muco E, Ilahi TB. Anatomy, Head and Neck, Parathyroid. *StatPearls*. Published online August 11, 2021. Accessed August 22, 2021. https://www.ncbi.nlm.nih.gov/books/NBK537203/

73. Seccareccia D. Cancer-related hypercalcemia. *Can Fam Physician*. 2010;56(3):244. Accessed August 18, 2021. /pmc/articles/PMC2837688/

74. Ramos RE de O, Mak MP, Alves MFS, et al. Malignancy-Related Hypercalcemia in Advanced Solid Tumors: Survival Outcomes. *J Glob Oncol*. 2017;3(6):728. doi:10.1200/JGO.2016.006890

75. Kennel KA, Drake MT. Adverse Effects of Bisphosphonates: Implications for Osteoporosis Management. *Mayo Clin Proc*. 2009;84(7):632. doi:10.1016/S0025-6196(11)60752-0

76. Saner FH, Treckmann JW, Geis A, et al. Efficacy and safety of regional citrate anticoagulation in liver transplant patients requiring post-operative renal replacement therapy. *Nephrol Dial Transplant*. 2012;27(4):1651-1657. doi:10.1093/NDT/GFR510

77. Hands JM, Hands JM, Moy LS. Calcium: More Than Bone? Implications for Clinical Practice and Theory. *J Clin Med Res*. 2021;13(5):253-257. doi:10.14740/jocmr.v13i5.4505

78. Relevance of Lactate Threshold in Endurance Sports: A Reiew. Accessed August 23, 2021. https://www.researchgate.net/publication/344088986_RELEVANCE_OF_LACTATE_THRESHOLD_IN_ENDURANCE_SPORTS_A_REVIEW

79. Hamm LL, Nakhoul N, Hering-Smith KS. Acid-Base Homeostasis. *Clin J Am Soc Nephrol*. 2015;10(12):2232. doi:10.2215/CJN.07400715

80. Kellum JA. Determinants of blood pH in health and disease. *Crit Care*. 2000;4(1):6. doi:10.1186/CC644

81. Nattie E, Li A. Central Chemoreceptors: Locations and Functions. *Compr Physiol*. 2012;2(1):221. doi:10.1002/CPHY.C100083

82. Wong-Riley MTT, Liu Q, Gao X. Peripheral-central chemoreceptor interaction and the significance of a critical period in the development of respiratory control. *Respir Physiol Neurobiol*. 2013;185(1):156. doi:10.1016/J.RESP.2012.05.026

83. Koeppen BM. The kidney and acid-base regulation. *Adv Physiol Educ*. 2009;33:275-281. doi:10.1152/advan.00054.2009.-Since

84. Rose IA, Warms JVB. Control of Glycolysis in the Human Red Blood Cell*. *J Biol Chem*. 1966;241(21):4848-4854. doi:10.1016/S0021-9258(18)99643-2

85. Gojda J, Waldauf P, Hrušková N, et al. Lactate production without hypoxia in skeletal muscle during electrical cycling: Crossover study of femoral venous-arterial differences in healthy volunteers. *PLoS One*. 2019;14(3):e0200228. doi:10.1371/JOURNAL.PONE.0200228

86. Lee SM, An WS. New clinical criteria for septic shock: serum lactate level as new emerging vital sign. *J Thorac Dis*. 2016;8(7):1388-1390. doi:10.21037/JTD.2016.05.55

87. Klein R, Nagy O, Tóthová C, Chovanová F. Clinical and Diagnostic Significance of Lactate Dehydrogenase and Its Isoenzymes in Animals. *Vet Med Int*. 2020;2020. doi:10.1155/2020/5346483

88. Dror N, Weidling J, White S, et al. Clinical evaluation of a novel subcutaneous lactate monitor. *J Clin Monit Comput*. Published online 2021. doi:10.1007/s10877-021-00685-1

89. Garcia-Alvarez M, Marik P, Bellomo R. Sepsis-associated hyperlactatemia. *Crit Care*.

2014;18(5). doi:10.1186/S13054-014-0503-3

90.   Tachedjian G, Aldunate M, Bradshaw CS, Cone RA. The role of lactic acid production by probiotic Lactobacillus species in vaginal health. *Res Microbiol*. 2017;168(9-10):782-792. doi:10.1016/J.RESMIC.2017.04.001

91.   Talley K, Alexov E. On the pH-optimum of activity and stability of proteins. *Proteins*. 2010;78(12):2699. doi:10.1002/PROT.22786

92.   Aoi W, Marunaka Y. Importance of pH Homeostasis in Metabolic Health and Diseases: Crucial Role of Membrane Proton Transport. *Biomed Res Int*. 2014;2014. doi:10.1155/2014/598986

CHAPTER 2: PHOTOSTABLE AND PROTEOLYSIS-RESISTANT FÖRSTER RESONANCE ENERGY TRANSFER-BASED CALCIUM BIOSENSOR

Dat Nguyen[£], Danielle M. Behrens[£,Ψ], Sanjana Sen[¥, Ψ], Avid Najdahmadi[ꟲ], Jessica N. Pham[†], Gaetano Speciale[†], Micah M. Lawrence[£], Sudipta Majumdar[†], Gregory A. Weiss[†,¥, β,*] , Elliot L. Botvinick[£,ꟲ,ξ,*]

[Ψ]Contributed equally

[£]Department of Biomedical Engineering, University of California, Irvine, CA 92697-2730 USA.

[¥]Department of Molecular Biology & Biochemistry, University of California, Irvine, California 92697-3900, USA.

[ꟲ]Beckman Laser Institute and Medical Clinic, University of California, Irvine, CA 92612-1475, USA

[†]Department of Chemistry, University of California, Irvine, Irvine, California 92697-2015, USA

[β]Department of Pharmaceutical Sciences, University of California, Irvine, California 92697-4625, USA.

[ξ]Department of Surgery, University of California, Irvine, CA 92697-2730, USA.

*Corresponding Authors; email addresses: elliot.botvinick@uci.edu, gweiss@uci.edu

2. 1 Abstract

Molecular sensors from protein engineering offer new methods to sensitively bind to and detect target analytes for a wide range of applications. For example, these sensors can be integrated into probes for implantation, and then yield new and valuable physiological information. Here, a new Förster Resonance Energy Transfer (FRET)-based sensor is integrated with an optical fiber to yield a device measuring free Ca^{2+}. This membrane-encapsulated optical fiber (MEOF) device is composed of a sensor-matrix that fills polytetrafluoroethylene (PTFE) with an engineered Troponin C (TnC) protein fused to a pair of FRET fluorophores. The FRET efficiency is modulated upon Ca^{2+} ion binding. The probe further comprises a second, size-excluding filter-membrane that is synthesized by filling the pores of an PTFE matrix with a polyethylene glycol dimethacrylate (PEGDMA) hydrogel; this design ensures protection from circulating proteases and the foreign body response. The two membranes are stacked and placed on a thin, silica optical fiber for optical excitation and detection. Results show the biosensor responds to changes in Ca^{2+} concentration within minutes with a sensitivity ranging from 0.01 to 10 mM Ca^{2+}, allowing discrimination of hyper and hypocalcemia. Furthermore, the system reversibly binds Ca^{2+} to allow continuous monitoring. This work paves the way for the use of engineered structure-switching proteins for continuous optical monitoring in a large number of applications.

2.2 Introduction

The development of continuous biomedical sensors provides clinicians and researchers real-time data on clinically relevant and new physiological signals.[1] Currently, the catalog of continuous sensors is vastly outweighed by the number of clinically relevant analytes, which are largely analyzed with point-of-care (POC) devices or at clinical laboratories. For example, ionized calcium (Ca^{2+}), an essential mineral for muscle contraction, bone development, nerve impulses, blood clotting, and regulating heart beat propagation, is assayed by a calcium blood test; this test

requires a healthcare professional to draw blood from a patient's median cubital vein and send it to a clinical laboratory for a complete metabolic panel analysis.[2,3] The time between depositing a sample and receiving results may be several hours, or approximately one hour in emergency cases. To eliminate the latency caused by hospital lab delay, POC devices such as Abbott I-STAT can perform on-site assays, including Ca^{2+}, providing results within a few minutes. However, the frequency of assay is still dependent upon typically infrequent, professional blood draws. Though laboratory assays of Ca^{2+} are precise and accurate, the measurements are intermittent as compared to physiological Ca^{2+} dynamics. For example, in clinical cases, such as rapid blood transfusion during liver transplantations, Ca^{2+} concentrations can exhibit rapid transients at very low concentrations (e.g., drops by 0.1 mM Ca^{2+} in 5 min), underlying the need for a continuous Ca^{2+} sensor.[2,3]

Advances in protein engineering have yielded new classes of binding macromolecules that display exquisite ligand binding specificity and yield quantifiable signals upon such ligand or target binding.[4,5] For example, Maeshime, et al. developed a Förster Resonance Energy Transfer (FRET)-based molecular Mg^{2+} sensor to monitor Mg^{2+} dynamics during the cell cycle. This sensor comprises the structure-switching *Escherichia coli* (*E. coli*) Mg^{2+} transporter CorA (CorA-CD) positioned between the fluorescent proteins (FPs) enhanced cyan fluorescent protein (eCFP) and Venus (a variant of yellow fluorescent protein, YFP).[6] Furthermore, a genetically encoded calcium indicator, termed Cameleon, has been reported; this sensor joins structure-switching calmodulin (CaM) and CaM-binding peptides of Myosin Light-Chain Kinase positioned between eCFP and eYFP to monitor intracellular calcium.[7] These FRET sensors demonstrate the specificity and sensitivity of genetically encoded protein biosensors.

Here, the calcium FRET sensor Twitch-2B is considered for use in a continuous Ca^{2+} monitor. Twitch-2B was developed by Thestrup et al. for intracellular monitoring of Ca^{2+} transients during T-lymphocyte activation and action potential propagation in mouse cortical neurons.[8] Twitch-2B is derived from toadfish *Opsanus tau* Troponin C (TnC), a muscular actin-associated protein that undergoes structure-switching upon Ca^{2+} binding. Twitch-2B comprises a modified TnC (equilibrium dissociation constant for Ca^{2+}, $K_D = 200$ nM) space with linkers, each fused at their free ends to the FPs mCerulean3 (cyan FP variant) and cpVenus[cd] (yellow FP variant), at the N- and C-termini, respectively.[8] Twitch-2B was determined to be a candidate sensing molecule for a continuous physiological Ca^{2+} probe because of its reversible binding kinetics, stability in vivo, and sensitivity to varying Ca^{2+}concentrations.

A number of calcium sensing modalities have been developed to monitor calcium. Asif et al. developed an electro-chemical sensor to Ca^{2+} comprising functionalized biocompatible ZnO nanorods. In vitro testing shows a log-linear relationship between sensor voltage and Ca^{2+} ranging from 100 nM to 10 mM.[10] Shortreed et al. functionalized the distal end of an optical fiber with the calcium sensitive dye Calcium Green and reported a unique emission spectrum for Ca^{2+} concentrations ranging from 37.6 nM to 39.8 µM.[11]

These reported strategies lack a method to prevent interactions with physiological macromolecules, including antibodies, proteases, and other soluble proteins, upon device implantation. Proteins from the foreign body response (FBR) can foul the surface and adversely affect sensing for in vivo applications.[12] In consideration of an implantable Ca^{2+} sensor , a new type of Ca^{2+} sensor is presented that combines a FRET-based sensing molecule with a new membrane to provide the requisite protection for in vivo applications.

An optical fiber device was developed and referred to here as the membrane-encapsulated optical fiber (MEOF, **Figure 2.1**). MEOF first comprises a hydrophilic polytetrafluoroethylene (PTFE) sheet impregnated with a solution of a protein FRET sensor and placed in contact with the end of an optical fiber. MEOF also includes an outer membrane composed of a size-selective polyethylene glycol dimethacrylate (PEGDMA) 2000 hydrogel interpenetrating a second PTFE sheet. Results are presented for Ca^{2+}-sensing MEOF wherein the FRET sensor is a new photo-resilient variant of Twitch-2B, SNAP-Twitch-2B-CLIP (STC), which replaces the readily photobleached FPs with photostable Alexa Fluor 488 and Alex Fluor 546 as the donor and acceptor fluorophore, respectively.[13] This Ca^{2+} probe shows a reversible response curve for concentrations ranging between 0.01 mM to 10 mM, and is photostable over prolonged excitation scans, a necessary capability for future implantation. The probe also operates in real-time, which is critical for a continuous Ca^{2+} biosensor.
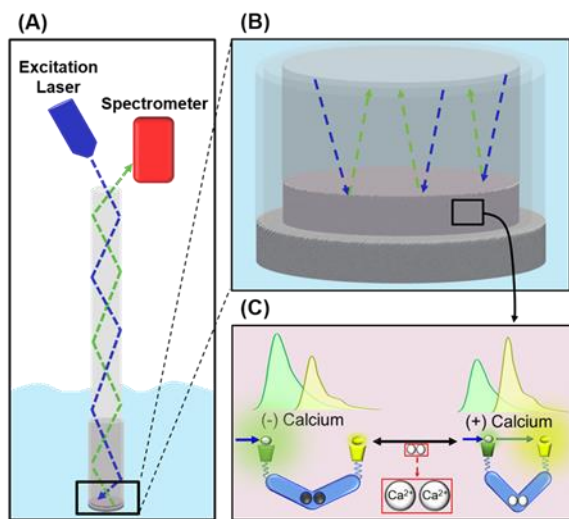
Figure 2.1. Schematic of the FRET calcium ion probe. (A) Excitation light results in a FRET signal analyzed by a spectrometer. (B) A size-excluding filter-membrane and sensor-matrix encapsulate the optical fiber. (C) The FRET signal is modulated by calcium ion concentration.

2.3 Experimental Section

2.3.1 Filter-Membrane Fabrication

Monomeric PEGDMA 2000 precursor (Sigma Aldrich) and Milli-Q water were mixed with a

flea-sized micro stirring bar (Grainger) in a 30%/70% (*w/w*) ratio in a dark room until a

homogenous solution was obtained. Photoinitiator 2-Hydroxy-4′-(2-hydroxyethoxy)-2-

methylpropiophenone (Irgacure 2959, Sigma Aldrich) was then mixed at 1% (*w/w*) and

illuminated by a UV (365 nm), 8 W VWR Dual UV Transilluminator for 10 min to form a

hydrogel. Subsequently, filter-membranes were fabricated by polymerizing the hydrogel

precursor solution while in PTFE (FHLC01300, 80% porosity, 0.45 µm pore size, 145 µm thick,

Sigma Aldrich).

2.3.2 Permeability Testing

Permeability of hydrogels was tested using 3 mm diameter disks of PEGDMA 2000. The

hydrogels were first allowed to swell overnight in Phosphate Buffered Saline Solution (PBS, pH

7.4, Thermo Fischer Scientific). Swelling reaches a steady state in 5 h (Supporting Information,

Figure S2.1). The swollen hydrogels were then placed in a custom-made rubber chamber (frame

size: 20 mm x 20 mm, mat opening: 15 mm x 15 mm, height: 1 mm McMaster-Carr), and

incubated in PBS solutions containing Alexa Fluor 488 - labeled insulin (5.8 kDa, Supporting

Information) or Precision Plus Protein Kaleidoscope Prestained Protein Standards (Bio-Rad; 10

kDa to 250 kDa) for 30 min.[13] Confocal microscopy was performed using either a Leica Sp8 or

Zeiss LSM700 inverted microscope using 488 and 633 nm laser lines and a 10x or 20x objective

lens. Emission was collected from 520 to 700 nm and 650 to 700 nm under 488 and 633 nm laser

line excitation, respectively. Images were acquired every 30 s.

The permeability of the filter-membranes was tested by first creating 1 mm PTFE disks with a 1

mm biopsy punch (World Precision Instruments). The disks were then glued (Loctite 4981,

Henkel) to the face of MRE-025 microrenathane tubing (ID: 0.30 mm, OD: 0.63 mm, Braintree

Scientific) and the hydrogel precursor solution was polymerized within the pores of the PTFE. A bare optical fiber (FG200LEA, 0.22 NA, 200 µm core, 220 µm cladding, Thor Labs) was guided down the tubing and placed in contact with the membrane. Loctite 4981 glue was used to seal the backend of the silica optical fiber to the microrenathane tubing. The distal end of each optical fiber terminated in an SMA thread and was coupled to a custom benchtop spectrometer apparatus (**Figure S2.2**). A set of membrane-fiber units were fabricated for each test solution described below. After incubation in PBS, the tip of each optical fiber construct was immersed in a solution containing fluorescein (FITC, 389.4 Da, Sigma Aldrich), green fluorescent protein (GFP, 26.9 kDa), Alexa Fluor 488 - labeled insulin (5.8 kDa) or fluorescein isothiocyanate-dextran (3-5 kDa or 150 kDa, Sigma Aldrich).[14,15]
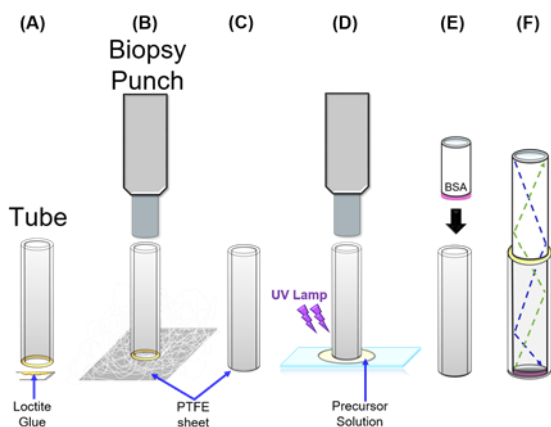
Figure 2.2. Fabrication of the membrane-encapsulated optical fiber (MEOF). (A) Microrenathane tubing is cut, and Loctite 4981glue is applied by a small needle to its tip. The tubing is placed onto a sheet of PTFE cut by biopsy punch (B) to produce a capped tube (C). PEGDMA 2000 hydrogel precursor solution is allowed to impregnate the PTFE sheet (D) such that after polymerization, a hybrid PEGDMA2000/PTFE membrane is produced. An optical fiber guides an PTFE sheet, wetted with FRET protein solution (shown in pink), to the end of the tubbing (E) and then sealed on the back end with Loctite 2981 glue (F).

2.3.3 Fabrication of the Membrane-Encapsulated Optical Fiber (MEOF)

MEOF probes were fabricated as illustrated in **Figure 2.2**. Microrenathane tubing was cut into 5 mm segments (**Figure 2.2A**), and the glue was then applied to the bottom annulus of the tubing

(Figure 2A) to adhere the tubing to a PTFE sheet (**Figure 2.2B).** A 1 mm biopsy punch was slipped over the tubing to cut the PTFE sheet into a circle of 1 mm diameter. (**Figure 2.2C**). Next, the hydrogel precursor solution was pipetted on a glass slide and the PTFE-capped tubing was pressed into the solution. The hydrogel precursor solution permeates throughout the PTFE due to their compatible hydrophilicity and was polymerized with a 365 nm 8 W VWR Dual UV Transilluminator for 10 min, producing a membrane-capped tube (**Figure 2.2D).** A second hydrophilic PTFE sheet was wetted with 2 µL of FRET sensor solution (4 mg/mL) by first pipetting the FRET protein solution onto the PTFE material and then compressing this sheet between two microscope slides to form the sensor-matrix. In parallel, a silica optical fiber was incubated overnight in a 2% bovine serum albumin (BSA, Chromatopur) /water solution to block the optical fiber's surface and prevent surface-induced aggregation of the FRET sensor. Next, the sensor-matrix was placed onto the tip of the BSA-coated optical fiber (**Figure 2.2E**) and the assembly was pushed through the tubing until it contacted the filter-membrane (**Figure 2.2F**). Glue was used to seal the backend of the silica optical fiber to the microrenathane tubing, and the resulting MEOF was incubated in protein buffer media at 4°C for at least 5 h. The assembly quality was assessed by MEOFs encapsulating GFP to monitor for leakage. These MEOFs were incubated in 4-(2-hydroxyethyl)-1-piperazineethanesulfonic acid (HEPES) buffer for 5 h (**Figure S2.3**), and the solution was tested for leaking GFP using a fluorescent plate reader (Spark, TECAN). No signal intensity was observed, confirming encapsulation of the protein within the sensor-matrix.

2.3.4 FRET Calcium Sensing

Each spectral measurement was acquired in triplicate with exposure times of 100 ms for the Twitch-2B sensor or 2 s for the STC sensor. Back-ground (dark signal)-subtracted spectra were

processed in MATLAB. Custom MATLAB code was used to process the digitized signals and calculate the FRET ratiometric signal, which here is defined as the peak acceptor intensity signal divided by the peak donor intensity signal ($I_{acceptor}/I_{donor}$), a metric commonly used to quantify FRET efficiency.[16]

Calcium solutions ($CaCl_2*2H_2O$, Sigma Aldrich) at the indicated concentration were placed in microcentrifuge tubes capped with parafilm to prevent evaporation. MEOF probes were tested by dipping the devices into these calcium solutions. GraphPad Prism was used for to fit data points onto nonlinear regression models and for statistical analysis.

2.4 Results and Discussion

2.4.1 Characterization of the Filter-Membrane

A well-known event, the FBR activates upon device implantation.[12] Of particular importance to the MEOF Ca^{2+} probe, the FBR recruits immune cells that secrete proteases, which could cleave the Twitch-2B and render the device inoperable. Thus, the device must exclude protease access to the molecular sensor.

Here, PEG hydrogels are formulated to size-exclude proteases secreted by immune cells. Such proteases are considerably smaller than immunoglobulins (~150 kDa), and much larger than calcium ions.[17] The smallest of these known proteases is Chymase, which has a MW of approximately 30 kDa.[18] PEG-derived hydrogels were selected for protein exclusion due to the tunability of their mesh size, swelling, and tensile strength.[19,20] Additionally, PEG is considered to be generally nonfouling and biocompatible.[21] Screening of various PEG formulations and derivates lead to the selection of PEGDMA 2000 hydrogels, formulated as described in the Experimental Section, and were shown to exclude proteins as small as 10 kDa, but permit transport of insulin (5.8 kDa). Fluorescence signals from the fluorescently labeled insulin at the

hydrogel/fluid interface show very rapid kinetics (**Figure 2.3A,2.3C**); in comparison, the 10 kDa

and larger proteins show no penetration of the hydrogel as measured by fluorescence (**Figure

2.3B, 2.3C**).
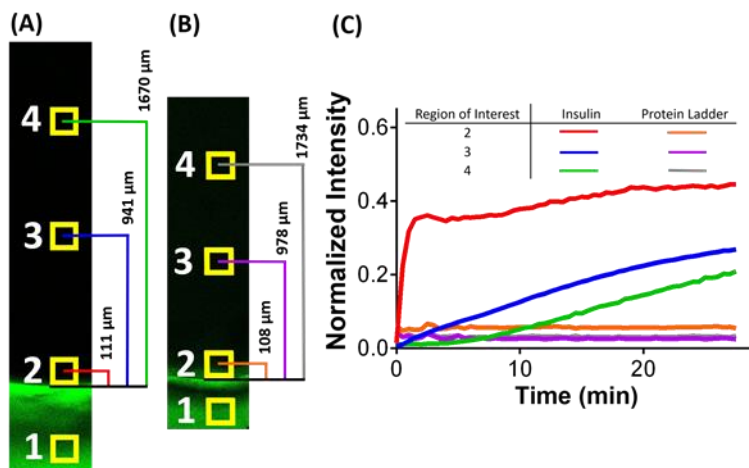
Figure 2.3. Examining the permeability of the PEGDMA 2000 hydrogel. (A) Confocal
micrographs of the PEGDMA 2000 hydrogel surrounded by Alexa Fluor 488-labeled insulin
(20X image) or (B) a protein ladder (Bio-Rad Protein Kaleidoscope; 10X image) were captured
at t = 0. (C) Intensity profiles highlight permeabilization by proteins into the indicated regions of
interests (ROIs) over time with normalization for fluorescence in ROI 1. ImageJ software was
used to analyze ROI intensity.

The PEGDMA 2000 hydrogels are very soft when hydrated, however and too fragile to place on

the tip of a probe for implantation. Thus, a protective PTFE layer was devised. The hydrogel

precursor solution was polymerized within the non-solid phase of commercially available

hydrophilic PTFE sheets. Scanning electron microscopy (FEI Magellan 400 XHR, Electron

Microscopy Solutions) after iridium sputter coating (10nm, EMS 150T, Electron Microscopy

Solutions) reveal the natural porosity of PTFE sheets (**Figure 2.4A**) and their impregnation by

the PEGDMA 2000 hydrogel (**Figure 2.4B**).This composite, termed the filter-membrane,

combines the size-exclusion properties of the PEGDMA 2000 hydrogel with the durability of

PTFE sheets, and offers a robust composite material for the tip of the Ca^{2+} sensing device.
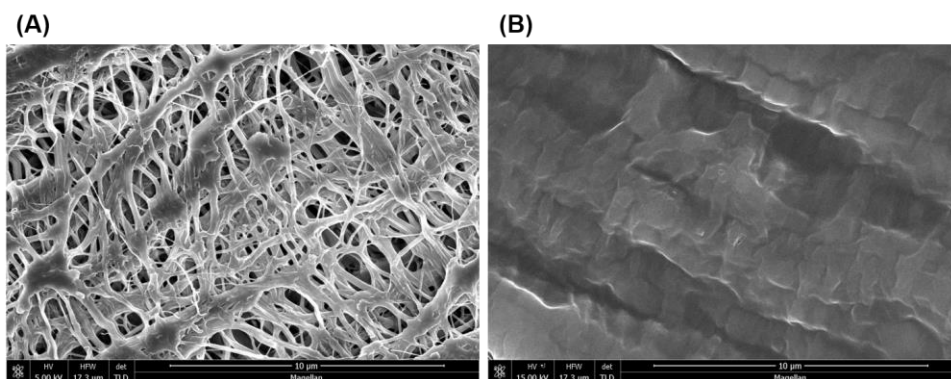
Figure 2.4. SEM images of PTFE and the filter-membrane. Scale Bar = 10 µm. A) The PTFE sheets contain 0.45 µm pores that are infiltrated with PEGDMA 2000 hydrogels (B) after UV polymerization.

Filter-membranes were tested to ensure they retain the size selectivity of the hydrogel alone. For each test, a filter-membrane was coupled to the end of an optical fiber as described in the Experimental Section. **Figure 2.5A** reports that FITC, 3-5 kDa fluorescein isothiocyanate-dextran and Alexa Fluor 488–labeled insulin can diffuse through the filter-membrane, while large macromolecules GFP and 150 kDa fluorescein isothiocyanate-dextran cannot. **Figures S2.4A** and **S2.4B** display the time-dependent emission spectra of Alexa Fluor 488 – labeled insulin and GFP. These results show the filter-membrane retains the size-exclusion properties of the hydrogel.

(A)

	Fluorescein	Dextran	Insulin	GFP	Dextran
Molecular Weight (kDa)	0.38	3-5	5.8	26.9	150
Membrane Permeable?	Yes	Yes	Yes	No	No

Figure 2.5. Properties of the filter-membrane. (A) Tabulated permeability results indicate the observed penetration by fluorescently labeled analytes.

2.4.2 Twitch-2B Ca^{2+} Probe

Calcium sensing membrane-encapsulated optical fiber (MEOF) biosensors were fabricated as detailed in the Experimental Section, where the FRET molecular sensor was Twitch-2B. Important to the FRET sensor, the sensor-matrix allows Twitch-2B to remain in solution, preserving Twitch-2B structure-switching upon Ca^{2+} binding and unbinding. The resulting MEOF probe has the following key properties. 1) enabling the passage of small target analytes (e.g., ions and small peptides) yet exclusion of larger proteins (such as serine proteases), 2) allowing FRET sensors to undergo conformational changes upon binding and releasing target analytes, and 3) guiding excitation light to the sensor-matrix and fluorescently emitted light to the spectrometer.

2.4.3 In Vitro Testing of MEOF Ca^{2+} Probes

To determine the efficacy of the Twitch-2B MEOF Ca^{2+} probe, probes were incubated in test buffer (25 mM 3-(N-morpholino) propanesulfonic acid (MOPS), 100 mM KCl, pH 7.6) supplemented with increasing concentrations of Ca^{2+}. For each measurement, 0.7 µW of 405 nm laser light was used to excite the protein sensor for 100 ms. Results show the FRET ratio ($I_{acceptor}$ / I_{donor}) being sensitive to increasing Ca^{2+} concentration from 0 to 14 mM, above which the sensor response saturates (**Figure 2.6A**). Importantly, the MEOF sensor responds in the physiological concentration range of Ca^{2+}; normal non-protein bound Ca^{2+} concentration in human blood plasma ranges from 1.1 to 1.3 mM with pathological values ranging from 0.33 mM (hypocalcemia) to 2.5 mM (hypercalcemia).[11,22,23] The probe-response curve was fit to a Hill equation, which determined the K_D and Hill constant to be 2.3 mM and 0.78, respectively (R^2 (Coefficient of Determination) = 0.99, Sy.x (Standard Error of the Estimate) = 0.07) consistent with binding affinity in a useful range. These results demonstrate that the intracellular FRET sensor Twitch-2B can be adapted to function in a hand-held optical device.
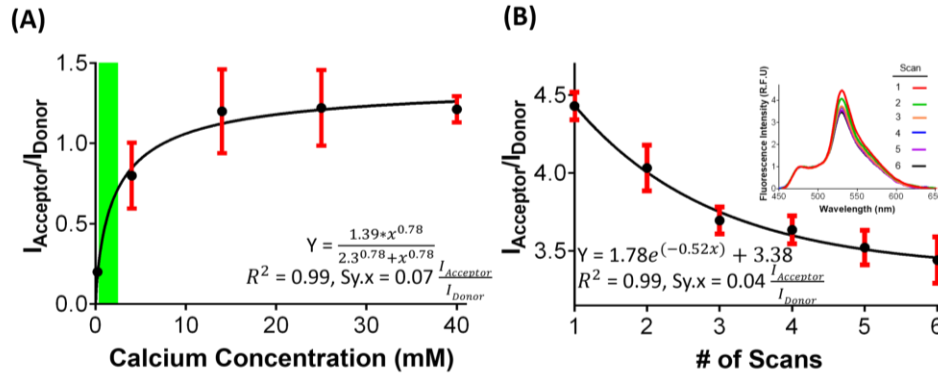
Figure 2.6. Efficacy of Twitch2B to sense calcium ions. (A) The dose-dependent response of the MEOF and its data fit to a Hill equation demonstrates the MEOF's usefulness for sensing physiological concentrations of Ca^{2+} (green). $I_{acceptor}/I_{donor}$ is the emission ratio after subtracting the spectra for calcium ion-free MOPS buffer. (B) Photobleaching of mCerulean3 and cpVenus[cd] in calcium-free MOPS buffer is significant and renders Twitch2B inappropriate for a MEOF calcium ion monitor; the inset depicts the emission spectra normalized by mCerulean3 peak intensity.

However, the Twitch-2B accepter fluorophore, cpVenus[cd] (a YFP derivative) is susceptible to photobleaching, particularly as compared to the donor fluorophore mCerulean3 (a CFP derivative).[24] The photostability of the Twitch-2B MEOF device was therefore investigated by repeated exposure to 405 nm while in calcium-free test buffer. The FRET ratio was measured after each exposure and showed significant photobleaching over time (**Figure 2.6B**), following an exponential decay in FRET ratio ($R^2 = 0.99$, Sy.x = 0.04), as expected for exponential photobleaching.[25,26] Further, it has been shown that the CFP-YFP FRET pair may suffer from phototoxicity when excited with violet wavelengths, resulting in inactivation of the FRET pair.[24] To account for possible effects specific to the MEOF, photobleaching experiments were conducted using solutions of Twitch-2B. Twitch-2B solutions were exposed to 45 mW, 405 nm laser light for three min; a non-illuminated solution served as a negative control. Solutions were analyzed with the spectroscopic fluorescent plate reader under three conditions: donor excitation in test buffer, acceptor excitation in test buffer, and donor excitation in test buffer supplemented

with CaCl$_2$. Spectroscopic data (**Figure S2.5**) confirm photobleaching and consequential loss of sensitivity to Ca^{2+}.

2.4.4 The Development of a Photostable Twitch-2B FRET Construct

To overcome cpVenus^{cd} photobleaching during MEOF measurements, photostable fluorescent molecules were sought to replace the mCerulean3-cpVenus^{cd} FRET pair. Small molecule Alexa Fluor dyes are highly suitable candidates for the MEOF FRET sensor as they provide greater photostability and brightness compared to genetically encoded fluorescent proteins and other fluorescent dyes like Cy3 and fluorescein.[27,28] To conjugate Alexa Fluor dyes, genetically-encoded SNAP- and CLIP-tags were integrated into Twitch-2B. SNAP and CLIP-tags, both derived from the human O^6-alkylguanine transferase; catalyze the covalent attachment of an O^6-benzylguanine (O^6-BG) and O^6-benzylcytosine (O^6-BC), respectively.[33]
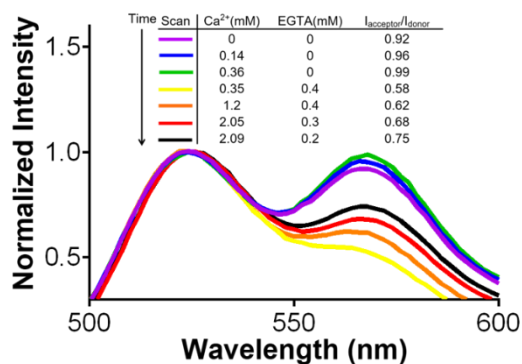
Figure 2.7. STC Ca^{2+} response in a fluorescence plate reader normalized by Alexa Fluor 488 peak intensity. The FRET ratio response is sensitive to increasing concentrations of Ca^{2+}.

The Twitch-2B sensor was reengineered with SNAP and CLIP tags flanking its N- and C termini, resulting in, SNAP-Twitch-2B-CLIP, termed STC. The plasmid encoding STC and plasmid map are shown in **Figure S2.6** and **S2.7**. The new construct was expressed at high yields and purified using affinity and size exclusion chromatography (**Figure S2.8A**). Commercially

available O^6-BG Alexa Fluor 488 and O^6-BC-Alexa Fluor 546-BC (New England Biolabs) were covalently attached onto the SNAP and CLIP tags of STC (Figure S8B, S8C), and the FRET construct retained its dose-dependent response to Ca^{2+} in a 96-well fluorescent plate assays (**Figure 2.7).** The STC construct was, henceforth, used in further investigations of the MEOF probes.

2.4.5 Characterization of MEOF Probes with the STC Construct

Here, probe photostability was assessed using a 450 nm laser light to excite the donor fluorophore Alexa Fluor 488. Each MEOF was incubated in Reference Buffer (RB, 50 mM HEPES, 50 mM NaCl, 10% glycerol, 10 mM β-mercaptoethanol (βME), pH 7.6) and exposed to 0.71 mW laser for 2 s per reading. Laser light energy per measurement is 20E3 times greater for STC as compared to Twitch-2B. No significant FRET ratio change was observed during the experiment (**Figure 2.8A**, Relative Standard Deviation, RSD = 0.57%). Thus, integration of the new donor and acceptor fluorophores provide sufficient photostability for continuous Ca^{2+} monitoring.

The sensor rise time was assessed by first incubating MEOF probes in RB and then in RB supplemented with 1.25 mM $CaCl_2$. The FRET ratio was recorded every 3 min for 30 min after media exchange. The data follow an exponential plateau function ($R^2 = 0.98$, Sy.x = 0.004) with a rise time of approximately 6 min, without detectable photobleaching within the plateau (RSD = 0.47%) (**Figure 2.8B**). The 6 min rise time is similar to that of commercial analytical devices, for example, continuous glucose monitors, known to be effective in guiding treatment of conditions having rapid and slow transients such as seen in type 1 diabetes.[35]

Next, MEOF probes were incubated in RB solutions having Ca^{2+} concentration ranging from 0 to 20 mM. The data shows sensitivity to Ca^{2+} across the measured range (0.01 mM to 10 mM), and

a functional form consistent with the Hill equation (Figure 8C; $R^2 = 0.99$, Sy.x = 0.01) having a

Hill constant and K_D values of 0.4 and 0.1 mM, respectively. As indicated by the green region in

Figure 2.8C, the MEOF is sensitive across the physiological range of ionized Ca^{2+} concentration

in the blood, and extends the dynamic range of the Ca^{2+} sensing modalities previously

mentioned.[11-13] This extended sensitivity range correlates with the Hill constant being less than

one, affording a stretched linear region of sensitivity.[36]
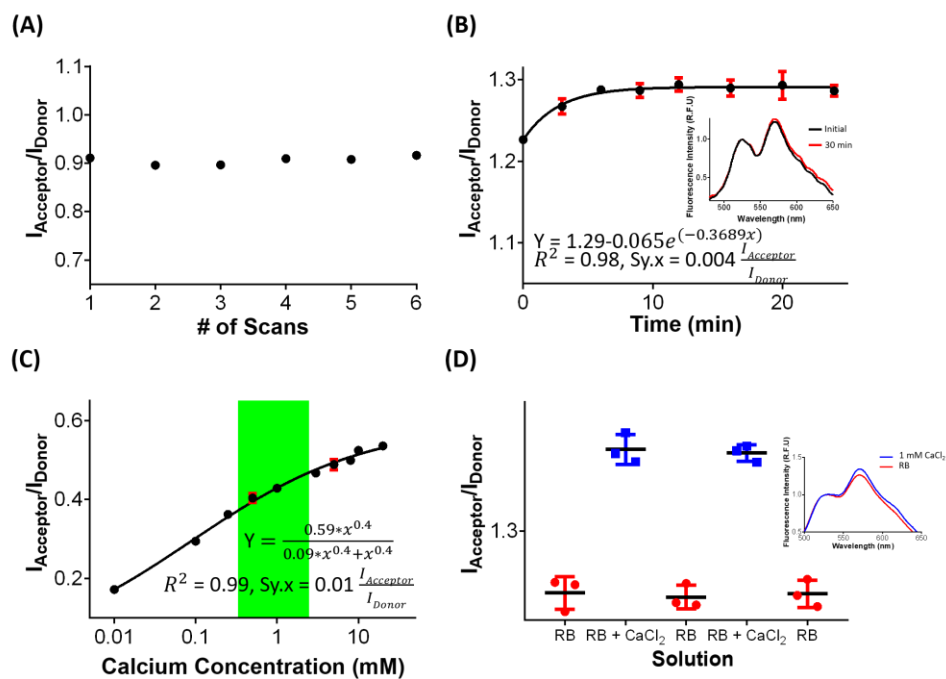
Figure 2.8. Ca^{2+} sensing with the MEOF probe. (A) The STC exhibits excellent stability in reference buffer. (B) Steady state measurements are observed 6 min after the addition of calcium ions; the inset depicts the emission spectra normalized by donor peak intensity. (C) The STC exhibits a dose-dependent response, and the data fits to a Hill equation. $I_{acceptor}/I_{donor}$ is emission ratio after subtracting spectra in calcium ion-free RB. (D) The MEOF device has excellent reproducibility after serial exposures to either buffer supplemented with Ca^{2+} (1 mM) or RB.

To test for sensor reversibility, MEOF probes were serially placed in RB solutions with or

without 1 mM CaCl₂ (**Figure 2.8D**). A one-way ANOVA was conducted to compare effects of

Ca^{2+} on FRET ratio. There was a significant effect of Ca^{2+} across all groups (P < 0.0001). The

Tukey post-hoc comparison with adjusted P values shows no significant differences between the

three RB solution groups or the two RB + 1 mM $CaCl_2$ groups ($p \geq 0.99$ for each comparison), but significant differences between each pairing of RB or RB + 1 mM $CaCl_2$ groups ($p < 0.0001$ for each comparison). Notably, sensor dynamics are considerably slower when comparing Ca^{2+} unbinding (**Figure S2.9**) to binding (**Figure 2.8B**). Although the cytoplasmic Twitch-2B has previously demonstrated rapid unbinding kinetics *in cellulo*, cells contain orders of magnitude lower calcium concentration as compared to the blood and contain unique pumps and transporters that rapidly reduce cytoplasmic Ca^{2+} concentration.[37] And so, it is unsurprising that MEOF fall-times are relatively long given the passive diffusion of Ca^{2+} ions at concentrations mimicking the blood.

2.4.6 Protection from Proteolytic Enzymes
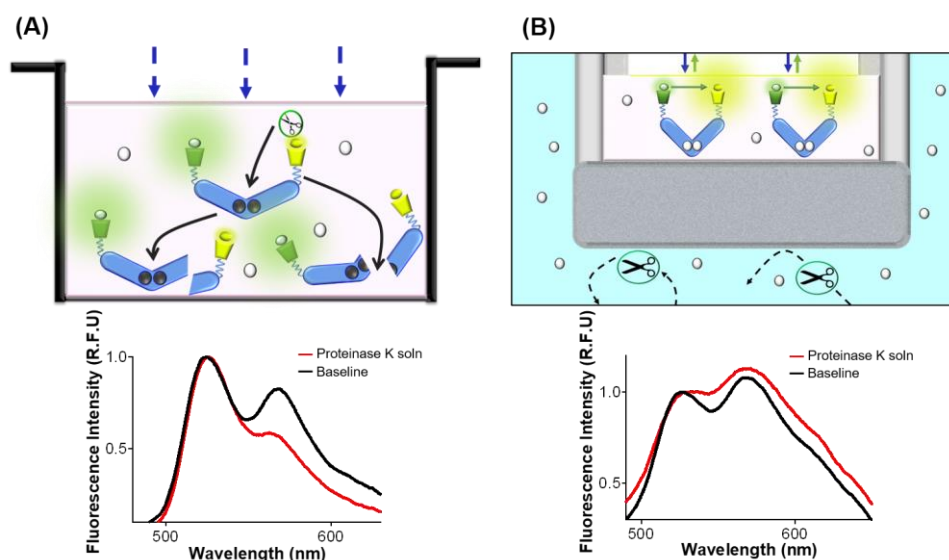
Figure 2.9. Sensor Isolation from Proteinase K. (A) Proteinase K cleaves STC resulting in a diminished acceptor intensity signal. (B) However, the MEOF successfully protects the protein sensor as demonstrated by the observed increase in FRET efficiency.

To model immune system proteolytic enzymes secretion during the FBR, the STC MEOF was incubated with the endopeptidase serine protease Proteinase K (28.9 kDa, New England

Biolabs).[38] The solution comprises 692 µM proteinase K in a solution of 20 mM Tris-HCl, 1 mM CaCl$_2$ and 50% glycerol by volume. Emission spectra confirm that proteinase K in the Ca^{2+} solution rapidly cleaves the STC and results in a 26% loss in acceptor fluorescence (**Figure 2.9A**). Conversely, uncleaved STC should show an increase in acceptor fluorescence over time due to FRET. This increase is observed for the MEOF incubated in the proteinase K solution for 30 min, demonstrating that the filter-membrane successfully excludes the proteinase K (**Figure 2.9B**). These findings highlight the need for and the key role of the size-excluding filter-membrane to circumvent the FBR.

2.5 Conclusion

This effort has produced an optical fiber-based probe, MEOF, designed for prolonged measurements of Ca^{2+} concentrations in vivo. Such capabilities result from (1) encapsulating protein FRET sensors within the pores of a mechanically robust PTFE sheet, such that FRET sensors are free to undergo conformation changes, (2) excluding host proteases by a hybrid PTFE-PEGDMA membrane, and (3) elimination of deleterious photobleaching of FPs in the Twitch-2B FRET sensor by installing small molecules for the donor and acceptor FPs, respectively. This approach is generalizable to the larger class of protein FRET sensors (e.g. ATP and Zn^{2+}).[39,40] Further, the molecular weight cut off properties of the hybrid filter-membrane can be tuned for other applications or FRET sensors by new hydrogel formulation comprising PEG derivatives, or other commonly used hydrogels such as alginate and hyaluronic acid. In summary, the MEOF probe can be easily adopted to include new FRET sensors to generate a new class of analytical probes.

2.6 Acknowledgements

2.7 Supporting Information

2.7.1 Expression and Purification of SNAP-Twitch-2B-CLIP (STC)

Plasmids encoding STC were transformed into chemically competent BL21(DE3)* *E. coli* cells.

After the cells were transferred to LB plates supplemented with carbenicillin (0.050 mg/mL), the

cells were incubated at 37 °C for 12-18 h. An individual colony from the transformation plate

was inoculated with LB (70 mL) supplemented with carbenicillin (0.050 mg/mL). The flasks

were incubated at 37 °C with shaking at 220 rpm for 12-18 h. This seed culture (15 mL) was

transferred into LB (1 L) supplemented with carbenicillin (0.050 mg/mL) before incubation at 37

°C with shaking at 220 rpm. Upon reaching a cell density of OD_{600} between 0.50 and 0.56, the

culture was induced through addition of IPTG (0.5 mM) before incubation at 25 °C with shaking

at 225 rpm for 6 h. The cultures were centrifuged at 6084.1 rcf at 4 °C for 20 min. The

supernatant was discarded, and the cell pellet was resuspended in lysis buffer (20 mL of 50 mM

HEPES buffer, 300 mM NaCl, 10 mM β-mercaptoethanol (βME), pH 7.6). A protease inhibitor

cocktail (HALT) was added to the suspended cells at the manufacturer's recommended

concentration, and the cells were lysed by sonication at a 50% amplitude pulsation (1 s on and 1

s off) for a 1-min cycle and a 2-min rest between each cycle, for a total of 5 cycles. The lysate

was centrifuged at 26891.1 rcf at 4 °C for 45 min. The supernatant was loaded onto a nickel-

charged microporous polymethacrylate resin (MIDA, Purolite). The supernatant underwent batch

binding with the charged resin overnight in 4 °C with a slow tilt rotation.

After batch binding, the mixture was homogenized by inversion and applied to a gravity column. Flow through, wash, and elution fractions were collected using the lysis buffer, lysis buffer with imidazole (40 mM), and lysis buffer with a higher concentration of imidazole (250 mM), respectively. The fractions containing the desired protein was further purified using fast protein liquid chromatography (FPLC) using a Superdex^{TM} 75 10/300 GL column (GE Healthcare). The column was washed with 1 volume of 20% ethanol and 1 volume of double-distilled water and pre-equilibrated with 1 column volume of a size exclusion reference buffer (RB, 50 mM HEPES, 50 mM NaCl, 10% glycerol, 10 mM βME, pH 7.6) at a flow rate of 0.2 mL/min. The protein was eluted with the RB at 0.2 mL/min. A 12% polyacrylamide SDS-PAGE gel confirmed the homogeneity of the protein.

2.7.2 Bioconjugation of Fluorophores onto STC

At 37 °C for 1 h in the dark, the purified protein was incubated with BG-Alexa Fluor 488 and BC-Alexa Fluor 546 dyes (New England Biolabs) in a 1:2:2 molar ratio (protein:BG-dye:BC-dye) in DMSO with the addition of dithiothreitol (DTT, 1 mM). Unbound dye was removed by microfiltration of the solution with a 10 kDa molecular weight cut off (MWCO) microfilter (Amicon Ultra-0.5 Centrifugal Filter Unit) at 17136 rcf at 4 °C for 5 min.

2.7.3 Expression and Purification of Twitch-2B

Using BL21(DE3) (Thermo Scientific^{TM}) chemically competent *E. coli* cells, the miniprepped CFP-Twitch2B-YFP plasmids were heat shock transformed. The cells were plated on warm LB agar plates supplemented with carbenicillin (50 mg/mL) and placed in a 37 °C incubator to grow for 12-18 h. Seed cultures were made by picking single colonies from the transformation plates and inoculating into a culture tube with 5 mL LB and 5 µL of carbenicillin (50 mg/mL). The tubes were left to grow at 37 °C, shaking at 220 rpm, for 6 h. An expression culture was made by adding

the seed culture in 1 L of LB and 1 mL of carbenicillin (50 mg/mL). The expression culture was left to grow at 37 °C, shaking at 220 rpm, until the OD_{600} is at 0.6. Once it has reached this OD_{600}, the culture was induced with isopropyl-β-D-thio-galactoside (IPTG, 1 mM). The expression culture was moved to a pre-cooled 25 °C incubator for induction at 225 rpm for 12 to18 h.

The culture was removed from the incubator and centrifuged at 6084.1 rcf at 4 °C for 20 min to harvest the cells. The cells were resuspended in 20 mL of lysis buffer (25 mM MOPS buffer, 100 mM KCl, pH 7.6). A protease inhibitor cocktail (HALT) was added to the suspended cells at the manufacturer's recommended concentration. The suspended cells were lysed by sonication at a 50 % amplitude pulsation (1 second on and 1 second off) for a 1-min cycle and a 2-min rest between each cycle, with a total of 3 cycles. The lysate was centrifuged at 26891.1 rcf at 4 °C for 45 min. The supernatant was loaded onto a nickel charged immobilized metal affinity chromatography (IMAC) resin (1.5 mL of IMAC charged with $NiSO_4$ and equilibrated with the lysis buffer) The supernatant underwent batch binding to the charged IMAC resin overnight in 4 °C with constant shaking.

After batch binding, the IMAC/supernatant mixture was homogenized by inversion and loaded into a gravity column. The following fractions were collected: a flow through fraction (FT), a wash fraction using a solution of lysis buffer with 25 mM imidazole (W), and elution fractions using a solution of lysis buffer with 250 mM imidazole (E1-5). SDS-PAGE confirmed the expression of the protein and its purity. Ethylenediaminetetraacetic acid (EDTA, 0.5 M) was added to the eluted fractions containing the protein of interest and the mixture was dialyzed in 4 L of lysis buffer overnight and concentrated to approximately 1 mL

2.7.4 Tagging Insulin with N-Hydroxysuccinimide Ester (NHS)-Alexa Fluor 488

In order to label insulin with Alexa Fluor 488, Alexa Fluor 488-NHS ester (Thermo Fisher Scientific) and recombinant human insulin were combined at final concentrations of 20 µM and 84 µM, respectively, in a total volume of approximately 180 µL. The volume was split into 30 small reactions and incubated in a thermocycler for 1 h at 4 °C. The total volume of the reaction was serially dialyzed for 3 h and then overnight in 2 L of PBS pH 8.0, such that unbound, hydrolyzed NHS-Alexa Fluor 488 could be removed from the labelled insulin solution.

2.7.5 Fluorescence Imaging of SDS-PAGE Gels

Tagging of SNAP- and CLIP-tags with Alexa Fluor 488 and Alexa Fluor 546 was visualized by imaging the fluorescently tagged proteins on a 0.75 mm thickness SDS-PAGE using a Typhoon Trio+ Scanner (GE Healthcare) in "fluorescence acquisition" mode Fluorescent signals from Alexa Fluor 488 was imaged using the Green (532 nm) laser and the 526 SP filter at 500 PMT voltage, whereas for detecting Alexa Fluor 546, the Green (532 nm) laser and 580 BP filter at 400 PMT voltage was used. Images were recorded at 25-micron pixel size for high resolution scanning. Once fluorescent signals were imaged, the total protein was visualized using Coomassie dye.

2.7.6 Fluorescent Intensity Measurements by TECAN Spark Plate Reader

In a Corning black polystyrene 96 well plate, 100 µL of buffer (either TB or RB) was used to fill the wells unless otherwise stated. 4 µL of protein sensor solution was added to each well, and 405 nm and 450 nm excitation light were used excite the donor fluorophores on Twitch-2B and STC, respectively. Emission spectra from 450 to 600 nm and 500 to 600 nm were collected for Twitch-2B and STC. Excitation and emission bandwidths were set to 5 nm.

2.7.7 Determining Protein Concentration using the Bradford Assay

Protein concentration was determined with the Bradford protein assay. BSA standards and the protein samples were introduced to Coomassie Brilliant Blue G-250 dye (Bio-Rad) for protein

binding in 96 well Costar plate (SKU#3595), which undergoes a colorimetric change.

Absorbance is measured at 595 nm, and the protein concentration is determined through

interpolation of the standard curve.
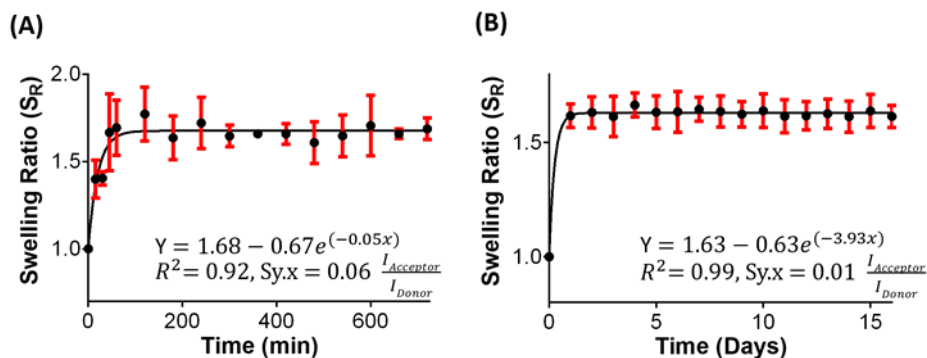
Figure S2.1. Swelling studies of PEGDMA 2000.
PEGDMA 2000 hydrogels were allowed to swell in PBS, pH 7.4 at room temperature to reach a steady state mass. To quantify the degree of swelling, the swelling ratio of the hydrogel was calculated. The formula is shown in **eq. s2.1**

$$S_R = \frac{W_s}{W_i} * 100 \qquad\qquad \textbf{eq s2.1}$$

where S_R is the hydrogel swelling ratio, W_s is the hydrogel swell mass after incubation in PBS, pH 7.4 at room temperature and W_i is the initial hydrogel mass right after polymerization.[1] The results indicate that (A) the hydrogel reaches a steady state mass after 5 h of incubation after which (B) there is no change in S_R for up to two weeks (relative standard deviation (RSD) = 0.87%).
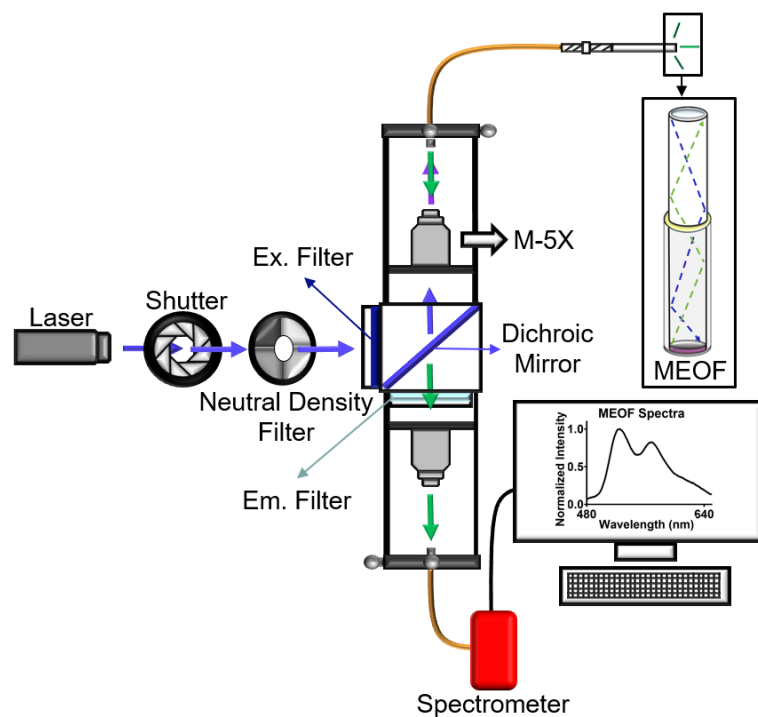
Figure S2.2. Spectroscopic Benchtop System. A benchtop optical system was constructed for MEOF excitation and emission collection. The system was integrated into a cage system to maintain fiber alignment. In the case of STC, excitation light is provided by a 450 nm continuous wave laser (4.5 mW, CPS450 ThorLabs) that is mechanically shuttered (CX2450B, NM Laser Product). The beam passes through a variable neutral density filter wheel (NDC-25C-4, Thorlabs) to reduce power in the beam. The beam then passes through a filter cube block (CM1-DCH with attached SM30 circular filter mounts tubes, Thorlabs), comprising a 450 nm bandpass filter (ET448/19x, Chroma) tuned to the laser wavelength, a dichroic beam splitting mirror with center wavelength at 458 nm (ZT458rdc, Chroma), and a 465 nm long pass filter (AT465lp, Chroma) in the emission pass to filter out any back-reflected laser light. Laser light reflected off the dichroic mirror is focused by a M-5x microscope objective lens (0.10 NA, Newport) into a SMA-SMA optical fiber patch cable (M92L01, Thorlabs). This optical fiber is attached to a SMA female plate mounted within a XY translation stage (ST1XY-S Translation Mount, Thorlabs) for fine X-Y alignment of the optical fiber relative to the focused laser beam. The MEOF is coupled to the distal end of the patch cable by a SMA to SMA mating sleeve (ADASMA, Thorlabs). Fluorescence emission is collected by the MEOF and collimated into our cage system, passing through the dichroic mirror and the 465 nm longpass filter, where it is coupled into an optical fiber. This coupling uses the same strategy as for the laser light into the MEOF system. The distal end of the optical fiber directs light into a spectrometer (CCS200, Thorlabs). ThorLabs software collects spectrometer data that is subsequently analyzed in MATLAB (MathWorks). In the case of the Twitch-2B construct, the laser, excitation, dichroic, and emission filters were replaced with a 405 nm continuous wave laser (Newport LQA305-40P laser, 45 mW maximum power), FBH405-10, DMLP425R, and FELH0450 filters (Thorlabs) respectively.

47
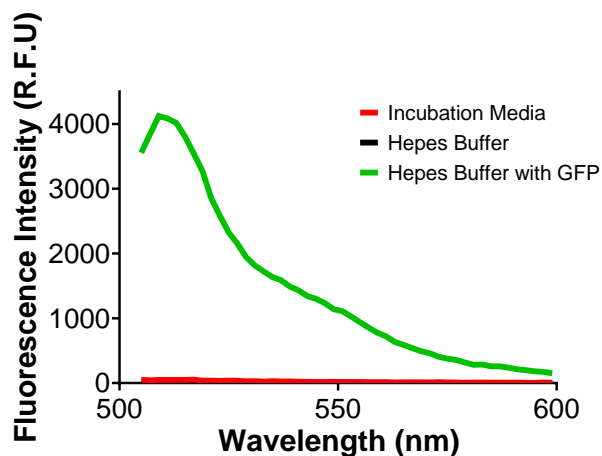
Figure S2.3. GFP encapsulation within the MEOF. GFP was loaded into the sensor-matrix of the MEOF probe and incubated in HEPES buffer for 5 h. 150 µL of the HEPES buffer was then analyzed with a fluorescence plate reader (red). For the experiment, negative and positive controls include 150 µL of HEPES buffer without GFP (black) and 150 µL of HEPES buffer spiked with 0.1 µL of GFP at 4 mg/mL (green). The spectral curves demonstrate GFP encapsulation within the MEOF.
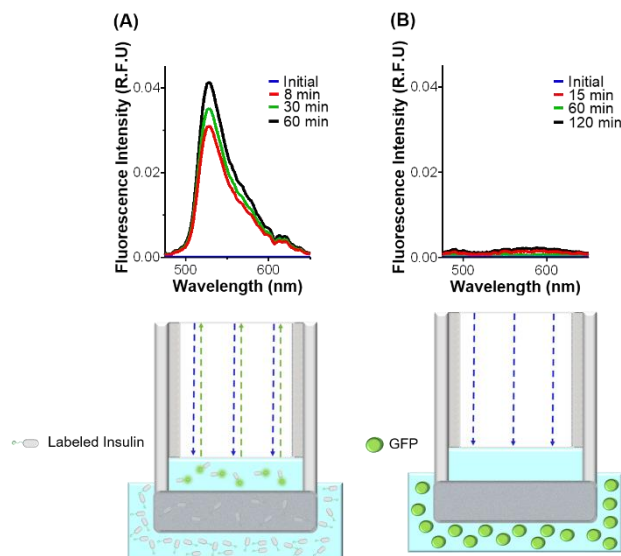
Figure S2.4. Selective permeability of the filter-membrane. The spectral curves demonstrate GFP encapsulation within the MEOF. Diffusion spectra (top) and schematic representation (bottom) of fluorescently labeled (A) insulin and (B) GFP demonstrate selective permeability by the MEOF.
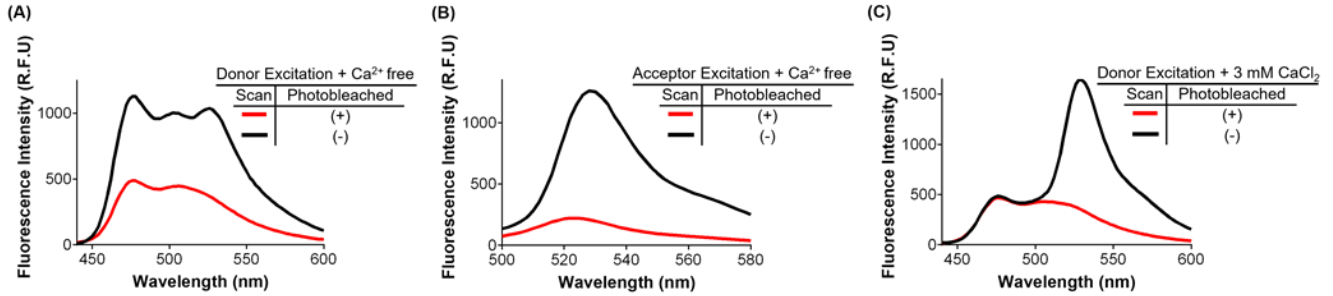
Figure S2.5. FRET properties of non-photobleached and photobleached Twitch2B samples. Both solutions contained 150 µL of Twitch2B protein (4 mg/mL). For the photobleached samples, both (A) donor excitation at 405 nm and (B) direct acceptor excitation at 475 nm have an absent acceptor fluorescence signal. (C) Moreover, donor excitation with the introduction of Ca^{2+} does not increase the FRET efficiency in the photobleached sample.

ATGCGGGGTTCTCATCATCATCATCATCATGGTATGGACAAAGACTGCGAAATGAAG
CGCACCACCCTGGATAGCCCTCTGGGCAAGCTGGAACTGTCTGGGTGCGAACAGGG
CCTGCACCGTATCATCTTCCTGGGCAAAGGAACATCTGCCGCCGACGCCGTGGAAGT
GCCTGCCCCAGCCGCCGTGCTGGGCGGACCAGAGCCACTGATGCAGGCCACCGCCT
GGCTCAACGCCTACTTTCACCAGCCTGAGGCCATCGAGGAGTTCCCTGTGCCAGCCC
TGCACCACCCAGTGTTCCAGCAGGAGAGCTTTACCCGCCAGGTGCTGTGGAAACTGC
TGAAAGTGGTGAAGTTCGGAGAGGTCATCAGCTACAGCCACCTGGCCGCCCTGGCC
GGCAATCCCGCCGCCACCGCCGCCGTGAAAACCGCCCTGAGCGGAAATCCCGTGCC
CATTCTGATCCCCTGCCACCGGGTGGTGCAGGGCGACCTGGACGTGGGGGGCTACG
AGGGCGGGCTCGCCGTGAAAGAGTGGCTGCTGGCCCACGAGGGCCACAGACTGGGC
AAGCCTGGGCTGGGTCGCATGCAAGTTGCCGACGCCAGCGAAGAGGAACTGAGCGA
GTGCTTCAGAATCTTCGACTTCGACGGCAACGGCTTCATCGACAGAGAGGAGTTTGG
CGACATCATCAGACTGACCGGCGAGCAGCTGACCGACGAGGACGTGGACGAGATCT
TCGGCGACTCCGACACCGACAAGAACGGCAGAATCGATTTCGACGAGTTCCTGAAG
ATGGTGGAAAACGTGCAGCCCATCTACCCCGAGCTCGACAAAGACTGCGAAATGAA
GCGCACCACCCTGGATAGCCCTCTGGGCAAGCTGGAACTGTCTGGGTGCGAACAGG
GCCTGCACCGTATCATCTTCCTGGGCAAAGGAACATCTGCCGCCGACGCCGTGGAA
GTGCCTGCCCCAGCCGCCGTGCTGGGCGGACCAGAGCCACTGATCCAGGCCACCGC
CTGGCTCAACGCCTACTTTCACCAGCCTGAGGCCATCGAGGAGTTCCCTGTGCCAGC
CCTGCACCACCCAGTGTTCCAGCAGGAGAGCTTTACCCGCCAGGTGCTGTGGAAACT
GCTGAAAGTGGTGAAGTTCGGAGAGGTCATCAGCGAGAGCCACCTGGCCGCCCTGG
TGGGCAATCCCGCCGCCACCGCCGCCGTGAACACCGCCCTGGACGGAAATCCCGTG
CCCATTCTGATCCCCTGCCACCGGGTGGTGCAGGGCGACAGCGACGTGGGGCCCTA
CCTGGGCGGGCTCGCCGTGAAAGAGTGGCTGCTGGCCCACGAGGGCCACAGACTGG
GCAAGCCTGGGCTGGGT

Legend: ■ HisTag ■ Snap Tag ■ Linkers ■ Twitch-2B ■ CLIP tag

Figure S2.6. Nucleotide sequence encoding the STC protein.
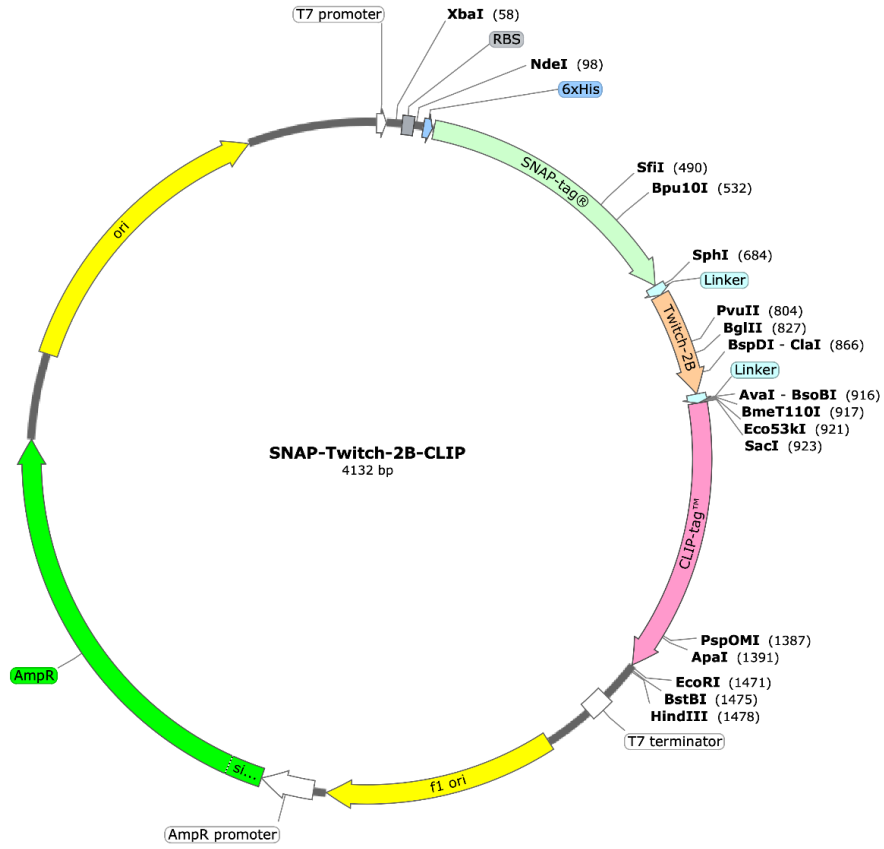
Figure S2.7. Plasmid Map of the gene encoding the STC protein in the pRSETB vector.
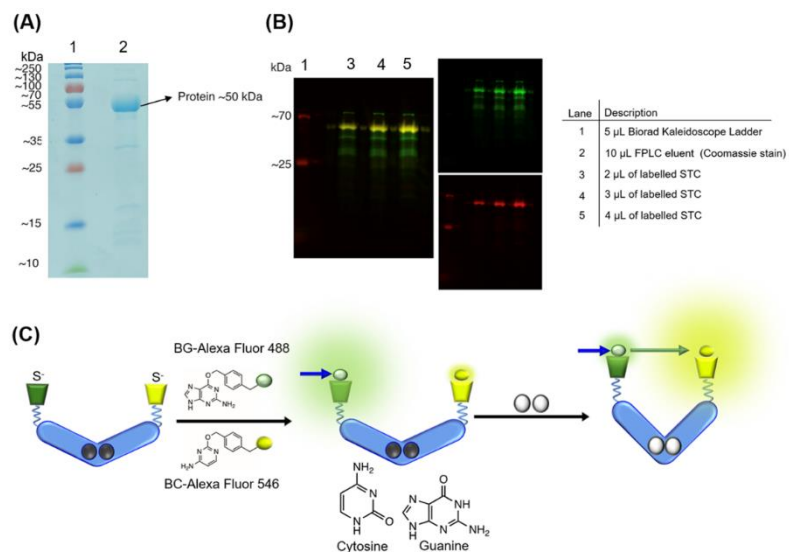
Figure S2.8. Production of STC. (A) SDS-PAGE was used to analyze the FPLC fractions to show the high protein yield and purity of STC. After STC protein was fluorescently labelled with Alexa Fluor 488 and 546 dyes using orthogonal SNAP and CLIP tags, which was confirmed with a (B) Typhoon fluorescence scanner.[2–4] The covalent linkage of the Alexa Fluor dyes onto SNAP and CLIP tag are shown in (C) where cytosine and guanine are displaced in the reaction.
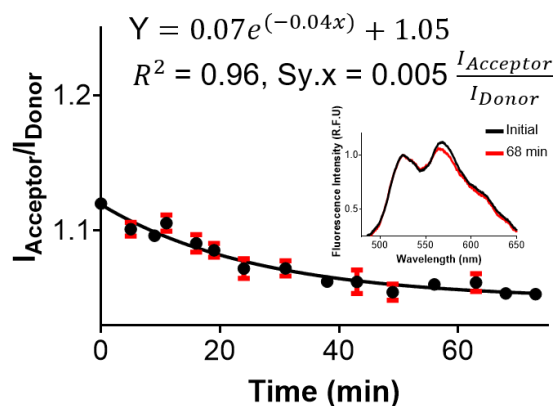
Figure S2.9. Unbinding of Ca^{2+}. The $I_{acceptor}/I_{donor}$ ratio falls after media exchange from RB with $CaCl_2$ (1.25 mM) solution to calcium-free RB. *Inset:* Emission spectra at times 0 and 68 min.

2.8 References

1. Seshadri DR, Li RT, Voos JE, et al. Wearable sensors for monitoring the physiological and biochemical profile of the athlete. *npj Digit Med*. 2019;2(1). doi:10.1038/s41746-019-0150-9

2.   Díaz J, Acosta F, Parrilla P, et al. Correlation among ionized calcium, citrate, and total calcium levels during hepatic transplantation. *Clin Biochem*. 1995;28(3):315-317. doi:10.1016/0009-9120(94)00094-C

3.   Chung HS, Cho SJ, Park CS. Effects of liver function on ionized hypocalcaemia following rapid blood transfusion. *J Int Med Res*. 2012;40(2):572-582. doi:10.1177/147323001204000219

4.   Chockalingam K, Zhao H. Directed evolution of specific receptor-ligand pairs for use in the creation of gene switches. In: *AIChE Annual Meeting, Conference Proceedings*. ; 2005:9272. doi:10.1073/pnas.0409206102

5.   Di Roberto RB, Chang B, Peisajovich SG. The directed evolution of ligand specificity in a GPCR and the unequal contributions of efficacy and affinity. *Sci Rep*. 2017;7(1). doi:10.1038/s41598-017-16332-2

6.   Maeshima K, Matsuda T, Shindo Y, et al. A Transient Rise in Free Mg2+ Ions Released from ATP-Mg Hydrolysis Contributes to Mitotic Chromosome Condensation. *Curr Biol*. 2018;28(3):444-451.e6. doi:10.1016/j.cub.2017.12.035

7.   Lindenburg L, Merkx M. Engineering genetically encoded FRET sensors. *Sensors (Switzerland)*. 2014;14(7):11691-11713. doi:10.3390/s140711691

8.   Thestrup T, Litzlbauer J, Bartholomäus I, et al. optimized ratiometric calcium sensors for functional in vivo imaging of neurons and t lymphocytes. *Artic Nat methods /*. 2014;11(2):175. doi:10.1038/nmeth.2773

9.   Asif MH, Fulati A, Nur O, et al. Functionalized zinc oxide nanorod with ionophore-membrane coating as an intracellular Ca2+ selective sensor. *Appl Phys Lett*. 2009;95(2). doi:10.1063/1.3176441

10.   Shortreed M, Kopelman R, Kuhn M, Hoyland B. Fluorescent Fiber-Optic Calcium Sensor for Physiological Measurements. *Anal Chem*. 1996;68(8):1414-1418. doi:10.1021/ac950944k

11.   Kastellorizios M, Tipnis N, Burgess DJ. Foreign body reaction to subcutaneous implants. *Adv Exp Med Biol*. 2015;865:93-108. doi:10.1007/978-3-319-18603-0_6

12.   Fu Z, R. Gilbert E, Liu D. Regulation of Insulin Synthesis and Secretion and Pancreatic Beta-Cell Dysfunction in Diabetes. *Curr Diabetes Rev*. 2012;9(1):25-53. doi:10.2174/15733998130104

13.   Hink MA, Griep RA, Borst JW, et al. Structural dynamics of green fluorescent protein alone and fused with a single chain Fv protein. *J Biol Chem*. 2000;275(23):17556-17560. doi:10.1074/jbc.M001348200

14.   Woting A, Blaut M. Small intestinal permeability and gut-transit time determined with low and high molecular weight fluorescein isothiocyanate-dextrans in C3H mice. *Nutrients*. 2018;10(6). doi:10.3390/nu10060685

15.   Algar WR, Hildebrandt N, Vogel SS, Medintz IL. FRET as a biomolecular research tool — understanding its potential while avoiding pitfalls. *Nat Methods*. 2019;16(9):815-829. doi:10.1038/s41592-019-0530-8

16.   Lipman NS, Jackson LR, Trudel LJ, Weis-Garcia F. Monoclonal Versus Polyclonal Antibodies: Distinguishing Characteristics, Applications, and Information Resources. *ILAR J*. 2005;46(3):258-268. doi:10.1093/ilar.46.3.258

17.   Dell'italia LJ, Collawn JF, Ferrario CM. Multifunctional role of chymase in acute and chronic tissue injury and remodeling. *Circ Res*. 2018;122(2):319-336. doi:10.1161/CIRCRESAHA.117.310978

18. Lin CC, Anseth KS. PEG hydrogels for the controlled release of biomolecules in regenerative medicine. *Pharm Res*. 2009;26(3):631-643. doi:10.1007/s11095-008-9801-2

19. Lanasa SM, Hoffecker IT, Bryant SJ. Presence of pores and hydrogel composition influence tensile properties of scaffolds fabricated from well-defined sphere templates. *J Biomed Mater Res - Part B Appl Biomater*. 2011;96 B(2):294-302. doi:10.1002/jbm.b.31765

20. Jang HJ, Shin CY, Kim KB. Safety evaluation of polyethylene glycol (PEG) compounds for cosmetic use. *Toxicol Res*. 2015;31(2):105-136. doi:10.5487/TR.2015.31.2.105

21. Renaghan AD, Rosner MH. Hypercalcemia: etiology and management. *Nephrol Dial Transplant*. 2018;33(4):549-551. doi:10.1093/ndt/gfy054

22. Anastasopoulos D, Kefaliakos A, Michalopoulos A. Is plasma calcium concentration implicated in the development of critical illness polyneuropathy and myopathy? *Crit Care*. 2011;15(5):R247. doi:10.1186/cc10505

23. Bajar BT, Wang ES, Zhang S, Lin MZ, Chu J. A guide to fluorescent protein FRET pairs. *Sensors (Switzerland)*. 2016;16(9). doi:10.3390/s16091488

24. Van Munster EB, Kremers GJ, Adjobo-Hermans MJW, Gadella TWJ. Fluorescence resonance energy transfer (FRET) measurement by gradual acceptor photobleaching. *J Microsc*. 2005;218(3):253-262. doi:10.1111/j.1365-2818.2005.01483.x

25. Derieppe M, Bos C, De Greef M, Moonen C, Denis De Senneville B. Correction for photobleaching in dynamic fluorescence microscopy: Application in the assessment of pharmacokinetic parameters in ultrasound-mediated drug delivery. *Phys Med Biol*. 2015;61(2):588-600. doi:10.1088/0031-9155/61/2/588

26. Panchuk-Voloshina N, Haugland RP, Bishop-Stewart J, et al. Alexa dyes, a series of new fluorescent dyes that yield exceptionally bright, photostable conjugates. *J Histochem Cytochem*. 1999;47(9):1179-1188. doi:10.1177/002215549904700910

27. Regoes A, Hehl AB. SNAP-tag^{TM} mediated live cell labeling as an alternative to GFP in anaerobic organisms. *Biotechniques*. 2005;39(6):809-812. doi:10.2144/000112054

28. Gautier A, Juillerat A, Heinis C, et al. An Engineered Protein Tag for Multiprotein Labeling in Living Cells. *Chem Biol*. 2008;15(2):128-136. doi:10.1016/j.chembiol.2008.01.007

29. Zaharieva DP, Turksoy K, McGaugh SM, et al. Lag Time Remains with Newer Real-Time Continuous Glucose Monitoring Technology During Aerobic Exercise in Adults Living with Type 1 Diabetes. *Diabetes Technol Ther*. 2019;21(6):313-321. doi:10.1089/dia.2018.0364

30. Kurganov BI, Lobanov A V., Borisov IA, Reshetilov AN. Criterion for Hill equation validity for description of biosensor calibration curves. *Anal Chim Acta*. 2001;427(1):11-19. doi:10.1016/S0003-2670(00)01167-3

31. Bagur R, Hajnóczky G. Intracellular Ca2+ Sensing: Its Role in Calcium Homeostasis and Signaling. *Mol Cell*. 2017;66(6):780-788. doi:10.1016/j.molcel.2017.05.028

32. Mótyán J, Tóth F, Tőzsér J. Research Applications of Proteolytic Enzymes in Molecular Biology. *Biomolecules*. 2013;3(4):923-942. doi:10.3390/biom3040923

33. Sanford L, Palmer A. Recent Advances in Development of Genetically Encoded Fluorescent Sensors. In: *Methods in Enzymology*. Vol 589. Academic Press Inc.; 2017:1-49. doi:10.1016/bs.mie.2017.01.019

34. Vinkenborg JL, Nicolson TJ, Bellomo EA, Koay MS, Rutter GA, Merkx M. Genetically encoded FRET sensors to monitor intracellular Zn2+ homeostasis. *Nat Methods*.

2009;6(10):737-740. doi:10.1038/nmeth.1368

35.   Leach SPZ and JB. Hydrolytically degradable poly(ethylene glycol) hydrogel Biomacromolecules. *Biomacromolecules*. 2011;11(5):1348-1357. doi:10.1021/bm100137q.Hydrolytically

36.   Keppler A, Gendreizig S, Gronemeyer T, Pick H, Vogel H, Johnsson K. A general method for the covalent labeling of fusion proteins with small molecules in vivo. *Nat Biotechnol*. 2003;21(1):86-89. doi:10.1038/nbt765

37.   Keppler A, Kindermann M, Gendreizig S, Pick H, Vogel H, Johnsson K. Labeling of fusion proteins of O6-alkylguanine-DNA alkyltransferase with small molecules in vivo and in vitro. *Methods*. 2004;32(4):437-444. doi:10.1016/j.ymeth.2003.10.007

38.   Keppler A, Pick H, Arrivoli C, Vogel H, Johnsson K. Labeling of fusion proteins with synthetic fluorophores in live cells. *Proc Natl Acad Sci U S A*. 2004;101(27):9955-9959. doi:10.1073/pnas.0401923101

CHAPTER 3: IN VIVO PHOTONIC DETECTION OF PH AND LACTATE ON AN IMPLANTABLE FLEXIBLE SENSOR

Dat Nguyen[1,3], Micah M. Lawrence[1,2,3], Haley Berg[3], Samir Shreim[2], Mark T. Keating[2], John Weidling[2], Elliot L. Botvinick[1,2,3,4,*]

[1]Department of Biomedical Engineering, University of California, Irvine, CA 92697-2730 USA.

[2]Beckman Laser Institute and Medical Clinic, University of California Irvine, Irvine, California 92612, USA

[3]The Edwards Lifesciences Center for Advanced Cardiovascular Technology, University of California Irvine, Irvine, California 92697, USA

[4]Department of Surgery, University of California, Irvine, CA 92697-2730, USA.

*Corresponding Author

KEYWORDS: pH sensor, lactate sensor, multi-analyte, photonic, continuous monitoring, critical care monitoring

3.1 Abstract

Clinical research shows that frequent measurements of both pH and lactate can help guide therapy and improve patient outcome. However, current methods of sampling blood pH and lactate make it impractical to take readings frequently (due to the heightened risk of blood infection and anemia). As a solution, we have engineered an implantable pH and lactate sensor (PALS), that can provide continuous, physiologically relevant measurements. To measure pH, a sheet containing a pH-sensitive fluorescent dye is placed over 400 and 465 nm light emitting diodes (LEDs) and a filter-coated photodetector. The filter-coated photodetector collects an emitted signal from the dye for each LED excitation, and the ratio of the emitted signals is used to monitor pH. To measure lactate, two sensing sheets comprising an oxygen-sensitive phosphorescent dye are each mounted to a 625 nm LED. One sheet additionally comprises the enzyme lactate oxidase. The LEDs are sequentially modulated to excite the sensing sheets, and the difference in their phase shift at the LED drive frequency is used to monitor lactate. In vitro results indicate that PALS successfully records pH changes from 6.92 to 7.70, allowing for discrimination between acidosis and alkalosis, and can track lactate levels up to 9 mM. Both sensing strategies exhibit fast rise times (< 5 min) and stable measurements. Multi-analyte in vitro models of physiological disorders show that the sensor measurements consistently quantify the expected pathophysiological trends without crosstalk; in vivo rabbit testing further indicates usefulness in the clinical setting.

3.2 Introduction

pH and lactate are biomarkers that can be monitored during sepsis, as well as liver and lung disease to improve patient outcome.[1–4] Blood pH is naturally buffered to within a range of 7.35 to 7.45 and deviations from this range can be indicative of serious disease.[5,6] Examples of these

56

deviations are in cases of metabolic acidosis and alkalosis where blood pH can change when the body has too high or low concentration of hydrogen ions (H^+) and/or bicarbonate. [5,6] A form of metabolic acidosis is lactic acidosis, which can occur when lactate is generated in excess (hyperlactatemia, > 2 mM) and the amount of circulating H^+ exceeds the capacity of the blood's buffering system.[7,8] Elevated lactate levels are often a sign of cellular hypoxia as lactate is excessively produced during anaerobic glycolysis.[9] An increase in lactate can result in a decrease in pH; however, this is not always the case. For this reason, it is important to recognize that measuring only lactate or pH is not a surrogate for measuring the other. For example, in respiratory acidosis, pH may be directly influenced by an accumulation of carbon dioxide in the blood while lactate remains unchanged.[10] In this case, frequent pH measurements can guide therapy. Importantly, there are a variety of circumstances when both pH and lactate should be measured simultaneously. Frequently referenced examples are during sepsis or septic shock as Lee et al. found that both the lactate levels and pH are essential when predicting patient mortality.[1]

Current clinical standards for measuring blood pH and lactate require intermittent blood draws and analysis by benchtop instruments (Yellow Springs Instrument, YSI) or hand-held monitors (Abbott Laboratories i-STAT).[11–13] The frequency of measurements are limited ultimately by the frequency of blood draws which increase the likelihood of blood infections and anemia.[11,14] Meanwhile, there is substantial evidence suggesting that attentive monitoring and treatment of pH and lactate can improve patient prognosis and outcome.[15,16] In a multisite study with 348 patients having initial lactate $\geq$ 3.0 mEq/L, goal-oriented treatment targeting a 10% decrease in lactate per hour increased patient survivability by 10% as compared to the control (standard treatment, p = 0.067).[17] Importantly, in addition to reduced mortality, patients were discharged from the intensive care unit

earlier than those in the control group. Moreover, in a prospective study with 75 patients experiencing sepsis and metabolic acidosis, both pH and lactate endpoint values were concluded as vital biomarkers towards patient outcome.[18] In this study, the 11 non-survivors had a lower mean pH and a higher mean lactate level than survivors after 5 days in the Intensive Care Unit. Changes in pH and lactate were not statistically significant ($p > 0.714$) as compared to initial values for the nonsurvivors, whereas significant changes were observed for the 64 survivors ($P < 0.002$).[18] Monitoring pH and lactate clearly has major implications towards patient prognosis, underscoring the value of a continuous pH and lactate sensor.

There are well established pH sensing modalities including electrochemical-based electrodes and luminescent dyes. Electrochemical-based glass and metal oxide electrodes measure pH through a difference in H^+ concentration between a sensitive and reference electrode.[19,20]Although glass electrodes provide the highest level of specificity, they cannot be easily miniaturized and require frequent calibration.[19] Metal oxide electrodes can be easily miniaturized, but exhibit low resolution, large drift, and hysteresis.[19,21] Meanwhile, pH-sensitive luminescent probes vary in their linear range of sensitivity (pKa), quantum yield, and mode of operation (intensity, emission ratio, etc.).[22–24] To continuously monitor pH on an implantable sensor, we have selected luminescent dye 8-hydroxypyrene-1,3,6-trisulfonic acid trisodium salt (HPTS). HPTS has a reported pKa of 7.3, exhibits minimal toxicity, a quantum yield of 0.82 in water, and a linear response ranging from 6.7 to 8.7, which spans the pathophysiological range of acidosis and alkalosis.[25,26] HPTS peak emission intensity at 520 nm is a function of its spectral absorption efficiency. HPTS absorbs light more efficiently at 450 nm at high pH as compared to low pH. Conversely, HTPS absorbs 405 nm light more efficiently at lower pH values.[27] It has been shown

that with serial light excitation at 450 and 405 nm, HPTS can reliably measure pH through a ratiometric analysis at its peak emission wavelength.[27]

Numerous strategies exist to measure lactate, including colorimetric assays, high-performance liquid chromatography, and enzyme-linked immunosorbent assays.[28–30] One common mode of enzyme-based lactate sensing (as used in the YSI 2300 STAT Plus Glucose and Lactate Analyzer) employs lactate oxidase (LOX).[31] The LOX reaction consumes both oxygen and lactate while producing hydrogen peroxide and pyruvate. This allows lactate to be indirectly measured through monitoring the consumption of oxygen or generation of hydrogen peroxide.[28,29] The generation of hydrogen peroxide is commonly used for electrochemical-based LOX sensing of lactate.[32–34] Common challenges in such electrochemical sensing include high operation voltages, dependencies on electron-transfer mediators (which can be toxic and exhibit poor solubility), and acetaminophen interference.[32,35,36] As an alternative to electrochemical sensing, our group and others have published the use of a phosphorescent oxygen-sensitive dye for continuous measurements of lactate.[37,38] In our clinical studies, oxygen was detected by the metalloporphyrin dye platinum (II) meso-tetraphenyl tetrabenzoporphine (PtTPTBP).[38] PtTPTBP phosphorescence is quenched by oxygen, reducing its luminescence lifetime. This lifetime can be assessed by determining the phase shift between excitation and emission waveforms.[39] An indirect measurement of lactate may therefore be reported by calculating the phase shift of PtTPTBP

emission in the presence of LOX, lactate, and oxygen. This sensing scheme is adapted here to continuously monitor lactate within a multi-analyte sensor.
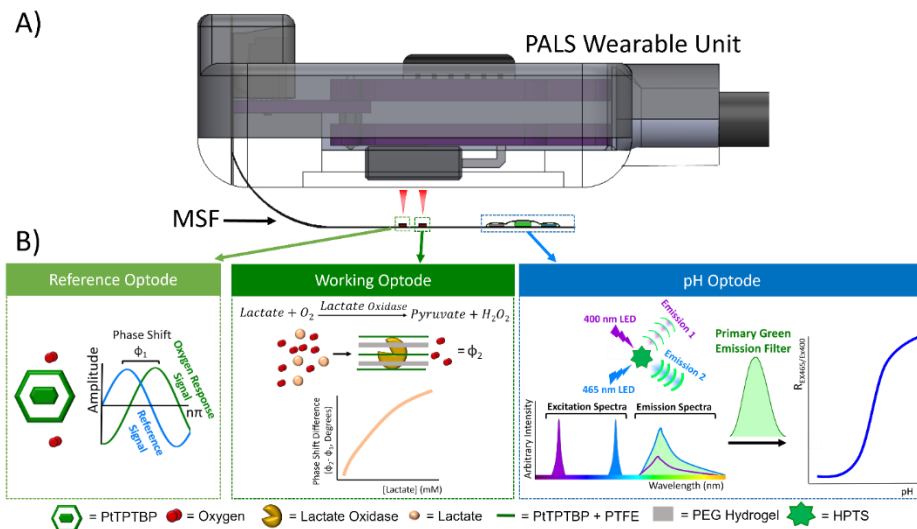
Figure 3.1. Schematic overview of pH and Lactate Sensor (PALS). A) PALS includes a wearable unit and a transcutaneous Multi-analyte Sensing Flex Sensor (MSF) to detect pH and lactate. B, (*left*) Oxygen is monitored by analyzing the PtTPTBP light emission's phase shift. (*middle*) Lactate oxidase consumes both oxygen and lactate; oxygen consumption can be used as an indirect measurement of lactate. (*right*) pH is measured by ratiometric analysis of HPTS light emission.

Herein, we introduce an implantable, continuous multi-analyte sensor, referred to as the pH and Lactate Sensor (PALS) (**Figure 3.1A**). PALS employs two unique sensing modalities at the tip of the implantable Multi-analyte Sensing Flex Sensor (MSF) to monitor pH and lactate: (1) a dual excitation, single band detection scheme that collects pH-sensitive light emissions and (2) a luminescence lifetime detection scheme that captures oxygen and lactate-sensitive light emissions (**Figure 3.1B).** *In vitro* results show rapid rise times for both pH and lactate sensing, measurement reversibility, and sensitivity across their respective pathophysiological ranges. Further, when measuring both analytes simultaneously, measurements were shown to be free of crosstalk. An implant study in a rabbit model of hypoxemia provides further evidence that PALS signals are reversible and trend appropriately with reference to a handheld blood gas analyzer.

60

3.3 Methods

3.3.1 Filter-Coated Photodetector

For the pH sensor, silicon photodiodes were coated with an optical filter as follows. A plastic green bandpass filter (Primary Green Filter, Lee filters, USA) was first cut into a 2 cm x 2 cm square. The square filter was then placed onto the surface of a 2 mm x 1.25 mm silicon photodiode (SFH2716, OSRAM Opto Semiconductors, Germany) that had been mounted on a microscope glass slide. The edges of the filter were held in place by two additional glass slides. A Varitemp VT-750C heat gun (Master Appliance, USA) at a temperature setting of 250°C was then used to melt the plastic green bandpass filter onto the photodiode (**Figure S3.1**).

3.3.2 pH Sensor Sheet (HSS)

First, a 12.7 mM HPTS stock solution was formulated by dissolving 99 mg of HPTS (MilliporeSigma, USA) in 15 mL of Milli-Q water (MilliporeSigma, 18.2 Mohm·cm at 25°C). 10 g of 45-150 µm diameter Dowex® 1X8 resin beads (MilliporeSigma, USA) were then suspended in the stock solution within a 20 mL disposable scintillation vial. This process yields the resin bead suspension (**Figure 3.2A**) and allows the negatively charged sulfonate groups on HPTS to ionically bind to the positively charged Dowex Resin.[25] 500 µL of the resin bead suspension was then added to a 1.5 mL amber glass vial along with 50 mg of poly(ethylene glycol) dimethacrylate 8000 (PEGDMA8000, Polysciences, USA), and 12 mg of 2-Hydroxy-1-(4-(2-hydroxyethoxy)phenyl)-2-methylpropan-1-one (Irgacure 2959, Sigma-Aldrich, USA), creating the pH-sensor suspension (**Figure 3.2B**).

To fabricate the pH Sensor Sheet (HSS), a thin circular sheet of hydrophilic polytetrafluoroethylene (PTFE, H050A047A, 35 μm thick, 0.50 μm pores, 47 mm diameter, Sterlitech, USA) was cut into a 1.2 cm x 1 cm rectangle and placed onto a microscope glass slide. 40 μL of the pH-sensor suspension was then pipetted onto the cut PTFE sheet. The sheet was then sandwiched between two glass slides (**Figure 3.2C**) until the pH-sensor suspension uniformly coated one side of the sheet. The pores of the PTFE sheet are two orders of magnitude smaller than the resin bead diameter, preventing resin penetration into the sheet. The coated sheet was then polymerized for 15 min using 365 nm wavelength light emitted from an 8-watt dual-ultraviolet (UV) transilluminator (VWR, USA) to produce the HSS. The HSS was retrieved with tweezers and left to swell for at least 2 h in Milli-Q water within a 20 mL scintillation vial (**Figure 3.2D**).
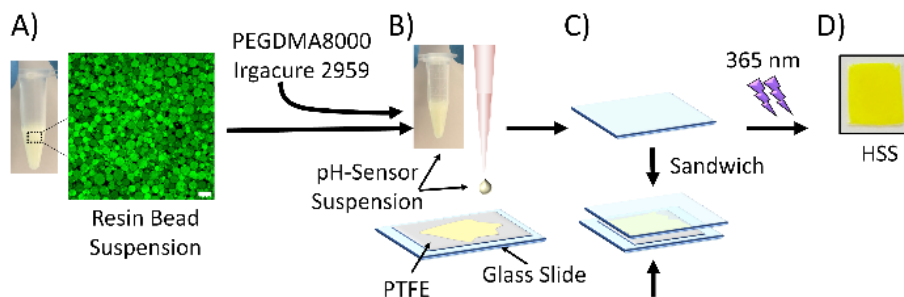
Figure 3.2. pH Sensor Sheet (HSS) Fabrication. A) Fluorescence confocal micrograph (Olympus Fluoview 1200) of the pH-sensitive resin bead suspension (405 nm laser excitation, emission bandpass filter: 505-540 nm). Scale bar = 100 μm. B) The suspension is pipetted onto a PTFE sheet. C) The suspension is sandwiched between two glass slides. D) The suspension is polymerized, yielding the HSS. The HSS is hydrated to allow for hydrogel swelling.

3.3.3 LOX and Oxygen Sensor Sheets

LOX Sheets were fabricated from oxygen-sensitive dye-coated PTFE sheets, the Protein Mixture containing enzymes LOX and catalase, and the Pretreatment Solution, all of which are detailed in supporting information. First, a 1 cm x 1 cm square of the dye-coated PTFE sheet was excised using a razor blade. 4.5 μL of Pretreatment Solution was then pipetted onto each of two

microscope glass slides (**Figure 3.3A**). After, the dye-coated PTFE sheet was sandwiched

between the two glass slides to force the Pretreatment Solution into the pores of the sheet. The

purpose of the Pretreatment Solution is to establish a porous network within the dye-coated

PTFE sheet that limits the diffusion of lactate and oxygen. Next, two parallel doubled-layered

strips of 25 µm-thick Kapton tape (Tapes Master, USA) were applied to a glass slide to function

as spacers. 4.5 µL of Protein Mixture was then pipetted in between the spacers and onto a second

slide. The pre-treated dye-coated PTFE sheet was then placed between the spacers and

sandwiched between the glass slides. While sandwiched, the sensor sheet was polymerized with

the 8-watt dual-UV transilluminator for 5 min to yield the LOX Sheet (**Figure 3.3B**). The

Oxygen Sheet was fabricated in similar fashion except for the exclusion of LOX and catalase in

its Protein Mixture.
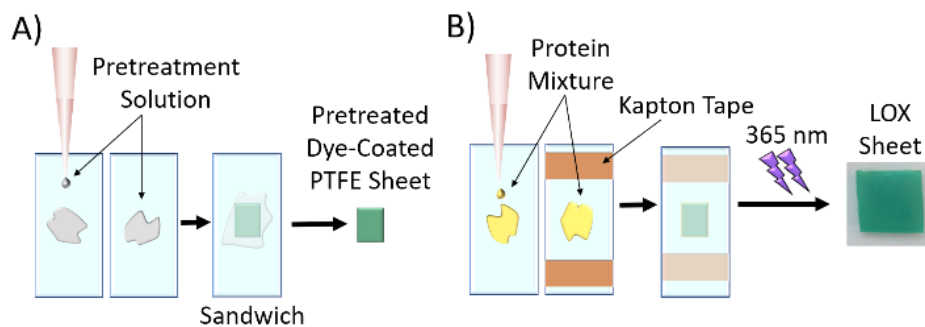
Figure 3.3. LOX Sheet Fabrication. A) Pretreatment Solution wets the dye-coated PTFE sheet.
B) The pretreated dye-coated PTFE sheet is sandwiched between glass slides containing the
Protein Mixture. Strips of Kapton Tape serve as spacers to control for membrane thickness. UV
polymerization cures the LOX Sheet.
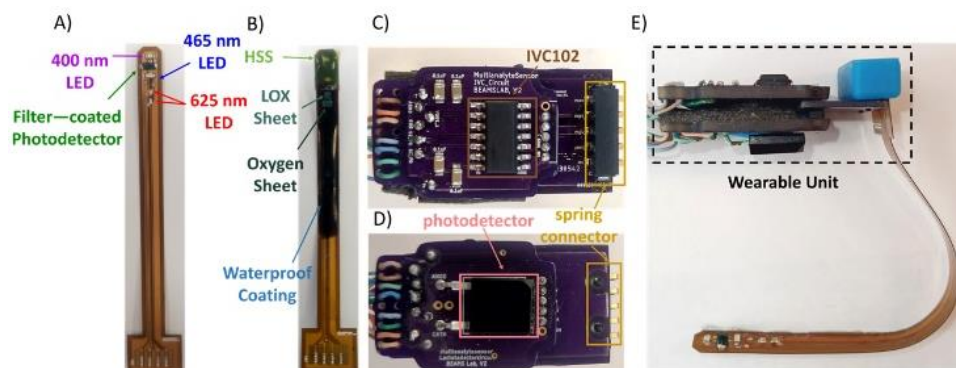
Figure 3.4. PALS Sensing Components**.** A) An MSF containing five on-strip optoelectronic components required for sensing. B) Fully assembled MSF comprising sensing sheets and waterproof coating. C) Integrator board for amplifying pH signals. D) Photodetector board for lactate and oxygen sensing. E) PALS Wearable Unit connected to the MSF.

3.3.4 PALS Circuitry

PALS consists of custom-made printed circuit boards (fabricated by OSH Park, USA) designed

using Eagle (Autodesk, USA). Essential components of the circuits are shown in **Figure S3.2**.

These custom boards were manually assembled and make up the three main subunits of PALS.

The first subunit is the MSF (**Figure 3.4A**). The second subunit is the wearable unit comprising

three circuit boards: (1) the integrator board for pH sensing based on the IVC102 transimpedance

amplifier (Texas Instruments, USA, **Figure 3.4C**), (2) the photodetector board for lactate and

oxygen sensing (**Figure 3.4D**), and (3) the connector board to connect the photodetector and

integrator boards to the MSF (**Figure 3.4E**). The last subunit is the backend controller unit (shown

in **Figure S3.2**) comprising a microcontroller Teensy 3.2 (PJRC, USA) and two circuit boards: (1)

the controller board for charlieplexing and tuning the drive current of the MSF LEDs (**Figure**

S3.2A) and (2) the IVC power supply board. Custom software was written for Teensy 3.2 to

charlieplex the LEDs and acquire data, using a combination of Arduino (Arduino, USA) with

Teensyduino library (PJRC, USA) and LabView (National Instruments, USA).

Custom designed housings were printed by a stereolithography printer (Prusa SL1, Prusa Research, Czech Republic) to protect and house the wearable unit as illustrated in **Figure 3.1**. The housing unit serves to also pressure-connect the prongs of the 5-spring battery connector (009155005852006, AVX Corporation, USA) on the connector board to the gold pads of the MSF, as depicted in **Figure 3.4E**.

3.3.5 Multi-sense Flexible Sensor (MSF) Fabrication

The MSF contains optoelectronic components for both pH and lactate sensing (**Figure 3.4A**). The optoelectronic components for pH sensing are a 400 nm LED (SM0603UV-400, Bivar, USA), a 465 nm LED (APT1608QBC/G, Kingbright, USA) and a filter-coated photodetector. Two 625 nm LEDs (APHHS1005LSECK/J3-PF, Kingbright, USA) are used for lactate and oxygen sensing. Each LED spectrum is shown in **Figure S3.3.** The MSF was coated with Loctite EA E-60NC (1:1 resin to hardener mix ratio, Henkel, Germany) for waterproofing. The waterproof coating was left to cure overnight. The sensing sheets were applied as described in the supporting material (**Figure 3.4B**).

3.3.6 Measurement Parameters

For pH sensing, LED currents were set to 6 mA and HSS-emitted light was sampled at 10Khz. Detection integration times (< 1s) were tuned at the start of each experiment. The tuning occurs in the first test solution of each *in vitro* experiment or following insertion for the *in vivo* experiment. Specifically, integration time was tuned such that the IVC hold voltage ranged between 1-2 V, corresponding to 30 - 61% of the total integration capacitance.

For lactate sensing, each of the 625 nm LEDs were illuminated one at a time. The LEDs were driven by a waveform comprising 21 cycles of a square wave with peak current of 9 mA, at a

frequency of 5 kHz, and 25% duty cycle. PtTPTBP emission was sampled simultaneously at 500kHz.

3.3.7 Statistical Analysis

Measurements are reported as the mean and standard error of the mean. Statistical analysis included a one-way analysis of variance (ANOVA) with Tukey post-hoc comparison or coefficient of variance (CV). $p < 0.05$ denotes statistical difference. Prism 8 (GraphPad, USA) was used for statistical analysis.

3.3.8 In Vivo Rabbit Study

The PALS implant study was conducted with the approval of the Institutional Animal Care and Use Committee at the University of California Irvine. A New Zealand White Rabbit was sedated with a 2:1 ratio of Ketamine Hydrochloride (100mg/ml, Ketaject, Phoenix Pharmaceutical Inc., USA): Xylazine (20mg/ml, Anased, Lloyd Laboratories) at a dose of 37.5mg/kg of Ketamine and 5 mg/kg of Xylazine IM using a 25-gauge 5/8-inch needle. The mixture of ketamine and xylazine was infused via the animal's right marginal ear vein. The animal was intubated and placed on mechanical ventilation with a tidal volume of 50 mL per breath, respiratory rate of 20 breaths/min, and 100% oxygen. An arterial catheter was placed within the right femoral artery for systemic blood pressure measurements and arterial blood gas sampling.

To implant the MSF in the subcutaneous space of the inner left thigh of the rabbit, first, an incision (length = 0.8 cm) was created with a scalpel. Next, a Metzenbaum dissecting scissor (Cole-Parmer, USA) was inserted inside the incision to separate skin from underlying muscle, to accommodate the tip of the MSF. After MSF-tip insertion, Loctite 4981 adhesive (Henkel, Germany) was applied at the incision site to adhere the MSF onto the skin and seal the incision. The PALS Wearable Unit was then placed on the skin and aligned to the MSF tip. Hypafix adhesive (USA) was placed over

the PALS Wearable Unit to limit sensor movement. After baseline measurements, the PALS was disconnected, and the animal was placed inside a sealed chamber which was then moved into a fume hood. The animal received 800 ppm chlorine gas (Airgas, USA) for 6 min followed by a 5 min rest period. 1 mL of 100 mM trihistidyl cobinamide was then administered through the right marginal ear vein. The animal was returned to the surgical room and the PALS was reconnected to resume monitoring. At the conclusion of the study, the animal was euthanized per standard procedures (1 mL of Euthasol, Virbac, USA).

3.3.9 Analysis of In Vivo Data

During the study, blood was drawn from the right femoral artery at 8 time points. Four blood draws were retrieved before and after chlorine gas and cobinamide infusion. Blood pH and lactate concentration was immediately assessed with an i-STAT (Abbott Laboratories, USA) using Abbott CG4+cartridges (Abbott Laboratories, USA). PALS pH and lactate measurements were retrospectively calibrated to the blood pH and lactate concentrations obtained from the i-STAT with a linear regression model.

3.4 Results and Discussion

3.4.1 pH Sensing by Dual LED Excitation and Single Band Detection

The PALS uses a dual LED excitation, single band photodetection scheme for measuring pH. To enable such sensing, the tip of the MSF comprises two surface-mount LEDs to excite an HSS and a coated photodetector to collect pH-sensitive emissions. To first determine if this is a viable scheme, a benchtop optical system was constructed (**Figure 3.5A**; fabrication methods in supplemental section). This system includes surface mount 400 nm and 465 nm dominant-wavelength LEDs soldered onto a protoboard, and a microscope objective lens that couples emitted light to a spectrometer (**Figure 3.5A).** pH-sensitive spectra from an HSS in a pH 7.6 solution were

collected with serial illumination from the two LEDs (**Figure 3.5B).** HSS emission spectrum

ranges from 470 nm to 660 nm and has a peak value at 520 nm. While the 400 nm LED light does

not overlap the HSS emission spectrum, the 465 nm LED does, necessitating an optical filter that

mitigates the effects of this spectral crosstalk. Ideally, such a filter should transmit the HSS

emission spectrum (**Figure 3.5B**) and be easily applied onto the surface of a photodiode. The

Primary Green Filter was selected which can be applied onto a photodiode as described in methods.

To simulate the filtering behavior of Primary Green Filter, its transmission spectra was multiplied

with HSS spectra (one per LED). The resulting filtered-spectra show that the 465 nm LED light

has a negligible contribution to the fluorescence signal (**Figure 3.5C**). To test for pH sensitivity

and reversibility, HSS spectra in solutions having pH 7.2 or 7.6 were collected and then multiplied

by the Primary Green Filter transmission curve. The ratio of area-under-the-curve (AUC Ratio:

Ex465/Ex400) was determined at these two pH values. Results indicate that the dual LED, single-

band detection scheme is stable and reversible and can be utilized as a pH optode at the tip of the

MSF (**Figure 3.5D**).
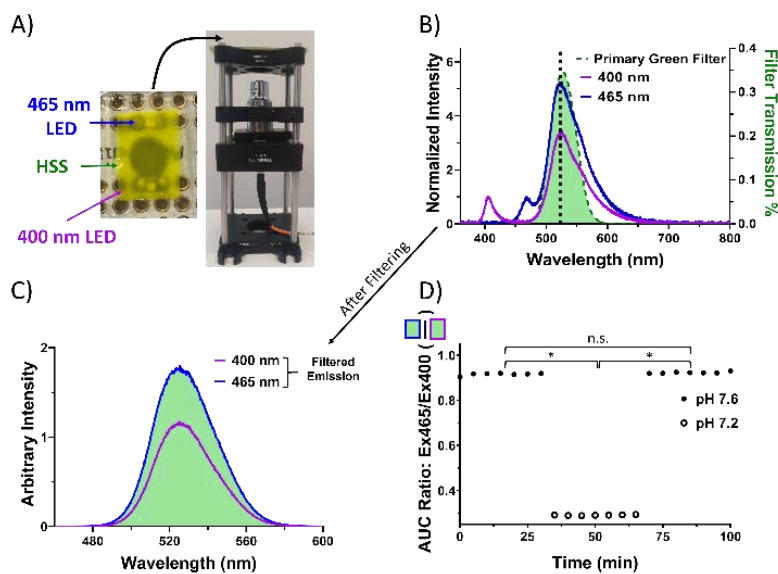
Figure 3.5. Dual LED Excitation of the HSS**.** A, *(left)* 465 nm and 400 nm LEDs soldered onto a
protoboard and covered by an HSS; *(right)* HSS emission signals are collected by a benchtop

optical system for analysis. An optical fiber routes the collected signals to a spectrometer. B) Dual emission spectra at pH 7.6. Green spectrum shows the transmission curve of the Primary Green Filter. Black dotted line matches HPTS peak emission wavelength. C) HPTS emission spectra following multiplication with the Primary Green Filter transmission spectrum. D) Filtered AUC ratios for solutions of pH 7.2 and 7.6. Mean ratios were analyzed for statistical significance. *p<0.05.

3.4.2 pH Optode

The pH optode comprises three of the optoelectronic elements at the tip of the MSF (**Figure 3.4A**).

The optode is fabricated by placing an HSS at the tip of the MSF such that it overlaps the two

LEDs and filter-coated photodetector (**Figure 3.4B**) as described in supplemental materials.

Photocurrents from the photodetector are amplified and converted to a voltage using a

transimpedance amplifier. pH is related to the ratio of the voltages acquired with 465 nm and 400

nm LED illumination ($R_{Ex465/Ex400}$) after background subtraction (no LED on).

3.4.3 Lactate Optode

The lactate optode was adapted from our previous work. In brief, two oxygen-sensitive PtTPTBP

dye sheets are mounted on two 625 nm dominant-wavelength LEDs. One of these sheets also

contains the enzyme LOX. The working optode has the enzyme-containing sheet, whereas the

reference optode has the enzyme-free sheet. The LEDs are illuminated in sequence, and the

oxygen-sensitive emitted light are detected by a photodetector within the PALS Wearable Unit

(**Figures 3.1 and 3.4E**).[40] Lactate is related to the phase shift difference between the working and

reference optode signals. The phase shift is defined as the phase difference (assessed by Fourier

Transform) between the LED drive-current waveform and corresponding photodiode signal at the

drive frequency.
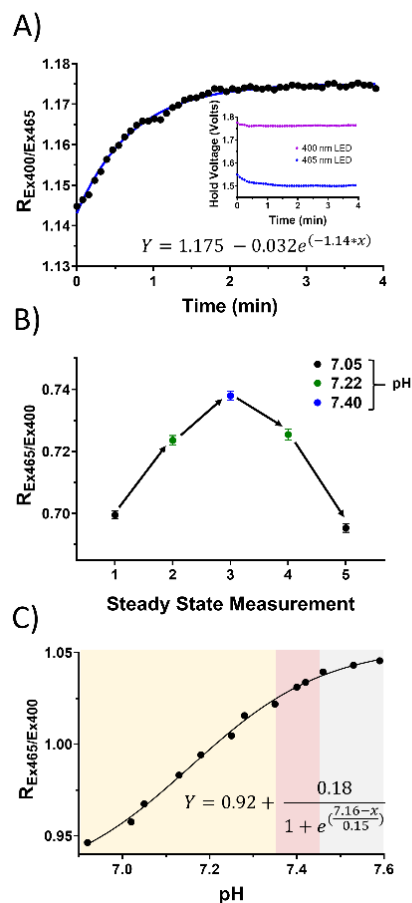
Figure 3.6. Ratiometric pH Sensing. A) pH sensor rise time from pH 7.45 to 7.01. Inset shows the hold voltages for each LED. B) pH sensor steady state measurements in a series of pH solutions. C) Calibration curve. The red shaded region indicates normal physiological range of pH in blood, 7.35 - 7.45, while the orange and grey shaded regions indicate acidosis and alkalosis, respectively.

3.4.4 pH Sensing In Vitro

To determine baseline pH sensor stability, measurements were obtained every 30 min for 8 h in pH 7.45 solution. Unless otherwise stated, each reported steady state measurement is an average of 20 repeats. No signal drift was detected (**Figure S3.4**; CV = 0.002). The stability is due in part to the quality of our custom LED current control circuitry (provided by the TLC driver, **Figure S3.2A**) that produces consistent LED output power. To check the stability of both LEDs, their emission spectra were acquired every 3 min for 30 min. Spectra show no significant differences in

area under curve (CV = 0.001) or peak emission intensity (CV ≤ 0.002; **Figure S3.5**). pH sensing rise time was assessed by first incubating a sensor in a solution with pH 7.45 and then exchanging for a solution with pH 7.01. $R_{Ex400/Ex465}$ was measured every 4.8 s following media exchange. Dynamics are described by a rising exponential plateau model ($R^2 = 0.99$, standard error of the estimate (Sy.x) = 0.006) with rise time of 2.63 min (**Figure 3.6A**). This rise time is short enough to capture critical physiological events such as subdermal scalp acidosis following fetal tachycardia in high-risk births, which occurs on the time scale of minutes.[41]

pH sensing reversibility was assessed by sequential measurements of solutions having pH of 7.05, 7.22, and 7.40 (**Figure 3.6B**). One-way ANOVA indicates a significant effect across groups ($p \ll 0.01$). Tukey post-hoc comparison with adjusted p-values shows significant differences between the three unique pH solutions ($p \ll 0.01$ for each comparison) but no significant differences between repeated pH solutions ($p > 0.25$ for each comparison). pH sensing sensitivity and range was assessed by exposure to thirteen solutions, with pH ranging from 6.92 to 7.59. Data follows a Boltzmann sigmoidal model ($R^2 > 0.99$, Sy.x = 0.002) with a pKa of 7.16 (**Figure 3.6C**), which is similar to the pKa of the HPTS dye alone.[25] Importantly, wellness-of-fit indicates PALS will have clinical relevance across the pathophysiological range including acidosis and alkalosis. [42]

3.4.5 Lactate Sensing In Vitro

To determine baseline lactate sensor stability, measurements were obtained every 30 min for 4 h in 4 mM lactate solution. Unless otherwise stated, each reported steady state value is the mean of 10 measurements. No significant signal drift was detected (**Figure S3.6**; CV = 0.007). The stability is due in part to the inclusion of the enzyme catalase that scavenges hydrogen peroxide, known to degrade proteins. [43,44] Lactate sensing rise time was assessed by changing the test media from 0 mM (1X Phosphate Buffered Saline Solution, PBS) to 6 mM lactate. Phase shift difference

measurements were recorded every 12 s following media exchange. Signals follow an exponential plateau model (R^2 = 0.99, Sy.x = 0.06) with a rise time of 4.8 min (**Figure 3.7A**). This rise time is comparable to commercial continuous glucose monitors such as the Dexcom G6 and Medtronic Guardian, which are reported to have an average rise time *in vivo* of 9.5 min and are effective in guiding insulin therapy. [45]

Lactate sensing reversibility was evaluated by cycling lactate solutions having concentrations of 0, 2.60, 4.64, and 6.53 mM (**Figure 3.7B**). One-way ANOVA detected differences between groups ($p \ll 0.01$). Tukey post-hoc comparison with adjusted p-values shows no significant differences between the pairing of identical lactate solutions ($p > 0.87$), while significant differences were found between solution of different lactate concentrations ($p \ll 0.01$). Lactate sensitivity and range were evaluated by incubation in seven lactate solutions ranging in concentration from 0 to 14 mM. Data follows an exponential plateau model (R^2 = 0.99, Sy.x = 0.03), showing sensitivity to lactate from 0 to 9 mM (**Figure 3.7C**). These results show PALS lactate sensing can distinguish between concentrations within the pathophysiological range.
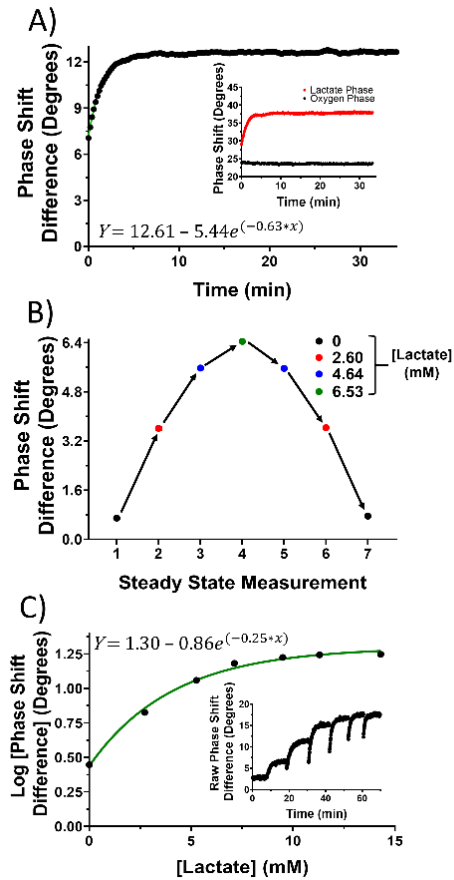
Figure 3.7. In Vitro Lactate Sensing. A) Rise time measured after media exchange from 0 mM to 6 mM lactate. Inset represents the raw lactate and oxygen phase shift measurements. B) Phase shift differences for a series of test solutions. C) Lactate sensor calibration curve. Inset shows raw phase shift differences acquired during the calibration experiment (of increasing concentration).

3.4.6 Multi-analyte Sensing In Vitro

Combined pH and lactate sensing was tested in *in vitro* models of five pathophysiological conditions (**Figure 3.8**). In a model of hyperlactatemia, pH was maintained at 7.43 ± 0.02 while lactate was increased (**Figure 3.8A**). PALS signals report the increase in lactate while the pH signals did not significantly change ($CV = 0.018$). In a model of lactic acidosis, as experienced in sepsis, solutions were formulated to have a decrease in pH and an increase in lactate (**Figure 3.8B**), and PALS successfully report these changes. In a model of extreme metabolic alkalosis, as can

occur with chronic vomiting and diarrhea, pH was increased while lactate was held at 3.50 mM ± 0.02 (**Figure 3.8C**).[46] PALS signals report the increase in pH and constant lactate concentration (CV = 0.027). In a model of panic-disorder patients that exhibit both respiratory alkalosis and hyperlactatemia, solutions were formulated to have an increase in both pH and lactate concentrations.[3] PALS signals successfully reflect these increases (**Figure 3.8D**). In a model of respiratory acidosis (as seen in chronic obstructive pulmonary disease) pH was formulated to decrease while lactate levels were held constant at 3.52 ± 0.02 (**Figure 3.8E**).[47] PALS signals report the decrease in pH and constant lactate concentrations (CV = 0.019). Collectively, **Figure 3.8** demonstrates PALS does not exhibit sensing modality crosstalk and can report physiologically relevant pH and lactate changes, which may aid clinicians in their practice of analyte-guided treatment towards improving patient outcome.
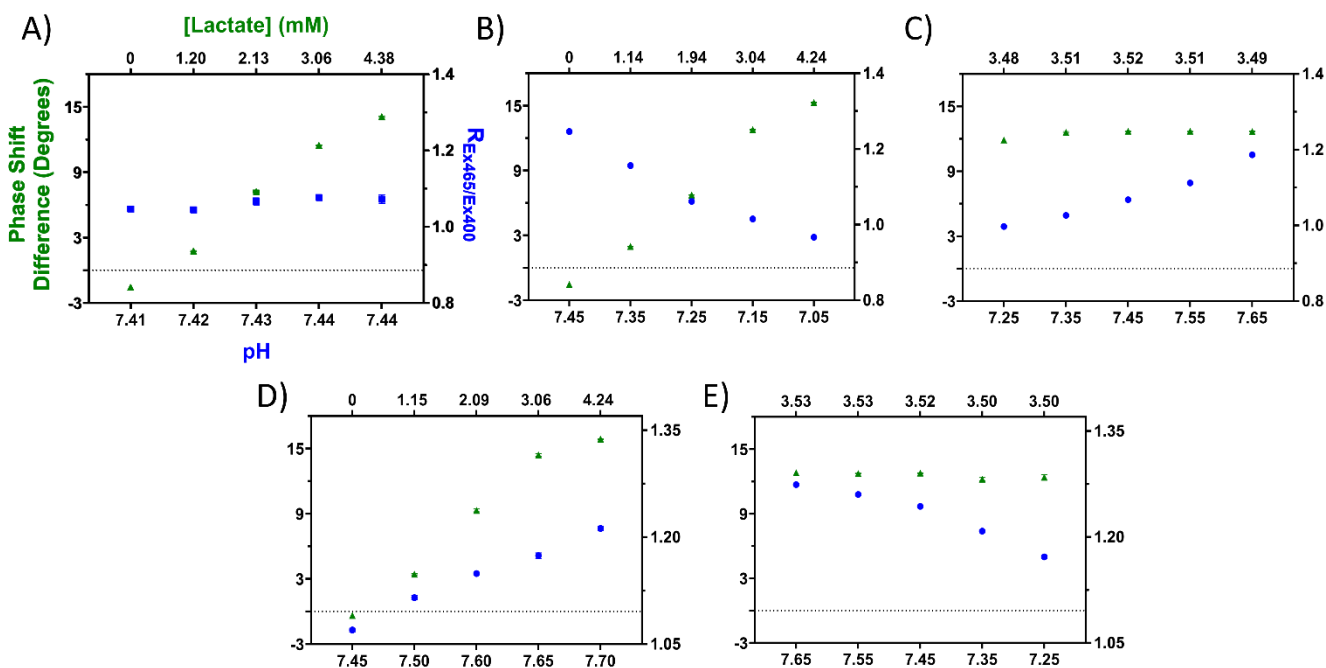
Figure 3.8. pH and Lactate Multi-Analyte Sensing. A series of solutions were formulated to model pathological conditions. Solutions were tested in order from left to right. Solutions model A) hyperlactatemia, B) lactic acidosis, C) extreme metabolic alkalosis, D) respiratory alkalosis and hyperlactatemia, and E) respiratory acidosis.
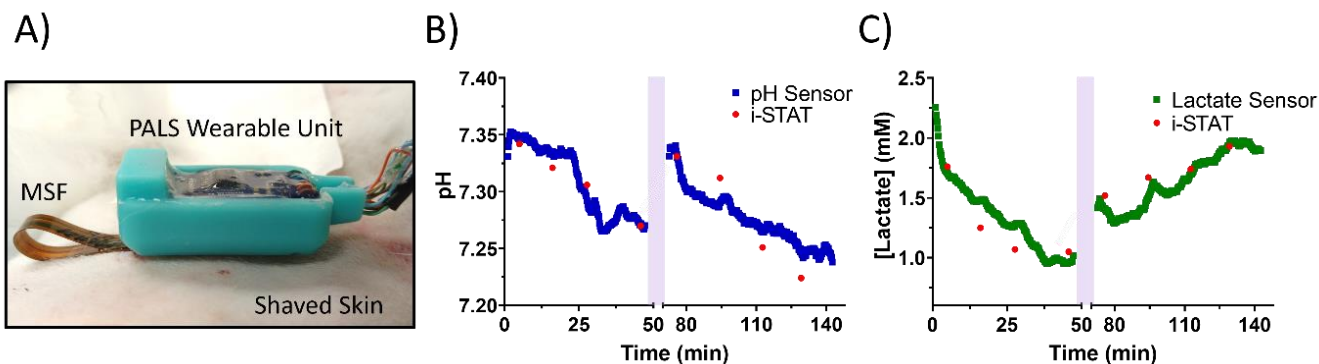
Figure 3.9. *In vivo* multi-analyte sensing in a rabbit exposed to chlorine gas. Purple region indicates when PALS measurements were paused for chlorine gas and cobinamide administration. A) Sensor implanted in the subcutaneous space of the inner left thigh. Lactate (B) and pH (C) sensing signals with intermittent blood reference values (i-STAT).

3.4.7 Multi-analyte Sensing In Vivo

PALS multi-analyte sensing was tested in an *in vivo* rabbit model of chlorine gas poisoning and cobinamide treatment. When chlorine gas reacts with water in the lungs, hydrochloric and hypochlorous acid are produced. The production of these acids damage the respiratory mucus membrane resulting in pulmonary edema and hypoxemia.[48] PALS should therefore detect decreasing pH and increasing lactate values following chlorine gas administration. The MSF-tip was implanted as described in methods **(Figure 3.9A). Figure 3.9B-C** shows that prior to drug infusion but early into intubation, PALS detected a decrease in both pH and lactate concentration, which agrees with the intermittent i-STAT blood assays. After poisoning and cobinamide treatment, PALS detected the expected increase in lactate concentration and decrease in blood pH, which were also in agreement with the intermittent i-STAT blood assays **(Figure 3.9B-C)**. Area-under-the-concentration time curve ratio between PALS and i-STAT measurements was calculated and assessed as described in in Dror et. Al, following FDA guidelines.[38,49] Area-under-the-concentration time curve ratio for pH (0.979) and lactate (1.036) indicate PALS bioequivalence to

the i-STAT blood analyzer in this study. Results demonstrate PALS reports clinically relevant pH and lactate changes, and at a higher frequency than can be offered by blood analysis alone.

3.5 Conclusion

We have shown that two different photonic detection schemes on an implanted flexible sensor can yield reliable signals for monitoring both pH and lactate across clinically relevant ranges. However, the technology should be improved before it can be used in the clinic. Because the process of PALS fabrication is not controlled at the level expected for a commercial product, we do observe differences in calibration parameters between units. Currently methods are being developed by our group to reduce variances in sheet fabrication and to improve the process by which the plastic optical filter is applied onto the photodetector. Additional engineering development will include miniaturization of the backend electronics as well as wireless data control and acquisition, which are achievable by existing manufacturing methods.

PALS can have a major impact on patient outcomes in conditions such as sepsis and organ failure where attentive monitoring of pH and lactate has been reported to improve patient outcome.[1-4] Importantly, the core elements of PALS can be replicated and modified to sense additional analytes on the MSF. For example, similar to the operating principle of HPTS, fluorescent dyes Fura Red AM and SBFI-AM exhibit a change in their absorbance behavior based upon the concentration of calcium and sodium, respectively.[50,51] Consequently our dual-excitation, single band detection scheme could be readily employed to continuously monitor these analytes. Moreover, our lactate sensing scheme is generalizable to additional oxidases and its corresponding analyte including those for glucose and alcohol. [52,53]The addition of these analytes can broaden the applicability of the MSF to other medical conditions. For example, continuous monitoring of sodium, pH, lactate, oxygen, and glucose, in individuals experiencing diabetic ketoacidosis, can diagnose dehydration

(loss of sodium), ketoacidosis (high glucose and low pH) and ischemia (low oxygen and high lactate), directing healthcare professionals towards a specific mode of intervention.[54–56] An expanded MSF could also be applicable beyond the medical field, such as in bioreactors for protein expression, agriculture, water management, and food industry, where sensing pH, glucose, and sodium, would provide vital information to each respective field.[57–60]

3.6 Acknowledgements

3.7 Supporting Information

3.7.1 Oxygen-Sensitive Dye-Coated PTFE Sheet Fabrication

Oxygen-sensitive dye solution was created by mixing 4 mg of PtTPTBP dye (Frontier, USA), 60 mg of polystyrene (molecular weight: 2500, Sigma-Aldrich, USA) and 900 µL of chloroform (Sigma-Aldrich, USA) in a 1.5 mL amber vial. The resulting concentrations are 440.873 µM PtTPTBP and 0.024 mM polystyrene in 900 µL chloroform. 200 µL of this solution was pipetted onto a circular PTFE sheet. The chloroform was allowed to evaporate resulting in the oxygen-

sensitive dye-coated PTFE sheet. This dye-coated PTFE sheet served as the base of both the LOX and Oxygen Sheets.

3.7.2 LOX Sheet Solution Preparation

The LOX sheet is formulated using two solutions: (1) Protein Mixture and (2) Pretreatment Solution. Protein Mixture is composed of 0.060 mM LOX (LCO-301, 108U/mg, 0.0096 mg/µL, Toyobo, Japan), 193.13 mM poly(ethylene glycol) dimethacrylate 2000 (PEGDMA2000, 0.386 mg/µL, Sigma-Aldrich, USA), 43.33 mM Lithium phenyl-2,4,6-trimethylbenzoylphosphinate (LAP, 0.0127 mg/µL, Sigma-Aldrich, USA), 1.16 mM catalase (AN366A, 5410U/mg, 0.28 mg/µL, BBI Solutions, U.K.), and 1X Phosphate Buffered Saline Solution (1X PBS). Pretreatment Solution is composed of 75% v/v poly(ethylene glycol) diacrylate 400 (PEGDA400, Polysciences, USA), 25 % v/v Milli-Q water, and 28 mM LAP (0.00825 mg/µL).

3.7.3 LED Spectra Acquisition System

To acquire LED spectra, a caged system containing a suspended optical fiber was created. All items were procured from ThorLabs (USA). A Blank Cage Plate (LCP03) was used as the base of the system. Assembly rods SR05, SR1, and SR1.5 rods were used to build vertically. Vertical mount plate CPVM threaded with a SM1SMA fiber adapter was used to incorporate jacketed fiber patch cable M92L01 into the system. The distance between the M92L01 aperture and the blank cage plate was approximately 90 mm. The opposite end of the jacketed optical fiber was connected to a CCS200 spectrometer. MSF with LEDs were taped down and placed in the center of the blank cage plate such that upon LED activation, M92L01 would capture emitted light. ThorLabs Optical Spectrum Analyzer (OSA) software was used to acquire spectra. Unless otherwise stated, integration times were set to 100 ms. To acquire data, LabView code (National Instruments, USA)

was used to turn on the MSF LEDs and spectra were then obtained using the LED Spectra Acquisition System. Drive currents for each LED were less than 10 mA.

3.7.4 Assembly of PALS Wearable Unit

For the integrator board, four 0.1 uf capacitors (80-C0805C104K5RACLR, KEMET, USA) and a IVC102 transimpedance amplifier were soldered by reflow soldering. Reflow soldered onto the photodetector board are the following components: a 1 pF capacitor (C0603C109B4HACTU, KEMET, USA), a 1 Mohm resistor (ERJ-3EKF1004V, Panasonic, Japan), 1 uF capacitors (80-C0603C105Z3VACTU, KEMET, USA), 0.1 uF capacitors, 4.99 kohm resistors (RN73H2BTTD4991F100, KOA Speer, USA), a 4.7 uF capacitor (12065C475K4T4A, AVX Corporation, USA), a LTC6244HV operational amplifier (LTC6244HVCMS8#TRPBF, Analog Devices, USA), and a J-FET (BF862, NXP USA). A Silicon photodetector was soldered onto the photodetector board using a solder iron.

The connector board was developed to connect the integrator and photodetector boards to the MSF. The connector board has a 5 spring battery connector soldered on via reflow soldering to connect to the MSF. The integrator, photodetector, and connector boards all contain 5 through holes to connect to one another. To connect the three circuits, 1.27 mm pitch header pins were first soldered through the photodetector circuit (photodetector facing down) with a solder iron. The connector circuit was then soldered to the same header pins, on top of the lactate detector circuit, followed by the integrator board (with the IVC facing out) being soldered on top of the connector circuit.

3.7.5 Assembly of PALS Backend Controller Unit

To fabricate the IVC power supply board, a 0.1 uf capacitor , 2.2 uf capacitors (08055C225KAT2A, AVX Corporation, USA), 470 uH inductors (82474C, Murata, Japan), a 2.7 kohm resistor (667-ERJ-UP3F2701V, Panasonic, Japan), and a 10 kohm resistor (667-ERJ-

UP3F1002V, Panasonic, Japan) were soldered onto the board via reflow soldering. Through hole components including a 3.3 V to 15 V power converter, stacking header pins and ethernet jack were soldered on with a solder iron.

The controller board had the following surface mount soldered on via reflow soldering: 22uH inductors (82223C, Murata, Japan), 2.2 uf capacitors, 0.1 uf capacitors, a 22 ohm resistor (CHP0603AJW-220ELF, Bourns, USA), a 680 ohm resistor (ERJ-UP3J681V, Panasonic, Japan), a 100 ohm trimmer potentiometer (TC33X-2-101E, Bourns, USA), a 1 kohm resistor (CR0603AFX-1001ELF, Bourns, USA) , a TLC driver board , and a 1-of-8 Multiplexer FET Switch. Through hole components 3.3 V to 5 V power converter, ethernet jack, and 0.1" female header pins were soldered onto the board with a solder iron.

3.7.6 Connecting the Wearable Housing Unit to the Backend Controller Unit

To connect the IVC power supply board to the integrator board, an ethernet patch cable (Monoprice SlimRun, USA) was first cut in half. The half with the ethernet cable intact was connected to the ethernet jack on the IVC power supply board. The other half with the eight 30 american gauge exposed were routed through through-holes located on the bottom of the integrator board and soldered to their appropriate connections (with a soldering iron). This process was repeated to connect the controller board to the photodetector board.

3.7.7 Sensor Film Application

The HSS was the first sensor sheet applied. After swelling, the HSS was removed from Milli-Q water and placed onto a glass slide. A razor blade was used to remove hydrogel from the sheet edges to expose underlying PTFE. This process resulted in a rectangular hydrogel with dimensions of roughly 1 cm x 0.8 cm. Loctite 4981 was then applied along the width of the MSF, between the 465 nm LED and the top-most 625 nm LED. The shorter side of the HSS (0.8 cm) with exposed

PTFE was laid down onto the Loctite 4981, with the resin-tethered HPTS side facing the LEDs. The Loctite 4981 (Henkel, Germany) was then allowed to cure. The MSF was then flipped over, and Loctite 4981 was applied to the top edge and along the lateral edges of the back of the MSF. The remaining exposed PTFE edges of the HSS were then pressed in contact with the Loctite 4981 and allowed to cure.

After HSS was cured onto the MSF, LOX and Oxygen Sheets were applied onto the MSF. The sheets were cut into smaller sheets (1.8 mm x 1.5 mm) immediately following polymerization and adhered directly onto the 625 nm LEDs with Loctite 4981. When all sensing sheets were applied, the MSF was allowed to incubate in 1X PBS for at least 8 h at room temperature prior to testing.

3.7.8 Benchtop Optical System Set-up

The benchtop optical system was built using ThorLabs (USA) assembly rods (SR05, SR1, and SR1.5 rods) with vertical cage system mounting plate CPVM (ThorLabs, USA) serving as the base component. Building from bottom to top, cage plate LCP01T (ThorLabs, USA) was suspended above the CPVM to add on a jacketed multi-mode optical fiber patch cable (0.22 NA, 200 µm core, M92L02, ThorLabs, USA) coupled to a collimator (F810APC-543, ThorLabs, USA). The opposite end of the optical fiber patch cable was connected to a CCS200 spectrometer (ThorLabs, USA). Above the collimator, a LCP02 (ThorLabs, USA) cage plate adapter housing a 5x objective lens (0.10 NA, Newport, USA) was added to capture HSS-emitted light. Settled above the objective lens on an additional LCP02 was a Perma-Proto board (Adafruit, USA) with 400 and 465 nm dominant-wavelength LEDs soldered on opposite ends of a drilled hole (diameter = ¼ inch). In parallel, exposed PTFE of an HSS was used to adhere the sheet onto a µ-Slide 2 well (Ibidi, USA) using Loctite 4981. The adhesive was allowed to dry for at least 5 min prior to testing. The well was secured above the protoboard using tape. The well was positioned, such that upon

testing, the HSS sat over the LEDs and emitted light was collected through the drilled hole with the 5x objective lens.

ThorLabs OSA software was used to acquire spectra data. An Arduino Uno (Arduino, USA) with custom Arduino software (Arduino, USA) was used to power the LEDs (5V output). Resistors (±5% tolerance range, BOJACK, China) with total resistance values of 1450 and 830 ohms were placed in series with the 400 and 465 nm LEDS, respectively. Integration time for both LEDs was 1s. For pH testing, the HSS was first washed with the first pH test solution 10 times and then allowed to equilibrate for 30 s. 3 emission spectra were recorded for each LED and averaged after background spectrum (no LED excitation) subtraction. The background-subtracted emission spectrum was then saved as a text file. To exchange pH solution, the solution previously tested was aspirated under vacuum and the next pH test solution was tested as previously mentioned. MATLAB (MathWorks, USA) was used for subsequent analysis.

3.7.9 pH Solution Preparation, Validation, and Testing

pH test solutions were prepared following Sigma-Aldrich's Phosphate Buffer Preparation Table, using potassium phosphate monobasic anhydrous (795488-500G, Sigma-Aldrich, USA), sodium phosphate dibasic heptahydrate (S9390-1KG, Sigma- Aldrich, USA), and Milli-Q water. Polynomial equations were fitted onto both reagent quantities listed in the Preparation Table to interpolate pH solution formulations. The pH solutions were probed using a Mettler Toledo FiveEasy pH probe (Sigma Aldrich, USA). pH probe calibrations were completed with pH 4.01, 7.00, and 10.01 buffer solutions (Orion™ Standard All-in-One™ pH Buffer Kit, 910199, ThermoFisher Scientific). Only calibrations with slopes greater than 95 were used. For pH testing *in vitro*, measurements were obtained at room temperature. For PALS pH testing *in vitro*, each MSF was placed in a 20 mL scintillation vial and incubated in the series of pH solutions. For

testing, except for rise times studies, the MSF was first washed with the pH test solution 10 times and then allowed to equilibrate for 30 s. After measurements were obtained, the test solution was aspirated. This process was completed for each new test solution. For rise time studies, only 1 wash was completed when introducing the next test solution.

3.7.10 Lactate Solution Preparation, Validation, and Testing

Lactate test solutions were prepared with L-(+)-Lactic acid solution (27714-1L, Sigma Aldrich, USA) and 1X PBS. pH adjustments were made with 0.1 M HCl and 0.1 M NaOH (43617, Sigma-Aldrich). 0.1 M HCl was formulated by diluting 11 N HCl (A144C-212, Fisher Scientific, USA) with Milli-Q water. Unless otherwise noted, pH of lactate solutions was adjusted to 7.45. The lactate solutions were verified using a YSI 2300 STAT Plus Glucose and Lactate Analyzer (Yellow Springs Instrument, USA). For lactate testing *in vitro*, measurements were obtained at room temperature. Each MSF was placed in a 60 mm plastic dish (BD Falcon, USA) and incubated in the series of lactate solutions. For testing, except for rise times studies, the MSF was first washed with the lactate test solution 10 times and then allowed to equilibrate for 30 s. After measurements were obtained, the test solution was aspirated. This process was completed for each new test solution. For rise time studies, only 1 wash was completed when introducing the next test solution.
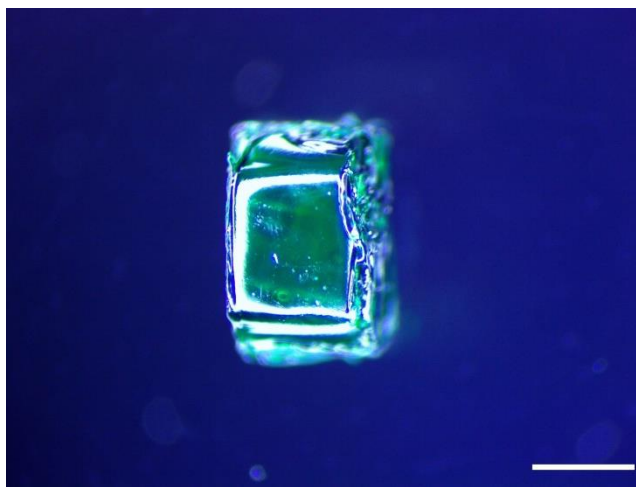
Figure S3.1. Micrograph of a Filter-Coated Photodetector. Scale bar = 1 mm. Primary Green filter applied onto a SFH2716 photodiode (OSRAM Opto Semiconductors, Germany).
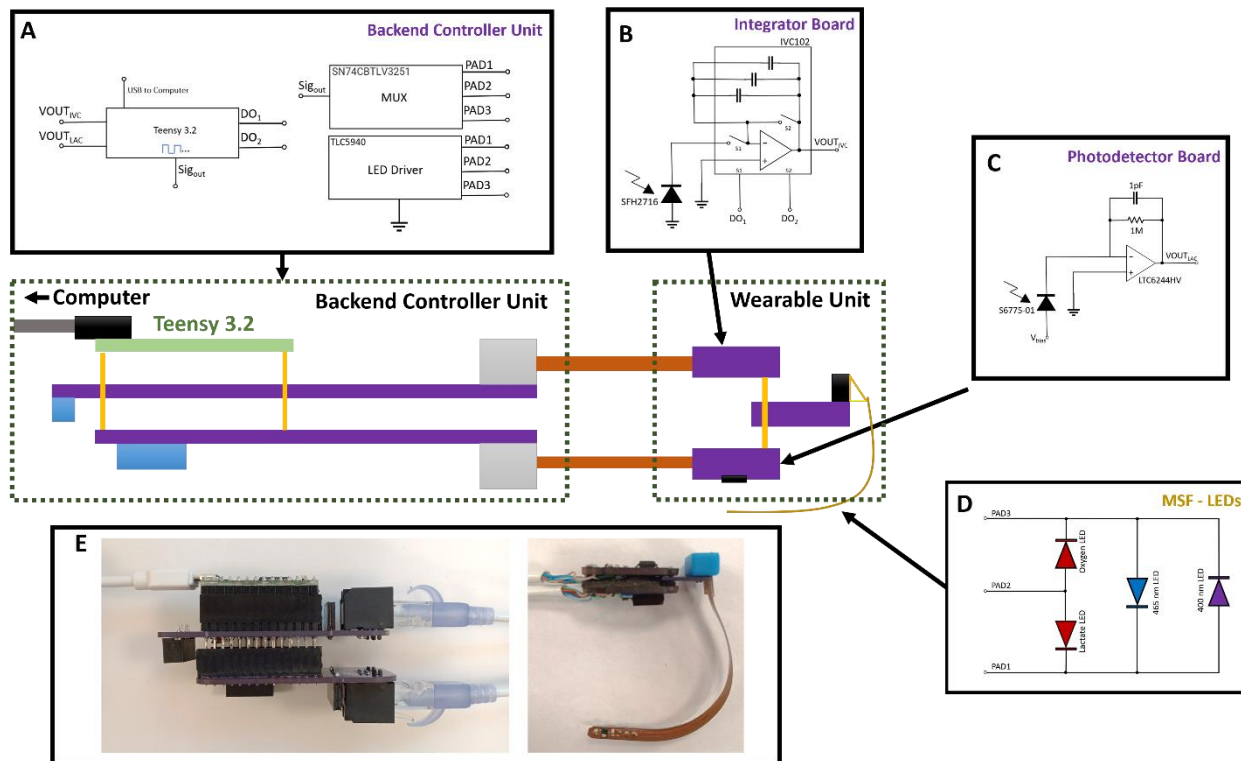
Figure S3.2. Simplified Schematics of PALS Printed Circuit Boards. A) High side control of the charlieplex circuit is achieved with a multiplexer (SN74CBTLV3251PWR, Texas Instruments, USA), which toggles the output line of a square wave generated by the Teensy 3.2. Low side control is achieved by a constant sink LED driver (TLC5940, Texas Instruments, USA). The sink was alternated over 3 lines to control 4 LEDs on the MSF. B) Integrator board utilizing 100pF internal capacitance. Timing of IVC102 integration is controlled by the Teensy 3.2 via digital outputs. IVC102 output signal is run through a voltage divider (not shown) before being read at the analog input of the Teensy 3.2. C) Photodetector board utilizing a S6775-01 photodiode (Hamamatsu, Japan). Output signals from the op amp are read using an analog input of the Teensy 3.2. D) LED charlieplexing schematic. E) Fully connected PALS.
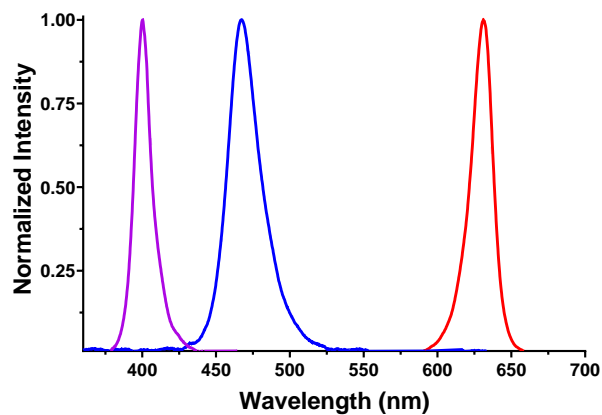
Figure S3.3. Normalized LED Emission Spectra. Signals were obtained using the LED Spectra Acquisition System. Spectra were corrected for any background signals. The 400, 465, and 625 nm LEDs have peak emission wavelengths of 400, 467, and 631 nm, respectively.
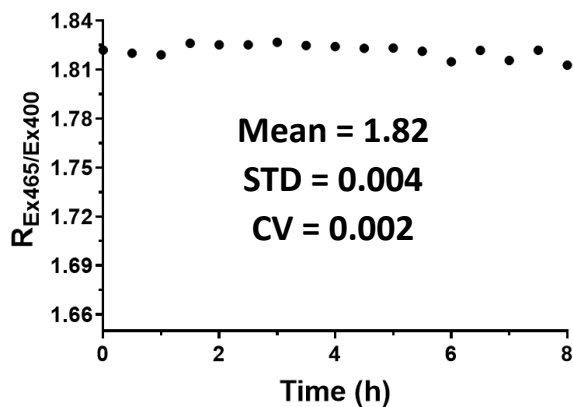
Figure S3.4. Baseline pH Sensor Stability in pH 7.45. PALS pH sensor measurements over 8 h.
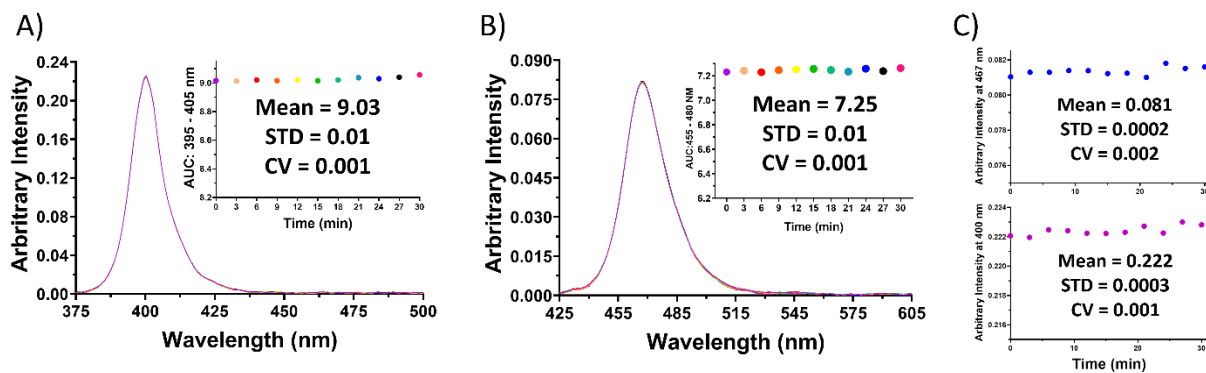
Figure S3.5. Spectral Stability of the pH Optode LEDs. Spectra were obtained every 3 min for 30 min with the LED Spectra Acquisition System. Each spectrum is an average of 3 measurements

after background signal subtraction. A) Overlapped 400 nm LED spectra. Inset: AUC analysis of wavelengths encompassing the peak emission wavelength show minimal variance. B) Overlapped 465 nm LED spectra. Inset: AUC analysis shows minimal variance. C, Top) 465 nm LED peak emission intensity at 467 nm shows no significant change over time. C, Bottom) 400 nm LED peak intensity is stable.

Figure S3.6. Baseline Lactate Sensor Stability. Lactate sensing in 4 mM lactate over 4 h.

3.8 References:

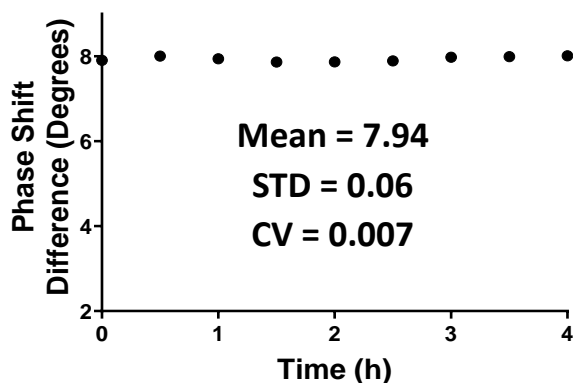1   Lee, S. W. *et al.* Lactic acidosis not hyperlactatemia as a predictor of inhospital mortality in septic emergency patients. *Emergency Medicine Journal* **25**, 659–665 (2008).

2.   Scheiner, B. *et al.* Acid-base disorders in liver disease. *Journal of Hepatology* vol. 67 1062–1073 (2017).

3.   Hall, A. M. & Bending, M. R. Severe hyperlactaemia in the setting of alkalaemia. *NDT Plus* **2**, 408–411 (2009).

4.   Kellum, J. A. Determinants of blood pH in health and disease. *Critical Care* vol. 4 6–14 (2000).

5.   Kellum, J. A. Determinants of blood pH in health and disease. *Critical Care* vol. 4 6–14 (2000).

6.   M N, A., Mudda, V., Chandra, M. & T J, S. PHYSIOLOGY OF ACID BASE BALANCE. *Journal of Evidence Based Medicine and Healthcare* **1**, 2140–2152 (2014).

7.   Zilva, J. F. The origin of the acidosis in hyperlactataemia. *Annals of Clinical Biochemistry* vol. 15 40–43 (1978).

8.   Foucher, C. D. & Tubben, R. E. Lactic Acidosis. *StatPearls* (2020).

9.   Meakins, J. & Long, C. N. H. OXYGEN CONSUMPTION, OXYGEN DEBT AND LACTIC ACID IN CIRCULATORY FAILURE 1. *Journal of Clinical Investigation* **4**, 273–293 (1927).

10.   Patel, S. & Sharma, S. *Physiology, Acidosis, Respiratory*. *StatPearls* (StatPearls Publishing, 2018).

11.   Dukić, L., Kopčinović, L. M., Dorotić, A. & Baršić, I. Blood gas testing and related measurements: National recommendations on behalf of the Croatian society of medical biochemistry and laboratory medicine. *Biochemia Medica* vol. 26 318–336 (2016).

12.   White*, R., Yaeger*, D. & Stavrianeas‡, S. Determination of Blood Lactate Concentration: Reliability and Validity of a Lactate Oxidase-based Method. *International Journal of Exercise Science* **2**, (2009).

13.   Steinfelder-Visscher, J., Teerenstra, S., Klein Gunnewiek, J. M. T. & Weerwind, P. W. Evaluation of the i-STAT point-of-care analyzer in critically ill adult patients. *Journal of Extra-Corporeal Technology* **40**, 57–60 (2008).

14.   Bodley, T. *et al.* Patient Harm from Repetitive Blood Draws and Blood Waste in the ICU: A Retrospective Cohort Study. *Blood* **134**, 57–57 (2019).

15.   Pölönen, P., Ruokonen, E., Hippeläinen, M., Pöyhönen, M. & Takala, J. A prospective, randomized study of goal-oriented hemodynamic therapy in cardiac surgical patients. *Anesthesia and Analgesia* **90**, 1052–1059 (2000).

16.   Friedman, G., Berlot, G., Kahn, R. J. & Vincent, J. L. Combined measurements of blood lactate concentrations and gastric intramucosal pH in patients with severe sepsis. *Critical Care Medicine* **23**, 1184–1193 (1995).

17.   Jansen, T. C. *et al.* The prognostic value of blood lactate levels relative to that of vital signs in the pre-hospital setting: A pilot study. *Critical Care* **12**, (2008).

18.   Ganesh, K., Sharma, R., Varghese, J. & Pillai, M. G. K. A profile of metabolic acidosis in patients with sepsis in an Intensive Care Unit setting. *International Journal of Critical Illness and Injury Science* **6**, 178–181 (2016).

19.   Manjakkal, L., Szwagierczak, D. & Dahiya, R. Metal oxides based electrochemical pH sensors: Current progress and future perspectives. *Progress in Materials Science* vol. 109 100635 (2020).

20.   Vonau, W. & Guth, U. pH Monitoring: A review. *Journal of Solid State Electrochemistry* vol. 10 746–752 (2006).

21.   Khan, M. I., Mukherjee, K., Shoukat, R. & Dong, H. A review on pH sensitive materials for sensors and detection methods. *Microsystem Technologies* vol. 23 4391–4404 (2017).

22.   Miksa, M., Komura, H., Wu, R., Shah, K. G. & Wang, P. A novel method to determine the engulfment of apoptotic cells by macrophages using pHrodo succinimidyl ester. *Journal of Immunological Methods* **342**, 71–77 (2009).

23.   Boens, N. *et al.* Photophysics of the fluorescent pH indicator BCECF. *Journal of Physical Chemistry A* **110**, 9334–9343 (2006).

24.   Ramshesh, V. K. & Lemasters, J. J. Imaging of mitochondrial pH using SNARF-1. *Methods in Molecular Biology* **810**, 243–248 (2012).

25.   Kermis, H. R., Kostov, Y., Harms, P. & Rao, G. Dual excitation ratiometric fluorescent pH sensor for noninvasive bioprocess monitoring: Development and application. *Biotechnology Progress* **18**, 1047–1053 (2002).

26.   An, Y., Bai, H., Li, C. & Shi, G. Disassembly-driven colorimetric and fluorescent sensor for anionic surfactants in water based on a conjugated polyelectrolyte/dye complex. *Soft Matter* **7**, 6873–6877 (2011).

27.   Hulth, S., Aller, R. C., Engström, P. & Selander, E. A pH plate fluorosensor (optode) for early diagenetic studies of marine sediments. *Limnology and Oceanography* **47**, 212–220 (2002).

28.   Yanase, S., Yasuda, K. & Ishii, N. Small-Scale Colorimetric Assays of Intracellular Lactate and Pyruvate in the Nematode Caenorhabditis elegans. *Journal of visualized experiments : JoVE* (2018) doi:10.3791/57807.

29. Erdoğan, H., Aypak, S. Ü., Erdoğan, S. & Ural, K. Comparative interpretation of lactate measurement by point of care spectrophotometric and ELISA methods in transition cows. *Polish Journal of Veterinary Sciences* **21**, 741–746 (2018).

30. Rathee, K., Dhull, V., Dhull, R. & Singh, S. Biosensors based on electrochemical lactate detection: A comprehensive review. *Biochemistry and Biophysics Reports* vol. 5 35–54 (2016).

31. Park, J. *et al.* Microscale Biosensor Array Based on Flexible Polymeric Platform toward Lab-on-a-Needle: Real-Time Multiparameter Biomedical Assays on Curved Needle Surfaces. *ACS Sensors* **5**, 1363–1373 (2020).

32. Payne, M. E., Zamarayeva, A., Pister, V. I., Yamamoto, N. A. D. & Arias, A. C. Printed, Flexible Lactate Sensors: Design Considerations Before Performing On-Body Measurements. *Scientific Reports* **9**, 1–10 (2019).

33. Currano, L. J. *et al.* Wearable Sensor System for Detection of Lactate in Sweat. *Scientific Reports* **8**, 15890 (2018).

34. Park, J. *et al.* Microscale Biosensor Array Based on Flexible Polymeric Platform toward Lab-on-a-Needle: Real-Time Multiparameter Biomedical Assays on Curved Needle Surfaces. *ACS Sensors* **5**, 1363–1373 (2020).

35. Maahs, D. M. *et al.* Effect of Acetaminophen on CGM Glucose in an Outpatient Setting. *Diabetes Care* **38**, e158 (2015).

36. Juska, V. B. & Pemble, M. E. A Critical Review of Electrochemical Glucose Sensing: Evolution of Biosensor Platforms Based on Advanced Nanosystems. *Sensors (Basel, Switzerland)* **20**, 1–28 (2020).

37. Andrus, L. P., Unruh, R., Wisniewski, N. A. & McShane, M. J. Characterization of Lactate Sensors Based on Lactate Oxidase and Palladium Benzoporphyrin Immobilized in Hydrogels. *Biosensors* **5**, 398 (2015).

38. Dror, N. *et al.* Clinical evaluation of a novel subcutaneous lactate monitor. *Journal of Clinical Monitoring and Computing 2021* 1–7 (2021) doi:10.1007/S10877-021-00685-1.

39. Valledor, M. *et al.* Determination of phosphorescence lifetimes in the presence of high background signals using phase-shift measurements. *Sensors and Actuators B: Chemical* **113**, 249–258 (2006).

40. Smith, A. M., Mancini, M. C. & Nie, S. Bioimaging: Second window for in vivo imaging. *Nature Nanotechnology* vol. 4 710–711 (2009).

41. Young, B. K., Hirschl, I. T., Klein, S. H. & Katz, M. *25. Continuous Fetal Tissue pH Monitoring in Labor with High Risk Pregnancies*. vol. 226 (1978).

42. Hopkins, E., Sanvictores, T. & Sharma, S. Physiology, Acid Base Balance. *Urolithiasis* 19–22 (2020).

43. Fligiel, S. E. G., Lee, E. C. & McCoy, J. P. Protein degradation following treatment with hydrogen peroxide. *American Journal of Pathology* **115**, 418–425 (1984).

44. Davies, M. J. Protein oxidation and peroxidation. *Biochemical Journal* vol. 473 805–825 (2016).

45. Schmelzeisen-Redeker, G. *et al.* Time delay of CGM sensors: Relevance, causes, and countermeasures. *Journal of Diabetes Science and Technology* **9**, 1006–1015 (2015).

46. Ueda, Y., Aizawa, M., Takahashi, A., Fujii, M. & Isaka, Y. Exaggerated compensatory response to acute respiratory alkalosis in panic disorder is induced by increased lactic acid production. *Nephrology Dialysis Transplantation* **24**, 825–828 (2009).

47. Pahal, P. & Sharma, S. *Chronic Obstructive Pulmonary Disease (COPD) Compensatory Measure*. *StatPearls* (StatPearls Publishing, 2019).

48. Gorguner, M. & Akgun, M. Acute Inhalation Injury. *The Eurasian Journal of Medicine* **42**, 28 (2010).

49. Office of Training and Communications Division of Communications Management Drug Information Branch. 301–827 (2001).

50. Kurebayashi, N., Harkins, A. B. & Baylor, S. M. *Use of fura red as an intracellular calcium indicator in frog skeletal muscle fibers*.

51. Katoh, D. *et al.* A technique for quantifying intracellular free sodium ion using a microplate reader in combination with sodium-binding benzofuran isophthalate and probenecid in cultured neonatal rat cardiomyocytes. *BMC Research Notes* **6**, 556 (2013).

52. Nery, E. W., Kundys, M., Jeleń, P. S. & Jönsson-Niedziólka, M. Electrochemical glucose sensing: Is there still room for improvement? *Analytical Chemistry* **88**, 11271–11282 (2016).

53. Vonck, J., Parcej, D. N. & Mills, D. J. Structure of alcohol oxidase from pichia pastoris by cryo-electron microscopy. *PLoS ONE* **11**, e0159476 (2016).

54. Seth, P., Kaur, H. & Kaur, M. Clinical profile of diabetic ketoacidosis: A prospective study in a tertiary care hospital. *Journal of Clinical and Diagnostic Research* **9**, OC01–OC04 (2015).

55. Etiology and therapeutic approach to elevated lactate. https://www.ncbi.nlm.nih.gov/pmc/articles/PMC3975915/.

56. Ibarra, G., Majmundar, M. M., Pacheco, E., Zala, H. & Chaudhari, S. Hypernatremia in Diabetic Ketoacidosis: Rare Presentation and a Cautionary Tale. *Cureus* **12**, (2020).

57. Castellanos-Mendoza, A. *et al.* Influence of pH control in the formation of inclusion bodies during production of recombinant sphingomyelinase-D in Escherichia coli. *Microbial Cell Factories* **13**, 1–14 (2014).

58. Marles, R. J. Mineral nutrient composition of vegetables, fruits and grains: The context of reports of apparent historical declines. *Journal of Food Composition and Analysis* vol. 56 93–103 (2017).

59. Zulkifli, S. N., Rahim, H. A. & Lau, W. J. Detection of contaminants in water supply: A review on state-of-the-art monitoring technologies and their applications. *Sensors and Actuators, B: Chemical* vol. 255 2657–2689 (2018).

60. Thakur, M. S. & Ragavan, K. V. Biosensors in food processing. *Journal of Food Science and Technology* vol. 50 625–641 (2013).

CHAPTER 4: CONCLUSION

Phlebotomy and arterial blood gas sampling provide healthcare professionals a static measurement of critical analytes such as pH, SpO_2, glucose, lactate, and creatine. Although single point measurements suffice for routine wellness checks, patients in critical care need more data points to determine if the provided treatment is improving their outcome. Unfortunately, current blood sampling strategies may result in anemia, low hematocrit, blood infection, and nerve damage which may worsen the patient's condition.

As an alternative to frequent blood sampling, my thesis work develops implantable optical sensors to continuously monitor biomarkers. Analytes such as calcium, pH, and lactate are continuously monitored. This work builds upon existing sensing strategies developed in the Botvinick Lab while also developing new ones. In Chapter 2, I use FRET technology to fabricate an implantable Ca^{2+} sensor. Results show sensor stability and the ability to record Ca^{2+} from 0.01 to 10 mM. Although Ca^{2+} is monitored, genetically modified FRET proteins that are selective to additional analytes (such as magnesium, insulin, or glucose) can as easily be integrated into the sensor to measure the corresponding analyte. In Chapter 3, I develop a dual excitation, single band detection scheme on an implantable sensor to measure pH. This work reduces analyte-sensitive spectroscopic data into voltages where due to the absorbance behavior of the selected pH-sensitive dye, the ratio of voltages (after dual LED excitation) can be used to monitor pH. This platform can be easily substituted with fluorescent dyes whose absorbance behavior also change due to the analyte concentration. The integration of the Botvinick Lab's lactate sensor yields a pH and lactate sensor that can have a major impact in ailments associated with lactic acidosis, such cardiac failure and sepsis.